

ULTRAFAST ELECTRON DIFFRACTION WITH HIGH SIX DIMENSIONAL BRIGHTNESS

A Dissertation

Presented to the Faculty of the Graduate School

of Cornell University

in Partial Fulfillment of the Requirements for the Degree of

Doctor of Philosophy

by

Cameron James Richard Duncan

May 2022

© 2022 Cameron James Richard Duncan
ALL RIGHTS RESERVED

ULTRAFAST ELECTRON DIFFRACTION WITH HIGH SIX DIMENSIONAL BRIGHTNESS

Cameron James Richard Duncan, Ph.D.

Cornell University 2022

Time-resolved measurements provide information about dynamical processes and are essential for studying complex physical, chemical and biological systems out of equilibrium. Electron probes in diffraction mode are uniquely suited to investigate correlated structural changes at surfaces, interfaces, and in atomically-thin materials. Ultrafast electron diffraction thus has a special role to play as a tool for scientists and engineers in the investigation of two-dimensional materials for modern technologies. This thesis reports the design, commissioning and first science results of a new ultrafast electron diffraction apparatus. The apparatus incorporates an extremely vacuum sensitive semiconductor electron source with a band gap matched to the wavelength of the photoemission laser. The source produces beams with state-of-the-art brightness at sub-relativistic acceleration energies. A single-electron-sensitive, high-dynamic-range, fast-frame-rate detector allows lock-in style data acquisition. Operated in this way, the experimental uncertainty of the apparatus is measured to be at the fundamental limit imposed by counting statistics. Time-resolved experiments performed on a twisted heterobilayer point to the potential for high-impact science results from the apparatus. This thesis also describes the design of a future upgrade to the apparatus that would enable high-resolution electron energy loss spectroscopy, making the apparatus sensitive to ultrafast changes in the electronic as well as structural properties of experimental samples.

BIOGRAPHICAL SKETCH

Cameron James Richard Duncan was born in Louisville, Kentucky on March 5, 1987. His father, Gerald Allan Duncan, was born in Grand Rapids, Minnesota. His mother, Jill Christine Duncan née Bonlender, was born in Chicago, Illinois. Cameron and his parents moved to Perth, Australia in 1989, where his two siblings, McKenzie and Allana, were born. His family moved again in 1999 to Adelaide, Australia, then to Sydney, Australia in 2005. Gerald served as a minister of the Uniting Church in Australia and received his Doctor of Ministry from the University of Dubuque Theological Seminary. Jill received her doctorate in Applied Linguistics from the University of Western Australia and, after a career in teaching, school administration and government, currently lectures at the University of Newcastle, Australia. Cameron earned his B.A. in Philosophy from the University of Sydney in 2009, with an Honours thesis on Logical Empiricism, a philosophical movement in the twentieth century that stressed experimentation as the foundation of our knowledge of the world. Cameron received his LL.B. in 2011 from the University of Sydney and was admitted as a lawyer of the Supreme Court of New South Wales in 2012. He earned his B.Sc. in 2015, again from the University of Sydney, double majoring in Mathematics and Physics. Cameron began his doctoral studies in physics at Cornell University in Fall, 2016. He worked on the Muon G-2 experiment at Fermilab under Lawrence Gibbons before joining Jared Maxson's ultrafast lab in Spring, 2018.

To my parents.

ACKNOWLEDGEMENTS

Thanks to **my sisters**, Allana and McKenzie, and to **my parents**, Jerry and Jill. Thanks to **my academic advisors**, Jared Maxson and Ivan Bazarov. Thanks to **all Cornell graduate students**, but especially, Robert Noest, Peter Sprau, Collin Clement, Matthew Bierbaum, John Stout, Frederik De Keersmaecker, Lauren McLeod, Michelle Kelley, Naomi Gendler, Mariel Tader, Berit Goodge, Jaron Kent-Dobias, Éamonn O'Shea, Michael "Pittsburgh Mike" Matty, Ryan Porter, Christopher Parzyck, Thomas Oseroff, Eve Vavagiakis, Patrick Hollister, Eric Schwen, Colin Bundschu, Peter Cha, Nathan Sitaraman, Maya Martirosyan, Sam Bright-Thonney, Ben Gregory, William Bergan and Ross "The Treasurer" Jennings. Thanks to **my labmates**, William Li, Jai Kwan Bae, Michael Kaemingk, Chad Pennington, Christopher Pierce, Matthew Gordon, Samuel Levenson, Matthew Andorf, Colwyn Gulliford and Adam Bartnik. Thanks to **my Ithaca housemates**, Dante Iozzo, Geoffrey Fatin, Thomas Wyse Jackson and Jeffrey Galczynski. Thanks to **the Finger Lakers**, and especially Grace Brown, Ava Mailloux and Christopher Christensen. Thanks to **all Sydneysiders**, most especially, Timothy and Elisabeth Smartt, Alec Sewell, Amy Lim, Nerida McCredie, Andy Owen, David Hinder, Timothy "Ninja" Dinjar, Hua Huang, Christine Wong, Rowan Kunz, Parnel Richards, Samuel Elman and Pitt Street Uniting Church. Thanks to **the University of Sydney School of Physics**, above all, Michael Wheatland, Martijn de Sterke and Andrew Doherty. Thanks to **my secondary school physics teacher**, Chris Jordison. And thanks to **Katey Collins**, whom I love and who helped me get this done.

TABLE OF CONTENTS

Biographical Sketch	iii
Dedication	iv
Acknowledgements	v
Table of Contents	vi
List of Tables	viii
List of Figures	ix
1 Introduction: how to clock fast natural processes and why you should	1
1.1 Survey of ultrafast methods	4
1.1.1 Photon probes	5
1.1.2 Electrons	11
1.2 Thesis outline	16
2 A kiloelectron-volt ultrafast electron micro-diffraction apparatus using low emittance semiconductor photocathodes	19
2.1 Note on authorship	19
2.2 Abstract	19
2.3 Introduction	20
2.4 System Description	25
2.5 Spatial Resolution	32
2.6 Temporal Resolution	38
2.7 Ultrafast Electron Diffraction	42
2.8 Summary and Outlook	45
Acknowledgements	47
3 Outrunning noise in ultrafast structural dynamics measurements with high repetition rate, high dynamic range direct detection	49
3.1 Abstract	49
3.2 Introduction	50
3.3 Methods	51
3.4 Lock-in	56
3.5 Diffusivity	59
3.6 Summary and Outlook	64
3.7 Supplemental Material	65
3.7.1 Materials and Methods	65
3.7.2 Diffusion Model	65
4 Lossless monochromation for electron microscopy with pulsed photoemission sources and rf cavities	69
4.1 Abstract	69
4.2 Introduction	70
4.3 Fundamental trade-off between energy resolution and beam current	73

4.4	Energy equalization	81
4.4.1	Qualitative summary	81
4.4.2	Correlation between emission energy, arrival time, and position	84
4.4.3	Cavity fields	89
4.4.4	Analytic prediction of cavity parameters	91
4.4.5	Simulation results	94
4.5	Jitter	101
4.6	Brightness conservation	108
4.7	Discussion and conclusion	114
4.8	Acknowledgements	116
4.9	Appendix A: Cavity field expansion	116
4.10	Appendix B: Integration by parts	118
5	Conclusion: more to learn from UED	121
	Bibliography	127

LIST OF TABLES

2.1	Routine beamline parameters for ultrafast micro-diffraction experiments.	32
4.1	Initial particle distributions assumed in all simulations. Measures of spread for each variable in particular simulation runs are indicated in the main text and figures.	95

LIST OF FIGURES

1.1	Illustration of the lower range of physical time scales: the time scales accessible with the ultrafast electron diffraction (UED) apparatus described in this thesis are at and above 10^{-13} s [1]	2
1.2	Schematic illustration of the common elements of pump probe experiments. The example experimental sample is a diatomic molecule and the vertical axis shows the relative position of the two atoms. The clock is an optical cavity, and time is measured by optical cycles. The clock triggers a pump pulse that interacts with the sample in event t_0 ; the clock triggers a delayed probe pulse. The delay is controlled by adjusting the optical path length. The probe pulse interacts with the sample in event t_1 ; methodologies differ in how the state of the sample is inferred from the transformation of the probe pulse at t_1	3
1.3	A <i>transform limited</i> optical pulse has the shortest possible pulse length allowed by the spread in frequency components: (a) a schematic spectrum of pulse energies: f_0 is the central frequency and $\Delta\nu$ is the minimum spacing between frequency components, as set by the geometry of the optical cavity; (b) an example of the pulse shape obtained by adding these components randomly out of phase; (c) a transform limited pulse obtained from the same spectrum with all components oscillating in phase.	6
1.4	Summary of how key laser technologies have enabled diverse table-top pump probe experiments.	8
1.5	Commissioning experiment to synchronize pump and probe beam. (a) The probe is beam focused upstream of the copper TEM grid, illuminating a 1 mm^2 area and casting a sharp shadow on the detector. (b) The pump beam is $10\ \mu\text{m}$ and photoemits an electron gas from the copper target. The probe beam is deflected by the gas. (c) The interaction with the probe makes a clear signal when pump-off images are subtracted from pump-on images. . .	17
2.1	(a) Schematic of the UED apparatus. The beamline consists of a 200 kV dc gun, two solenoids, a 3 GHz rf bunching cavity, the sample chamber, and a detector. The total length of the beamline is approximately 2.2 m. (b) Example data taken with the apparatus, showing a selected area electron diffraction pattern produced by a single flake of Nb_3Br_8 [136]. (c) The sample flake viewed under an optical microscope, the dark oval is a $10\ \mu\text{m}$ window through the SiN substrate.	25

2.2	<p>(a) A schematic of the laser system for the MEDUSA beamline. A 1030 nm fiber laser is used to generate both the 515 nm pump and the 650 nm photoemitting laser. The photoemitting laser is stretched with pulse stacking crystals and transported through a fiber to the cathode, to ensure position stability. The pump laser utilizes multiple feedbacked mirrors to ensure position stability. A motorized delay stage controls the relative time of arrival of the pump and probe. (b) Temporal distribution of the photoemitting laser as measured by deflecting a zero charge emitted electron beam.</p>	26
2.3	<p>(a) Top down illustration of our sample chamber, configured for ultrafast electron diffraction. We split the pump beam at the chamber entrance. The main pump path reflects off a final mirror and passes through a final focusing lens before reaching the sample. An aperture collimates the electron probe. The pump path bypasses the electron aperture and makes a 30° angle with the electron path. The other pump path, split at i., is focused by an equivalent lens onto a camera we use to track the pump position on the sample. (b) A view of a copper TEM mounted in the sample holder inside the chamber from a camera located outside the vacuum. (c) The sample holder accommodates 3 mm TEM grids, among other standard TEM sample mounts, as well as knife edges and pinholes for measuring emittance. The sample can be remotely translated transversely and up to two tilt axes.</p>	29
2.4	<p>(a) Scanning electron transmission image of our ultrafast diffraction sample, a gold film mounted on a 3 mm gold TEM grid. (b) Finer electron beam scan of a unique feature in the sample film. (c) Transmission scan of the same feature with the pump laser beam, for the purpose of verifying alignment of electron beam and pump. (d) Beam size measured at the sample plane through the final collimating aperture. There is a silicon knife edge in the sample plane, and the beam size is measured by fitting an error function to the intensity as a function of the position of the knife edge. The beam size is measured to be 3 microns rms. (e) Illustrating the two transmission modes, in red the electron beam is collimated by a 10 μm diameter aperture, in green the pump beam is steered around the electron aperture, making an angle with the electron beam of 30° at the sample plane; we perform the scan by moving the sample, shown in gold. (f) Selected area electron diffraction of the same gold sample comparing i. a 100 μm rms probe size against ii. a 3 μm rms probe size.</p>	31

2.5	Pareto fronts generated in simulation by a genetic algorithm optimizer for cathode MTEs of 25 meV (red), 150 meV (green), and 500 meV (blue) with a final bunch charge of 16 fC. The optimizer was set to minimize emittance and bunch length, holding MTE, gun voltage, and element positions constant while being free to pick operational parameters. The measured emittance and bunch length are consistent with an MTE less than 150 meV. The solid lines are included solely for the purpose of guiding the eye.	34
2.6	RMS bunch length as a function of buncher field amplitude. The minimum bunch length measured is less than 200 fs. The displayed error bars represent the mean of the individual standard errors for each measurement.	39
2.7	(a) Measurement of time-dependent photoemitted plasma lensing, showing the rms per pixel change in beam intensity as a function of time. (b) Schematic of the mechanism that drives the beam response, i. pump laser photoemits an electron gas from a copper grid, ii. Coulomb field from emitted gas deflects the electron beam. (c) Example of the detected difference image used to compute the signal plotted in (a).	40
2.8	Time-dependent diffraction from a gold sample pumped by 515 nm light. Each panel is a composite of 100 acquisitions at a 5 s exposure time and 5 kHz electron beam repetition rate, taken at a fixed pump delay indicated by the inset text.	41
2.9	Bragg peak intensity as a function of pump delay. Peak intensities are estimated from the data shown in Fig. 2.8 by taking the maxima of Gaussian filtered images. The quantity plotted is the change in this intensity normalized by its fully-relaxed (pump-probe delay 100 microseconds) value. (b) Simulated signal as a function of sample thickness including multiple scattering effects, assuming a cold temperature of 273 K and a hot temperature of 423 K; colors have the same meaning as in panel (a), dashed line indicates a thickness that reproduces qualitatively the dependence on scattering angle in the experimental data, values along this line are plotted as asterisks in panel (a).	44
2.10	(a) Scattering intensity as a function of the magnitude of the scattering vector and pump delay time; the data are calculated by averaging the images in Fig. 2.8 over the azimuthal coordinate, centered on the primary peak. (b) A comparison of two cross sections of panel (a), showing explicitly the percentage change in scattering intensity as a function of the magnitude of the scattering vector; the dashed curve corresponds to the cross section indicated by a dashed line in panel (a), likewise the solid curve. .	46

3.1	(a) Schematic of the UED beamline, see reference [1] for details: a 1030 nm Yb-fiber laser drives an optical parametric amplifier that sends 650 nm light pulses to the photocathode; photoemitted bunches are accelerated to 140 keV, compressed by an rf cavity, collimated by a probe-defining aperture, and are collected by the detector after scattering on the sample; the same 1030 nm pulses are split and frequency doubled to synchronously pump the sample. (b) Modification of the detector section of the beamline to accommodate a magnetic quadruple electron lens triplet. The lens triplet enables angular magnification of the scattering pattern. A diffraction feature is selected for magnification on the detector with a steering magnet upstream of the lens triplet. . . .	53
3.2	Schematic of the pump-probe technique in time; the period between pulses is 8 μ s and exaggerated here for clarity; the duration of the pump-pulse train is controlled by an acousto-optic modulator; an optical delay stage controls pump-probe delays from 100 fs to 1 ns and detector exposure timing controls pump-probe delays > 1 μ s. The dashed waveform shows whether exposures are added or subtracted in integrating the pump-probe signal. The solid waveform represents the microsecond-scale temperature envelope predicted by Eq. (3.2).	54
3.3	(a) Schematic of the spatial scanning technique used to collect the data plotted in Fig. 3.5: a 10 μ m aperture defines the size and position of the probe in the sample plane; pump pulses are scanned horizontally across the sample. (b) Optical microscope image of the sample, contrasting 10 nm thin windows hosting the heterobilayer on SiN substrate with Si holder-heat sink.	55

- 3.4 (a) Logarithmic scale diffraction pattern obtained from $\text{WSe}_2/\text{MoSe}_2$, demonstrating the EMPAD dynamic range. Highlighted in white, a long camera-length diffraction pattern showing a single, vertically aligned pair of Moire Bragg peaks: also visible, a pair of horizontally aligned satellite peaks, with 10 nm periodicity. Detector camera length is varied with a magnetic quadrupole lens triplet downstream of the sample (see Fig. 3.1). (b) Measurement uncertainty as a function of lock-in frequency: referring to the variance-to-mean ratio (VMR) defined in Eq. (3.1), the vertical axis shows $\sqrt{\text{VMR}}$ and can be interpreted as the ratio of total uncertainty to the shot noise limit set by the total integration time. Two curves compare different rates of scattering into the selected Bragg pair shown in (a); the different rates are obtained by increasing the radius of the probe defining aperture. (c) Measurement of the ultrafast Debye Waller effect, comparing data quality with high and low lock-in frequencies, each data point integrated for two minutes. 58
- 3.5 Sample thermometry performed at ps- μ s- μ m scales. The timing system, scanning technique and sample are shown in Figs. 3.2, 3.3. (a) The vertical axis shows the relative change in diffraction intensity, $\Delta I/I$, of the second-order Bragg pair highlighted in Fig. 3.4. The bottom horizontal axes show the displacement of the pump beam relative to the probe. Pump delay is indicated on the top horizontal axis: vertical gray arrows point to the delay at which each spatial scan is performed. The data plotted at 0 μ s show the ultrafast response of the sample to heating by the 515 nm, 2mJ/cm² pump laser after a 20 ps delay. Most of the energy deposited by one pump pulse is dissipated before the arrival of the next, but a residue remains trapped. To resolve the ramping of temperature as this residual energy accumulates over multiple pump pulse, we vary the length of the pump pulse train, up to a maximum of 440 μ s. Holding the pump pulse train length fixed at 440 μ s, we continue to increase the delay and spatially resolve the dissipation of energy to the sample boundaries. Pump trains cycle at 250 Hz, and we fit a steady-state, periodic diffusion model to the data described in Eq.(3.2) and following body text. Solid lines show the spatial temperature profiles predicted by the model at each delay, and the dashed line shows the temperature predicted by the model at the sample center. (b) Visualisation of the model, solid lines show contours of equal relative change. Vertical lines show the cuts at which spatial scans are performed, colors match the corresponding data in panel (a). 62

4.1	(a) Energy selecting monochromator as described in [206]: magnetic prisms disperse the energy spectrum of the electron beam in the transverse direction and a narrow acceptance slit selects the desired bandwidth at the cost of lost current. (b) Our lossless monochromator design: photoemission is triggered by a laser pulse and the beam energy spectrum disperses in the longitudinal direction. Time-correlated acceleration in the pair of cavities, indicated by force vectors in the figure, equalizes the energies of the dispersed beam. The average current in our design is limited by the cavity frequency.	75
4.2	Normalized energy gain versus the single particle time of arrival, expressed as a fraction of the full rf period. The quadratic coefficient of the energy gain is subtracted, leaving only unwanted higher-order terms. Vertical lines show the initial pulse length Δt_ℓ (solid) and final pulse length Δt_f (dashed). The duty cycle in Eq. (4.2) is $f\Delta t_f$. Inset shows the full sinusoidal energy gain versus the scaled time of arrival, with the quadratic term restored.	77
4.3	(a) Simulated source and monochromator layout in the x - z plane. The left axis is the transverse scale for the optical elements. All elements are axially symmetric. The transverse beam size is shown by the green curve, with the scale indicated by the axis on the right. The cathode and anode are at $z = 0, 10$ mm, respectively. At $z = 50$ mm is a focusing solenoid; at $z = 160, 240$ mm, dumbbell silhouettes approximate cavity cross sections. (b) Electrode profile and axial field $E_z(z)$ in the gun for a voltage of 50 kV.	82
4.4	Evolving correlation between the energy, radial position r , and time of arrival Δt in a dc electron gun. Results plotted are of single particle trajectory simulations. The accelerating field is uniform with a gradient of 5 MV/m. Each subplot shows the cross section of radial position and time of arrival at the exponentially increasing values of z indicated on the top axis. Color indicates particle energy $\Delta\mathcal{E}$ relative to the minimum energy in the statistical ensemble; Δt is defined relative to the last arriving particle. As the uncertainty in time and position grows, the correlation with energy tightens. Uncertainty in time of arrival asymptotically approaches the value predicted by Eq. (4.5) as the energy gained in acceleration comes to dominate the initial kinetic energy. The initial statistical ensemble in all our simulations, unless otherwise specified, is uniformly distributed in energy, time of emission, and solid angle over the forward hemisphere [214]. .	83
4.5	Cross section of the 3 GHz TM010 mode cavity used in the energy equalization device described in this paper.	84

4.6	Simulation cavity field map: (a) z, r cross section of the radially symmetric cavity \mathbf{E}^{rf} field at nominal amplitude and phase; (b) the axial cavity field $E_{0,z}^{\text{rf}}$ and its leading spatial derivatives, from which we construct the simulation field map.	89
4.7	Simulation of a beam with $\Delta t_l = 30$ fs and only longitudinal momentum spread. Transverse size and momentum spread are set to zero. In (a), an idealized, uniform field gun is used. In (b), the realistic gun field shown in Fig. 4.3 is used. Blue points denote the energy-time correlation just after the gun. Red points show the result after transiting a single cavity with amplitude set by the solution of solution of Eq. (4.20). White lines are the predictions of Eq. (4.11) and Eq. (4.24), where in (b) we use the field at the cathode for E_z^{cat}	96
4.8	Simulation of a beam with initial size $\sigma_x = 12$ nm and nonzero transverse momentum spread. Here the beam has no longitudinal momentum spread and has zero duration. Blue points show the energy-space correlation just after the gun, and red points show the result after transiting a single cavity with amplitude set by Eq. (4.21). The white line is the prediction of Eq. (4.11). Due to thick lens effects, the cavity settings predicted by Eq. (4.21) slightly overcorrect the energy-space correlation. The green curve is the result of numerical optimization of the cavity amplitude.	98
4.9	Simulated evolution of energy correlations on transiting two rf cavities, with an initial energy spread of 1 eV, vanishing initial transverse source size, and vanishing initial pulse length: (a) post gun but before the first cavity, the paraboloid distribution predicted by Eq. (4.11); (b) between the two cavities, the first cavity imparts a hyperboloid distribution as predicted by Eq. (4.18), with energy increasing in time and space; (c) after the second cavity, the residual energy spread involves cubic corrections to Eq. (4.11), shown in Eq. (4.12).	99
4.10	Results of simulating the beamline shown in Fig. 4.6(a). Particle ensembles initially have uniform energy spreads of 1 eV, distributed uniformly in solid angle over the forward hemisphere. Results for two accelerating voltages are shown, 10 kV (blue), 50 kV (red). Dashed horizontal and vertical lines indicate the FWHM.	101

4.11	Simulation results showing beam sizes and emittance as a function of beamline position for three different initial energy spreads; all particle ensembles have initial transverse size of 12 nm rms and momenta distributed uniformly over the forward hemisphere; with initial uniform energy spreads of 1 eV (red), 500 meV (blue), and 250 meV (yellow). Cavity settings are chosen to achieve the smallest final energy spread. (a) Transverse normalized emittance; (b) rms energy spread; (c), (d) rms pulse duration.	102
4.12	Simulated energy distribution in the presence of white rf phase noise at the same 5 fs rms scale reported experimentally in [145]. Four sets of initial conditions are shown, with initial energy spreads of 1 eV in all. Colors indicate two sets of primary energies: 50 keV (blue), 100 keV (red). Line style indicates the initial pulse length; 30 fs (solid line), 200 fs (dotted line). (a) Probability density per meV downstream of the rf monochromator. Inset shows the distribution of the timing noise in the simulation, with the noise identically and independently distributed in each cavity. (b) Cumulative probability density with dashed horizontal lines indicating interquartile range. (c) Probability of time of arrival per picosecond relative to the mean, downstream of the gun.	103
4.13	Simulations of cavity timing jitter. The initial particle ensemble has a uniform 1 eV energy spread distributed uniformly in solid angle over the forward hemisphere. Plots show the ensemble after transiting two 3 GHz cavities with timing offset from the optimal solution by ϕ_1, ϕ_2 respectively. Offsets add in quadrature to 10 fs. At left, histograms of final energy show single meV movement in peak location and 10 meV scale movement in tails. On the , energy-time correlation are shown as a function of cavity phase, where different phases are offset on the time axis for clarity.	107
4.14	Correlations between particle divergence and time of arrival in particle tracking simulations of a uniform accelerating gradient of 5 MV/m. The initial conditions of the particle distribution are a 1 eV uniform energy spread distributed uniformly in solid angle over the forward hemisphere, and vanishing transverse size and pulse length. The time-dependent divergence predicted by Eq. (4.37) are shown by the white lines at constant time increments of 50 fs.	111

5.1 Computing a real-space image with diffraction data. (a) The diffraction pattern of an atomic lattice is not unique. (b) By performing selected area diffraction of overlapping subregions of a sample, it is possible to solve for the real-space atomic configuration. This *ptychography* technique might allow more flexibility in mitigating Coloumb forces and thus achieve higher resolution ultrafast electron imaging. 124

CHAPTER 1

INTRODUCTION: HOW TO CLOCK FAST NATURAL PROCESSES AND WHY YOU SHOULD

The electron diffraction apparatus described in this thesis is, among other things, a clock with a timing precision of 10^{-13} s [1]. To put this number in a wide context, the timescales of natural processes span over 40 orders of magnitude, from 10^{18} s — the age of the universe — to 10^{-25} s — the lifetime of the W boson [2, 3]. The experimental uncertainty in the latter quantity is order 10^{-27} s. Thus, while the precision of our clock is an engineering feat, it is not physically extreme: one clock-tick is as long compared with the W lifetime as the age of the universe is to one day on Earth. At the physical extremes, scientists do not measure time with clocks. Instead, a parameter with units of time appears in a mathematical model of the process, which is fit to data acquired in a time-independent experiment. For example, the W lifetime is estimated from the measured energy spread of the particle's decay products. These examples and others illustrated in Fig 1.1 perhaps suffice to raise skepticism about the scientific need for fast clocks. Are there science discoveries at *ultrafast* timescales (faster than 10^{-9} s) that can only be made by measuring time with a clock, and not inferred from other available data? This introduction aims to answer that basic motivational question in the affirmative. It then surveys the developments in ultrafast science that serve as the context for the contribution made by this thesis toward improving techniques for performing ultrafast pump-probe experiments with high brightness electron beams.

The elements common to any pump-probe experiment, including the clock, are illustrated schematically in Fig. 1.2. Denoting the physical system under in-

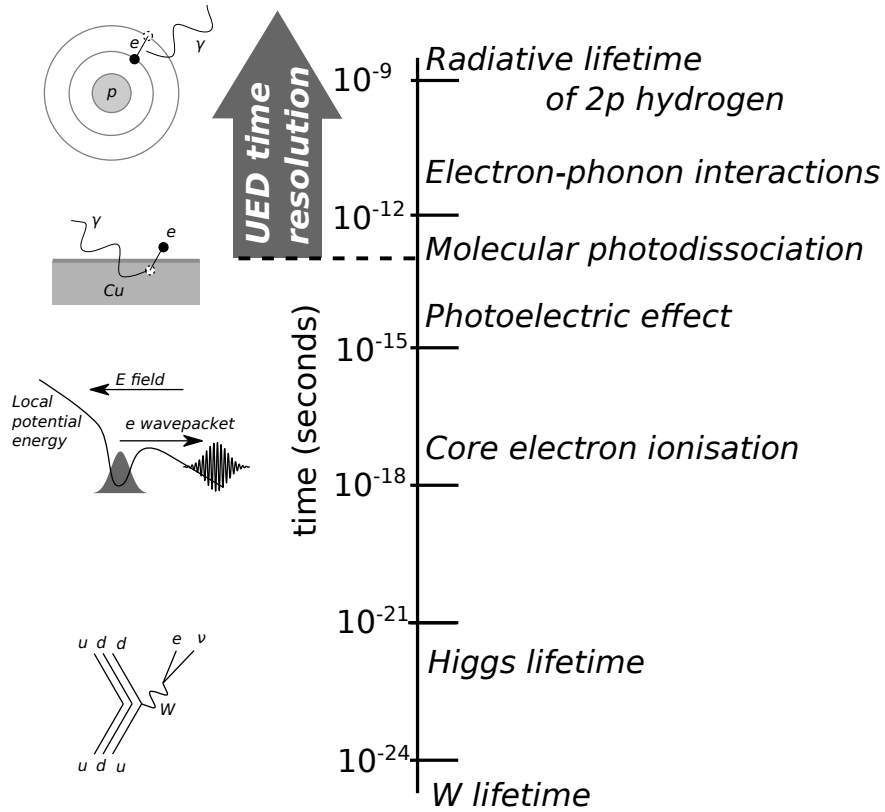


Figure 1.1: Illustration of the lower range of physical time scales: the time scales accessible with the ultrafast electron diffraction (UED) apparatus described in this thesis are at and above 10^{-13} s [1]

investigation *System A* (a diatomic molecule in the example illustrated by Fig. 1.2, see reference [4]), a *clock* is a second, periodic system, *System B*, e.g., a light pulse bouncing between two mirrors of an optical cavity [5]. The experimenter brings *System B* into causal contact with *System A*, e.g., by allowing a light pulse that exits the cavity to interact with *System A*. A first *pump* pulse prepares the initial state of *System A* in an interaction event t_0 , representing the start of the clock timer. A second *probe* pulse reads the state of *System A* in an interaction event t_1 , which stops the clock timer. Crucially, with a clock, knowledge of the time interval between t_0 and t_1 can be acquired without needing to assume a model of *System A*. The experimental protocol is in this sense a more direct measurement

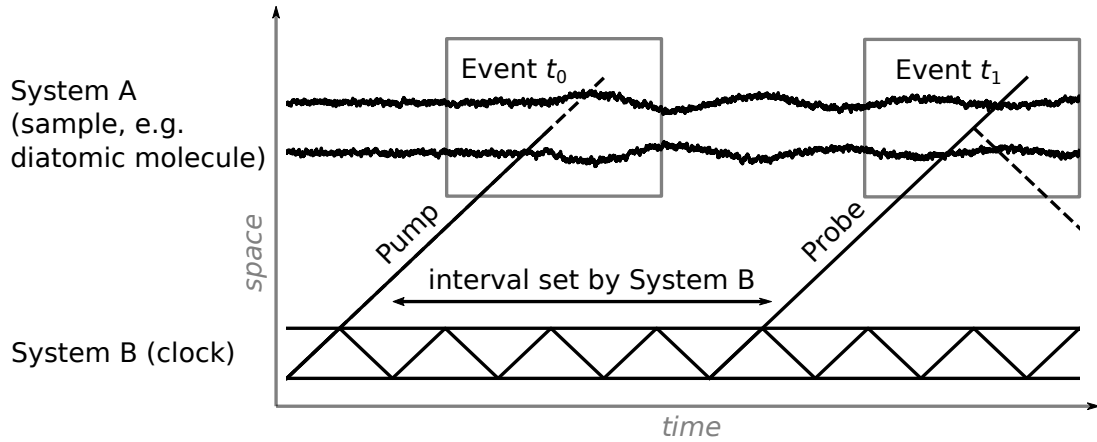


Figure 1.2: Schematic illustration of the common elements of pump probe experiments. The example experimental sample is a diatomic molecule and the vertical axis shows the relative position of the two atoms. The clock is an optical cavity, and time is measured by optical cycles. The clock triggers a pump pulse that interacts with the sample in event t_0 ; the clock triggers a delayed probe pulse. The delay is controlled by adjusting the optical path length. The probe pulse interacts with the sample in event t_1 ; methodologies differ in how the state of the sample is inferred from the transformation of the probe pulse at t_1 .

of the time interval as compared with a parametric fit.

A clock is informative if and only if the model of System B can be experimentally validated with greater confidence than the model of System A. Thus, in a case as profoundly simple (counting degrees of freedom) as estimating the lifetime of the W boson, a clock is both infeasible and redundant. As another illustration of the same point, in the commissioning experiments reported in Chapter 2 of this thesis, we begin with higher *a priori* confidence in our model of System A — say, photoemission from a copper grid — than System B, and thus the source of information is flipped: System A supplies information about the timing of events in System B.

Clocks are most useful, even essential, in cases where System A is complex (counting degrees of freedom), for example, condensed matter systems out of equilibrium [6–10], chemical reactions involving multiple pathways through intermediate states [11–14], and biological systems [15–20]. Complexity means that to construct a model of System A must involve making simplifying approximations and intelligent guesses, liable to be disproved by model-agnostic measurements. Femtochemistry provides the morality tale here, as retold by A. Zewail in his Nobel prize lecture [21]. Zewail quotes another Nobel laureate, Manfred Eigen, to the effect that no *interesting* dynamics occurs in chemical reactions at timescales faster than 10^{-6} s. Zewail’s data, clocked to 10^{-13} s precision, showed Eigen was mistaken, at least in the judgment of the Nobel committee.

1.1 Survey of ultrafast methods

A fast clock is common to all pump-probe experiments. It is convenient to categorise different methodologies based on the particle species of the probe. The following survey of probe species and their capabilities aims to provide the necessary context for understanding the scientific value of dedicated electron diffraction machines in particular. A common metric for quantifying probe quality is *brightness*, the particle number per unit phase space volume, which is inversely related to the spread in particle trajectories that comprise the beam. A narrow spread — thus high brightness — is almost always desirable. In ultrafast experiments, the relevant phase space is six-dimensional and consists of the transverse beam momentum and size, as well as the pulse length and spread in forward momentum. Formal definitions of brightness vary as to the beam statistic that quantifies spread (e.g., root-mean-square or full-width-at-

half-maximum): for the purpose of this introductory review, it is not necessary to make a choice of convention (but see Chapters 2, 4 and references [22–24]).

1.1.1 Photon probes

Optical photons

The main stream of pump-probe techniques all rely on lasers as the clocking component. Some examples that connect tabletop pump-probe experimental techniques with developments in laser technologies are shown in Fig. 1.4. This survey of methodologies begins with the invention of the ruby laser in 1960 [25], and the technique for nanosecond pulsed operation first reported in 1962: *Q-switching* [26]. Electronic activation of the Q-switch interrupts the lasing process much like a mechanical shutter placed inside the optical cavity. A laser pulse is formed by opening and closing the switch. Time-resolved absorption spectroscopy experiments with a Q-switched ruby laser and 10^{-8} s resolution were performed in 1967 [27]. This early work illustrates many pump-probe concepts and the experimental technique is worth a brief description. A white-light probe transmitted through the sample is dispersed and a detector records gaps in the spectrum caused by absorption. Critically, the probe is intense enough that a spectrum can be recorded in a single pulse with energy resolution adequate to resolve time dependent features. To make the probe pulse, the 694 nm ruby laser light is focused on a gas cell. The photoionisation of the gas creates a white spark that, depending on the gas species, can be as short as 10^{-8} s. The pump-pulse is formed by frequency doubling the ruby fundamental.

The physical limit on laser pulse length is set by the reciprocal relationship

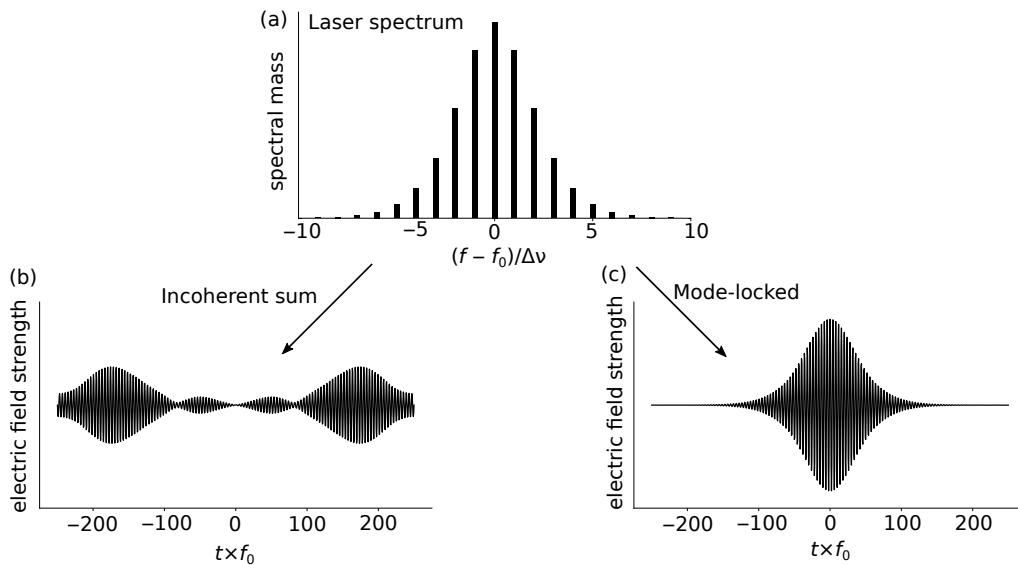


Figure 1.3: A *transform limited* optical pulse has the shortest possible pulse length allowed by the spread in frequency components: (a) a schematic spectrum of pulse energies: f_0 is the central frequency and $\Delta\nu$ is the minimum spacing between frequency components, as set by the geometry of the optical cavity; (b) an example of the pulse shape obtained by adding these components randomly out of phase; (c) a transform limited pulse obtained from the same spectrum with all components oscillating in phase.

between energy and time. If the spread of energy in the laser beam is ΔE then the shortest *transform limited* pulse length is $\Delta t = \hbar/\Delta E$. To reach the transform limit, the energy components of a pulse must oscillate in-phase with each other, as illustrated in Fig. 1.3 [28]. *Mode-locking* techniques to maintain the correct phase relationship were first demonstrated in dye lasers in the 1970s [29, 30]. Within a few years, picosecond pulsed dyes layers were deployed to perform ultrafast pump-probe experiments [31]. By the mid 1980s, dye lasers could produce pulses shorter than 10^{-14} s [32, 33], and systems following this design pattern were deployed in the same decade by the Zewail group to perform the fem-

tochemistry experiments for which the Nobel prize was awarded in 1999 [21]. Also in the 1980s, the development of femtosecond solid state lasers, particularly titanium:sapphire, was a key breakthrough that increased practically and thereby expanded the range of feasible ultrafast experimental techniques [34]. Today, commercial fiber lasers provide turn-key sub-picosecond pulses [35], and the shortest laser pulses achieved in laboratory experiments are 4×10^{-17} s [36].

An important parallel development to shorter pulse lengths is higher pulse energy. Higher pulse energy makes the laser a more versatile tool by unlocking energy-conversion processes that can transform a seed pulse into a variety of pump and probe pulses. Terahertz pump pulses are an example: this frequency band is scientifically interesting because it matches the typical energy of collective motion in solids [37]. There are no known amplification processes lying in the same band (aside from free electron lasers) and thus, to obtain terahertz pump pulses, non-linear frequency conversion of a high-power optical seed is necessary. However, it is physically challenging to combine high pulse energy with short pulse length. The key technical breakthrough, again made in the 1980s, was the development of chirped-pulse amplification [38].

The scientific advantage of optical probes is that the particle energy belongs in the same band as the transition energies of electronic degrees of freedom in molecules and solids. The interaction with the sample results in some fraction of the pulse energy being transmitted, some reflected, and the remainder absorbed. Information can be obtained by measuring transmitted and reflected power; there are multiple other indirect techniques for measuring the absorbed energy, such as reading a photoionisation current [39]. The disadvantage of optical probes is that their wavelengths are too long to resolve inter-atomic dis-

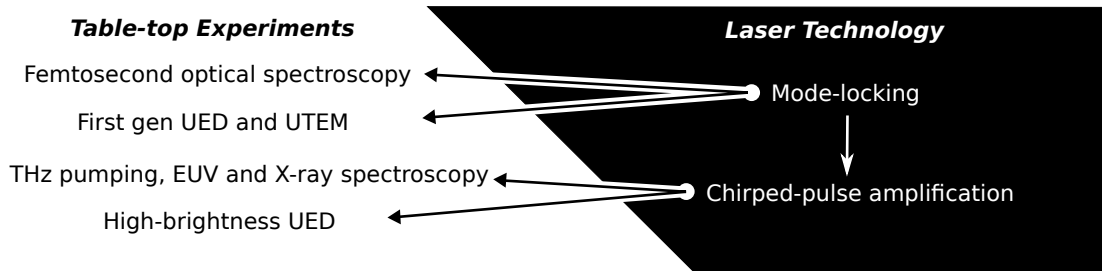


Figure 1.4: Summary of how key laser technologies have enabled diverse table-top pump probe experiments.

tances in diffraction or microscopy. Thus, *structural probes* that give information about atomic positions must either be x-ray photons or massive particles.

X-rays

Photons capable of resolving inter-atomic distances must have energies at and above 1 keV. It is possible to generate x-rays with these energies in a table-top experiment by driving x-ray emission with a femtosecond laser [40–43], and in this way achieve femtosecond time resolution. The brightest sources of keV x-rays are electron storage rings and free electron lasers (FELs) [44]. Synchronising pump pulses with conventional storage ring light poses a unique challenge [45, 46]. *Laser-electron slicing* is a storage-ring technique in which a femtosecond laser pulse modulates the energy of a subset — slice — of electrons in a stored bunch [47, 48]. The pumped electrons can then be dispersively selected in order to generate femtosecond x-ray pulses. The cost of laser-electron slicing is a loss of total flux.

Free electron lasers provide femtosecond x-ray pulses at higher-flux and brightness, making it possible to perform spectroscopy on inelastically scat-

tered x-rays and measure other weak signals that are only detectable with a large number of probe particles [49–51]. All industrial and most laboratory lasers rely on electrons bound to neutral matter in gas, liquid or solid phase to produce electromagnetic radiation. A quantitative treatment of electron orbits inside these gain media requires quantum mechanics, which gives the mistaken impression that lasing is an inherently quantum mechanical process. Free electron lasers are the exception: the radiating electrons in a free electron laser follow classical trajectories. The force that makes FEL electrons oscillate is supplied by externally applied, macroscopic magnetic fields. Lasing occurs in an FEL because a back-reaction to the co-propagating electromagnetic radiation causes electrons in a bunch to oscillate in-phase with each other: classical stimulated emission [52]. The process saturates when the transfer of energy from the electron bunch to the electromagnetic field is large enough to push electron trajectories off resonance. Machines produce radiation at various wavelengths, including infrared [53], optical [54], soft [55, 56], and hard x-rays [44, 57]. The gain bandwidth goes roughly like the electron beam-brightness, so exceptionally bright electron beams are required for efficient amplification at hard x-ray wavelengths, and this brightness is achieved by accelerating to ultra relativistic energies.

In existing hard-xray FELs, the timing of x-ray pulses is governed by the phase of the radiofrequency (rf) cavities that accelerate the electron beam. If the sample is pumped at a different wavelength than the probe, it must be by an independent laser system, and rf feedback is then able to synchronize pump and probe pulses to within 10^{-12} s. Monitoring the time of arrival of electron bunches at points along the beam-line can tag x-ray pulses shot-by-shot to within 10^{-14} s [58]. In this way, experiments randomly sample pump-probe delays to 10^{-14} s

precision from within a 10^{-12} s window and the experimenter has control over the center of the window.

The situation is improved when the x-ray laser supplies the pump pulse. In one such experiment, an attosecond x-ray pump pulse ionizes electrons in a gas target, while a circularly polarized infrared probe pulse delivers a time-dependent radial kick to the liberated photoelectrons [59]. This kick imprints a correlation between a) the azimuthal angle at which photoelectrons arrive at a phosphor screen and b) the time of photoemission. The photocurrent from the high intensity x-ray pulse is sufficiently large that the phase of the probe pulse can be reconstructed in a single shot and, in this way, 10^{-16} s time resolution achieved. Other novel approaches to improve FEL time resolution in specifically x-ray pump, x-ray probe experiments are an active topic of research: see, e.g., reference [60].

Though x-ray sources are formidable science discovery machines, they nonetheless suffer from disadvantages, providing the motivation for electrons as the preferable structural probe in some important applications. X-rays have a much lower scattering cross-section for equivalent reciprocal space resolution, so that obtaining a good diffraction signal can require penetrating samples to depths as much as 10^{-4} m [61]. Good signal in electron diffraction, on the other hand, can be obtained from a single atomic monolayer: see Chapter 3 of this thesis. Electrons are thus ideal for studying the rapidly expanding category of 2D quantum materials, of which graphene is the prototypical example.

A deep penetration depth introduces two further, significant complications in pump-probe x-ray diffraction. First, the extinction length of an optical pump pulse can be order 10^{-8} m, so that most of the x-ray scattering volume is never

excited and thus pollutes the pump-probe signal. Second, the propagation velocity of electromagnetic waves in media is frequency dependent, so that even if an infrared or optical pump does penetrate deeply into the material, the pump and probe inevitably slip past each other, setting a physical limit on the temporal resolution.

To round out this discussion, an advantage of a larger scattering volume is that x-rays can serve as cleaner probes of the bulk structure of a sample than electrons. After relatively few atomic layers, electrons are significantly affected by multiple scattering, which complicates the interpretation of diffraction data: see Chapter 2 of this thesis.

1.1.2 Electrons

Diffraction

Electrons accelerated above 100 eV have the right wavelength to probe interatomic distances. In converting an ultrafast laser pulse into an electron pulse, there are multiple processes that blur the temporal resolution, but the most significant is Coulomb repulsion between emitted electrons. The dominant theme in the following summary of developments in ultrafast electron probes is how best to compensate the deleterious effects of Coulomb forces.

The technology for ultrafast conversion of light energy to electric current was first developed to build x-ray streak cameras [62]. In this design, an x-ray pulse arrives at one side of a vacuum diode: a deflecting field is pulsed so that the position at which photoemitted electrons are detected corresponds to the time

of photoemission. The first device to report ultrafast electron diffraction (UED) was constructed by modifying a streak camera [63]: the diffraction apparatus converted a 10^{-11} s UV light pulse into a 10^{-10} s electron bunch at the sample location. Machines that have since iterated on this design are characterized by metal photocathodes, accelerating voltages below 100 kV, few electron lenses and bunch charges of less than 10^4 electrons per pulse at the cathode [7, 64, 65]. Thanks to their simplicity, these machines are highly practical and continue to make science discoveries today [66], and can reach a time resolution of 100^{-13} s [65]. However, a more complex design is needed to overcome Coulomb forces and simultaneously produce a) bunch charges above 10^4 electrons per pulse at the cathode, and b) bunch lengths at or below 10^{-13} s at the sample.

There are broadly two strategies for mitigating Coulomb repulsion in the current generation of diffraction machines. One strategy is to accelerate to relativistic energies, which results in magnetostatic attraction almost perfectly compensating electrostatic repulsion [67–70]. The second strategy is to compress bunches following acceleration [1, 71–75], investigated in greater detail in Chapter 2 of this thesis. In principle, relativistic primary energies could be combined with bunch compression, a technique employed in FELs but not as yet for UED [76].

Microscopy

A second key modality for electron probes beside diffraction is *transmission electron microscopy* (TEM). As an imaging modality, the electron optics in a microscope are necessarily more complicated than a dedicated diffraction apparatus. A particular challenge when Coulomb forces are at play is that the beam is

brought to a *crossover* waist at multiple locations in the microscope column to achieve the desired illumination conditions and magnification. Typically, the formation of crossovers limits the beam current at the sample to one electron per pulse: see e.g., the beam currents on target cited in reference [77], and the study of pulse-length broadening in reference [78].

Single shot microscopy at sub-relativistic energies, time resolved to 10^{-8} s and christened *Dynamic* TEM, was demonstrated in 2000 [79], and further developed in that decade [80, 81]. Contemporary efforts towards single shot ultrafast TEM (UTEM) are pursuing relativistic beam energies as the strategy for overcoming Coulomb forces [82, 83]. Relativistic energies in static TEM are not widely employed because these beams cause significant radiation damage [84], but doses are reduced in single-shot operation and data can be acquired before the onset of radiation damage.

At the sub-relativistic energies typical of conventional TEM, the emphasis among ultrafast microscopists has shifted to stroboscopic UTEM [85]. Experimental highlights include: making a bright-field, real-space, real-time moving image of the propagation of a strain wave with 10^{-7} m wavelength and 10^{-11} s period [86], employing dark field and diffraction contrast to make a real-space, real-time moving image of the onset of a structural phase-transition [87], Lorentz force UTEM imaging of the evolution of magnetic singularities [88], and energy filtered UTEM imaging and ultrafast electron energy loss spectroscopy for studying non-linear light-matter interactions [89–91].

Coulomb forces cause both temporal and spatial resolution to deteriorate in UTEM. The following story captures the elements of the problem, while omitting the details of the variety of ways image contrast can be obtained in electron

microscopy. In transmission mode, to obtain the best contrast, microscopists seek to make the illuminating beam appear at the sample *as if* it originated from a point source [92]. The effective source size can always be reduced by restricting the size of apertures in the path of the beam, but at the cost of reduced average beam current. Aperture sizes that eliminate 99% of the beam are typical. At lower beam current, the system is more sensitive to low frequency jitter, including slow drift in the sample position on the atomic scale. This low frequency noise eventually washes out the contrast that would otherwise be gained by tightening the aperture. Even in the regime where the average current on the sample is one electron per pulse, selection of electrons for either high spatial or momentum resolution requires emitting orders of magnitude more charge at the cathode than arrives at the sample. Hence, Coulomb repulsion at the photoemitting tip and first crossover, by increasing the effective source size, blurs the imaging resolution. These difficulties motivate efforts to explore the possibility of numerically reconstructing a real space image from UED data, an extension of *ptychography* techniques successfully demonstrated in static experiments [93].

Ultimate limits on time resolution

Coulomb forces are also an obstacle to producing electron beams with transform limited pulse length. The transform limited pulse length of an electron beam with 200 keV primary energy and a *coherently added* energy spread of 1eV is less than 10^{-18} s, whereas the shortest pulses achieved experimentally are 10^{-17} s [94]. The leading strategy for achieving 10^{-18} s electron pulses is to emit a long, low energy spread pulse at the cathode and, following acceleration, compress this

long pulse in an interaction with an optical wave. The *a priori* scientific case for stroboscopic *structural* probes with 10^{-18} s resolution is unconvincing, because a stroboscopic modality can only study reversible processes and the energies involved in reversible processes for typical samples imply atomic motion on the 10^{-12} s timescale. However, by resolving the energy spectrum of the transmitted electron beam, it is possible to measure energy transfer from the probe to the sample's electronic degrees of freedom. Electron energy loss spectroscopy (EELS) with attosecond pulse lengths could therefore probe the 10^{-18} s timescale of electronic transitions involved, e.g., in non-linear light-matter interactions, such as higher-harmonic generation (for an alternative method of probing these processes, see, e.g., [95]).

The unique role of UED

The foregoing discussion has shown that each probe particle species has its own special capabilities, as well as limitations. There is therefore a unique scientific role for UED at 10^5 eV primary energies. In particular, as compared with UTEM, a dedicated diffraction apparatus has available more effective strategies for mitigating Coulomb repulsion, allowing for much larger beam currents while maintaining short pulse lengths. Electron diffraction is therefore especially sensitive to weak pump-probe signals. Larger beam current can also be traded-off for much more aggressive electron selectivity, which provides the fine momentum resolution to resolve long-wavelength correlated motion in the sample, as is demonstrated in Chapter 3 of this thesis.

1.2 Thesis outline

This thesis describes the commissioning (Ch 2), first science results (Ch 3) and possible future upgrades (Ch 4) of a high-brightness electron diffraction apparatus. It is a compilation of two “first author” publications and a first author manuscript prepared for publication.

The design and commissioning of the apparatus is described in Chapter 2. Emphasis in Chapter 2 is placed on the single micron sized diffraction probe. The chapter highlights the merits of a small probe by reporting UED experiments performed on a mosaic gold film. The small probe is able to resolve in diffraction the contribution of distinct mosaic domains. An important challenge in commissioning the apparatus is to locate the zero of time, t_0 , that is, to vary the pump path length so that the probe and pump pulses arrive at the sample simultaneously. The total pump path length is 20 m and thus must be calibrated to one part per million in order to time the system to the 10^{-13} s precision of the instrument response. Results of our first success in locating t_0 to picosecond precision are shown in Fig. 1.5. The signal, plotted in Fig. 1.5(c), is provided by the pump-induced photoemission of an electron gas from a copper grid. A noteworthy feature of the signal is its 10^{-10} s decay timescale, which implies that this method is practical only if the correct path-length is already known to centimeter precision. We performed experiments exploiting the much longer thermal relaxation of our gold sample to find t_0 to within 10^{-9} s. As compared with the results in Chapter 2, the experiment reported in Fig. 1.5 employs a millimeter size probe beam that is orders of magnitude larger than the pump spot. It is desirable when performing UED that the probe beam be smaller than the pump so as to maintain uniform pump illumination over the probed sam-

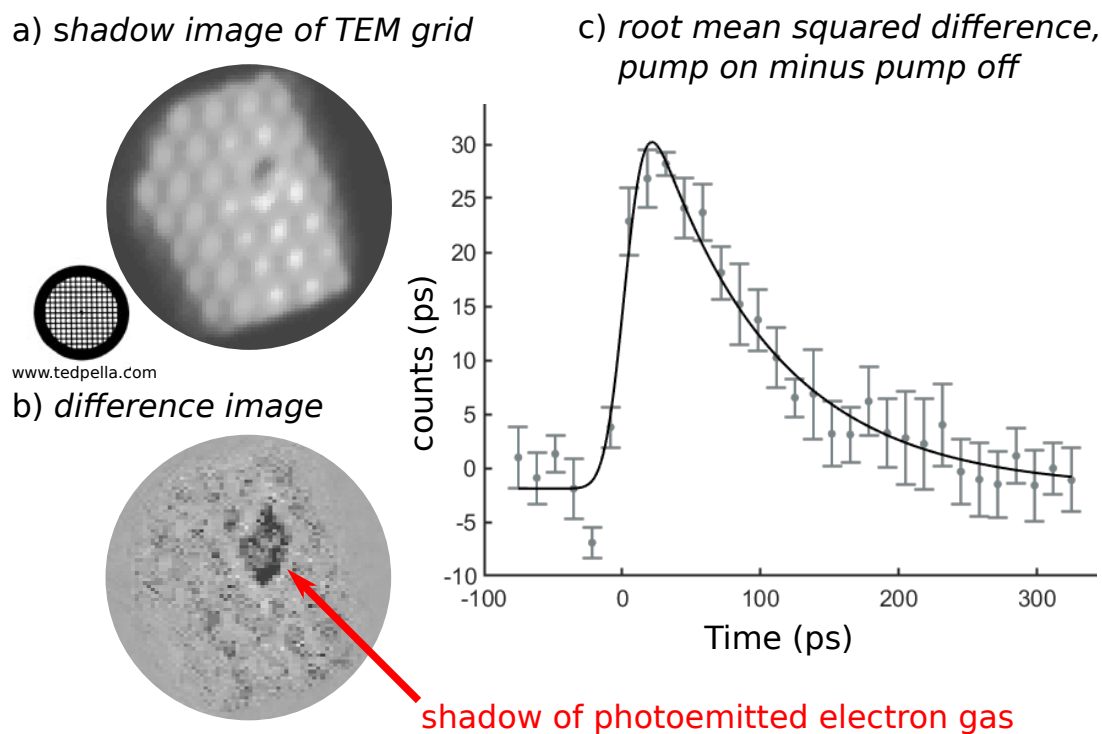


Figure 1.5: Commissioning experiment to synchronize pump and probe beam. (a) The probe is beam focused upstream of the copper TEM grid, illuminating a 1 mm^2 area and casting a sharp shadow on the detector. (b) The pump beam is $10 \mu\text{m}$ and photoemits an electron gas from the copper target. The probe beam is deflected by the gas. (c) The interaction with the probe makes a clear signal when pump-off images are subtracted from pump-on images.

ple area. However, in a t_0 experiment, a significantly larger probe eliminates the need for careful spatial alignment of the two beams. Chapter 2, Fig. 2.7 reports a similar experiment but with a micron size probe that enables a precise measurement of the probe beam's deflection angle, useful for investigating the evolution of the photoemitted gas.

Chapter 3 reports the first science results obtained with the diffraction ap-

paratus. Science data collection is enabled by a direct electron detector with kilohertz framerate and high dynamic range. Chapter 3 shows that the diffraction apparatus, when equipped with this detector, is able to reach the minimum experimental uncertainty set by the integer number of electrons per beam pulse.

Chapter 4 describes the design of an electron monochromator, which could be built and deployed in the future to perform high-precision EELS. Elastic scattering angles contain information about the position of atomic nuclei in the sample, but not about the electronic degrees of freedom that compose the chemical bonds holding the atoms together. Not only are measurements of electronic properties necessary to form a complete picture of the material science, electronic properties like superconductivity are of interest in technological applications of novel synthetic materials. Inelastic scattering processes transfer energy between the electron beam and electrons in the sample, but these transfers can only be resolved in spectrometry if the energy spread of the incident beam is narrow. Thus, adding an electron beam monochromator would significantly expand the scientific reach of the diffraction apparatus.

In describing the design, performance, operation and possible upgrades of the Cornell ultrafast electron diffraction apparatus, this thesis makes a strong case for the machine's scientific relevance now and in the future.

CHAPTER 2
A KILOELECTRON-VOLT ULTRAFAST ELECTRON
MICRO-DIFFRACTION APPARATUS USING LOW EMITTANCE
SEMICONDUCTOR PHOTOCATHODES

2.1 Note on authorship

William Li and I contributed equally to writing this Chapter, originally published as reference [1]. To delineate our respective technical contributions, William was responsible for the cathode transfer system, gun and cathode laser illumination, including calibrating the optical parameteric amplifier, as well as electron beam-line simulation, and beam-diagnostic data collection and analysis. I was responsible for the sample chamber, sample transfer, pump optics, electron scattering simulation, and diffraction data collection and analysis. We both contributed to commissioning the rf systems. I took the data and prepared the plots shown in Figs. 2.1(b), 2.3, 2.4(a – c), 2.4(e – f), 2.7, 2.8, 2.9 and 2.10. William and I contributed text to every section of the manuscript, but section 2.7 is almost entirely my own work.

2.2 Abstract

We report the design and performance of a time-resolved electron diffraction apparatus capable of producing intense bunches with simultaneously single digit micron probe size, long coherence length, and 200 fs rms time resolution. We measure the 5d (peak) beam brightness at the sample location in micro-

diffraction mode to be 7×10^{13} A/m²-rad². To generate high brightness electron bunches, the system employs high efficiency, low emittance semiconductor photocathodes driven with a wavelength near the photoemission threshold at a repetition rate up to 250 kHz. We characterize spatial, temporal, and reciprocal space resolution of the apparatus. We perform proof-of-principle measurements of ultrafast heating in single crystal Au samples and compare experimental results with simulations that account for the effects of multiple-scattering.

2.3 Introduction

Probing the transient response of materials after excitation by short, intense pulses of light is a route to the discovery of new phenomena and functionalities not observable in equilibrium [6–10, 13]. Progress in the experimental investigation of out-of-equilibrium states of matter requires the ongoing development of electron and x-ray beam-based tools with high resolving power in space, time, and energy. Observation of the fastest structural responses demands temporal resolution at the picosecond level and below [94, 96].

In practical terms, electron beam systems can be more compact than synchrotron x-ray sources, and can provide complementary structural information [97]. Multiple ultrafast electron probe modalities are common, ranging from diffraction [98] to microscopy (imaging) [99] and spectroscopy [100], accelerated to energies from sub-keV [101] to keV [71], up to few MeV [67, 69, 102–105], with notable advantages in each regime. Among these, keV diffraction beamlines have served as the pioneering ultrafast electron structural probe system [7, 63, 106–108], and keV primary energies offer the advantages of room-scale size,

high scattering cross section (beneficial for the investigation of 2D materials) [109], and intrinsically high reciprocal space and energy resolution [110–113]. In this paper, we focus on the keV ultrafast electron diffraction (UED) system archetype and explore ways to expand its scientific reach.

Temporal resolution has rightly been a focus of much work on ultrafast electron probes, with the state of the art in temporal resolution well below 50 fs [114–116]. In this work, we adopt the rf compression scheme employed by multiple keV sources which regularly achieve 100 fs temporal resolution and below.

In the design of this apparatus, we emphasize the transverse degrees of freedom: probe size and reciprocal space resolution [68, 117]. Decreasing the probe size can significantly reduce the difficulty and time requirements of sample preparation [118], may permit the direct usage of standard transmission electron microscope (TEM) sample preparation techniques [119], or can enable selected area ultrafast diffraction of textured materials [112]. Additionally, for a given pump fluence, reducing the probe size permits a commensurate reduction of pump size and pump-pulse energy. Reducing the total deposited energy in the sample per shot can both extend sample lifetimes and potentially shorten the time required for the sample to relax to its initial state following pump interaction, allowing data to be taken at higher repetition rates.

As a means for beam generation, photoemission affords fine control of the electron distribution both in space and time via laser shaping [120–123]. To increase spatial beam quality, in this work we employ photocathodes with high intrinsic brightness and further tune the photoemission wavelength [124, 125]. The choice of photo-excitation energies, when approaching the photoemission threshold, involves a trade-off between (i) maximizing the ratio of emitted elec-

trons to incident photons — the *quantum efficiency* (QE), and; (ii) minimizing the momentum spread of emitted photoelectrons, summarized in the *mean transverse energy* (MTE) [24] of the beam. The maximum brightness achievable from a photoemission source is inversely proportional to MTE [126, 127].

Almost all ultrafast electron machines rely on metal photocathodes. While being robust, metals typically have much lower quantum efficiency (often $< 10^{-4}$, but there are exceptions [128]) and higher MTE (often 100s of meV) than the best performing semiconductor photocathodes. We elect to use alkali antimonide photocathodes, which possess higher QE ($\sim 10^{-3}$) and lower MTE (< 50 meV) when illuminated with near-threshold visible and near-infrared photons. This high quantum efficiency near the photoemission threshold is critical as it mitigates the brightness diluting effects of multiphoton photoemission and ultrafast cathode heating [129, 130]. However, the cost of this increased brightness is extreme vacuum sensitivity. Unlike metal photocathodes, alkali antimonides must be grown, transported, and used in ultra high vacuum (UHV) conditions.

Multiple ultrafast microscopy sources have utilized sharp tip geometries to generate coherent, sub-micron probes [86, 87, 131]. Similar sub-micron emission sizes in high quantum efficiency semiconductor cathodes are yet to be demonstrated but are possible in principle. Low MTE photoemission is, in a sense, the conjugate technique to spatial confinement, but has the advantage that it does not restrict total emitted charge per pulse. In this work, we use a 10 micron diameter laser-machined aperture just upstream of the sample plane (henceforth referred to as the “probe-defining aperture”) to generate few-micron rms sample probe sizes. In the hypothetical case without space charge, the role of the photocathode MTE is straightforward; our electron optics roughly image the

photocathode plane onto this aperture, and the MTE then primarily determines the reciprocal space resolution of the diffraction pattern. However, we operate in a regime where space-charge is non-negligible, and this modifies the direct correspondence between MTE and reciprocal space resolution. Space charge forces usually degrade the brightness of the total beam, a fact which on the surface suggests that low MTE may not be useful for beam brightness at the sample. However, for both high-charge photoinjectors (for example, for synchrotron light sources) and UED machines of the kind described in this work, it has been shown in simulation that if beam optics and setpoints are designed from the outset to incorporate low MTE photoemission, significant performance gains are possible, down to the levels of the lowest MTEs measured from photoemission to date: ~ 10 meV [132]. We present below simulations of this effect at play in our apparatus, as well as measurements consistent with the simulations.

The effects of space charge are further mitigated by selecting only the spatial core of the beam, as we do via the probe-defining aperture. In the core of the beam, nonlinear space charge forces are much smaller than at the edges, so that the core of the beam remains brighter than the beam as a whole [126, 132, 133]. We typically overfill the probe-defining aperture by orders of magnitude in charge so that we select only this core, whose brightness is most closely determined by the initial MTE and photoemitted charge density. As compared to space charge free operation, this method provides significant flux gains through the aperture with only modest concessions in coherence. For probe diameters of 10 micron, we typically select between 100-1000 electrons from incident pulses of $\sim 10^5$ electrons. The resulting bunch length at the sample is < 200 fs rms.

Operated in micro-diffraction mode at its maximum repetition rate of 250 kHz with between 100 to 1000 electrons per pulse, we measure a peak brightness of $7 \times 10^{13} \text{A/m}^2\text{-rad}^2$ at the sample plane, which is the state of the art in this charge regime. Thanks to its photoinjector heritage, our design mitigates much of the performance-degrading effects of space charge and in high-charge mode, at 10^5 electrons per bunch, achieves a peak brightness of $4 \times 10^{13} \text{A/m}^2\text{-rad}^2$, a small decrease in brightness for a dramatic increase in charge. Wide flexibility in bunch charges is advantageous in UED experiments particularly at moderate pump fluences, even in stroboscopic operation, because sample relaxation times and damage thresholds can prohibit running at megahertz repetition rates [134, 135]. Moreover, the intrinsically lower energy spread of our photocathode makes our machine suitable for performing sub-eV ultrafast electron energy loss spectroscopy experiments in the future. Finally, we compare below our brightness figures with brightness measurements in both MeV and keV ultrafast electron diffraction and microscopy systems, and show that our machine operates in an unfilled, complementary parameter space.

The body of this paper begins in Section 2.4 by describing the subsystems of the beamline, which we have named MEDUSA (Micro-Electron Diffraction for Ultrafast Structural Analysis). In sections 2.5 and 2.6 we report diagnostic measurements of the spatial and temporal resolution of the electron probe. Section 2.7 concludes the paper by presenting the results of a proof-of-principle measurement of ultrafast heating in a gold sample.

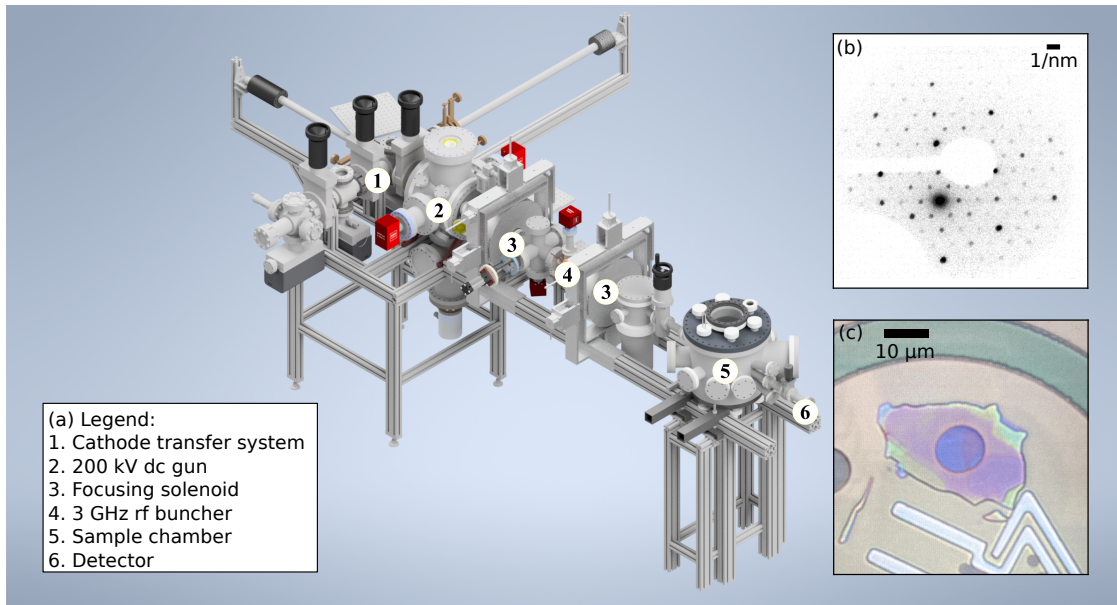


Figure 2.1: (a) Schematic of the UED apparatus. The beamline consists of a 200 kV dc gun, two solenoids, a 3 GHz rf bunching cavity, the sample chamber, and a detector. The total length of the beamline is approximately 2.2 m. (b) Example data taken with the apparatus, showing a selected area electron diffraction pattern produced by a single flake of Nb_3Br_8 [136]. (c) The sample flake viewed under an optical microscope, the dark oval is a $10\ \mu\text{m}$ window through the SiN substrate.

2.4 System Description

Our photoemission source is a Na-K-Sb cathode grown in the Cornell photocathode lab [137] and transported to the electron gun via a UHV suitcase. Na-K-Sb photocathodes have simultaneously high quantum efficiency ($\sim 10^{-3}$) and low MTE ($< 50\ \text{meV}$) when illuminated with red (650 nm) light [138]. Our photocathode geometry is planar, and the photocathode film diameter is $\sim 1\ \text{cm}$. Thus, the profile of the photoemitting laser determines the electron source size. The photocathode is mounted on a custom INFN/DESY/LBNL-style miniplug which allows laser illumination in one of either transmission or reflection mode

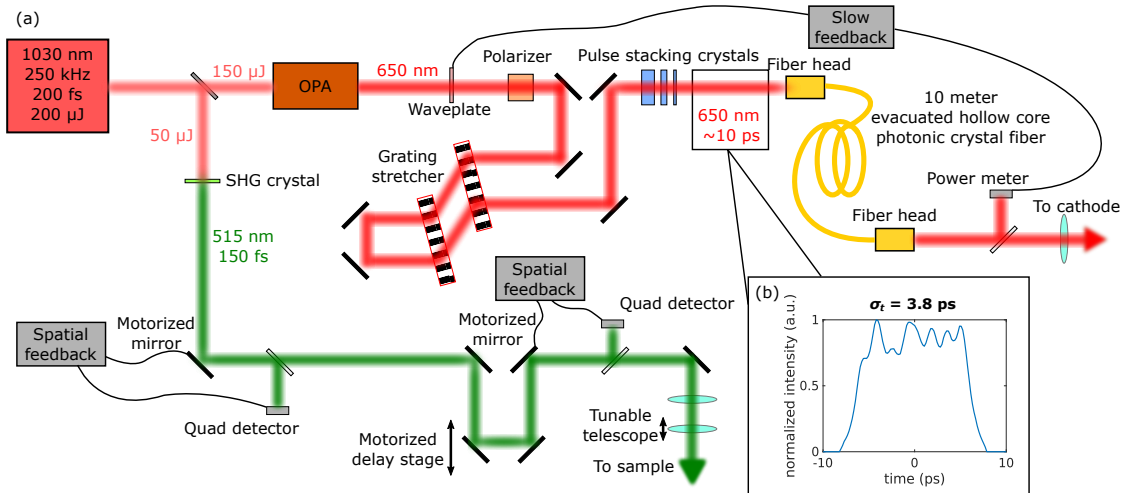


Figure 2.2: (a) A schematic of the laser system for the MEDUSA beamline. A 1030 nm fiber laser is used to generate both the 515 nm pump and the 650 nm photoemitting laser. The photoemitting laser is stretched with pulse stacking crystals and transported through a fiber to the cathode, to ensure position stability. The pump laser utilizes multiple feedbacked mirrors to ensure position stability. A motorized delay stage controls the relative time of arrival of the pump and probe. (b) Temporal distribution of the photoemitting laser as measured by deflecting a zero charge emitted electron beam.

[139, 140]. In reflection mode, we use a laser spot size of $25 \mu\text{m}$ rms, while in transmission mode, a final lens placed close to the cathode forms a minimum laser spot size of $5 \mu\text{m}$ rms. The required pointing stability of the photoemitting laser is much stricter in transmission mode than in reflection mode; the results reported in this paper were obtained in reflection mode. A dc gun accelerates the beam [141] to a maximum 200 keV; our typical operating energy is 140 keV. A schematic of the beamline is shown in Fig. 2.1. Following the dc gun, the beam is focused transversely by two solenoid lenses, and longitudinally by a 3 GHz bunching cavity. We place the transverse and longitudinal foci in the plane of the sample, and the diffraction pattern is transported by a drift to a modular detector section of variable length, depending on the reciprocal space field of

view required.

The laser system for generating both the pump and probe beams is a 250 kHz, 1030 nm, Yb fiber laser (Amplitude Systèmes Tangerine). One quarter of the available 200 μJ pulse energy is taken to generate the pump (typically 515 nm, via second harmonic generation), while the rest drives an optical parametric amplifier (OPA, Amplitude Systèmes Mango) to generate tunable visible light for photocathode illumination. A schematic of the entire setup is shown in Fig. 2.2. The OPA is tuned to generate 300 fs pulses at 650 nm, with 10 μJ pulse energy. A grating pair stretches the 300 fs pulse to approximately 1 ps, and the pulse is further broadened to 10 ps fwhm via temporal stacking crystals [142]. This long pulse length is chosen to obtain a “cigar” electron bunch aspect ratio upon photoemission, which is known to alleviate transverse space charge forces [127, 143]. Furthermore, the optimized simulations, shown in Fig. 2.5 and described in more detail in section 2.5, all required pulses with fwhm > 5 ps. We choose stacking crystals over a single high-dispersion grating stretcher, as large dispersion combined with the inhomogenous spectrum of the OPA would introduce temporal profile distortions.

Multiple feedback mechanisms ensure laser power and pointing stability. The photoemitting laser intensity is set by a waveplate controlled by a slow (~ 5 Hz) feedback mechanism, which primarily corrects for thermal drifts. The photoemitting laser is transported to the cathode via a single mode hollow core fiber, which both ensures position stability and cleans the spatial mode of the OPA. The pump laser position and angle are read by two quadrant detectors, each of which controls a fast piezo-mirror that holds the position of the laser on the sample constant to 1 μm rms. This position stability is of critical importance

given the small size of both pump and probe. The pump laser size can be tuned down to $< 10 \mu\text{m}$ rms at the sample in the current optical configuration.

The bunching cavity is a 3 GHz reentrant TM01 cavity based on the Eindhoven design [144]. The low-level 3 GHz rf signal is derived from the 50 MHz laser oscillator; the beam dynamics are therefore largely insensitive to laser oscillator phase drift. A fast feedback system based on the work of Otto et al.[145] controls both both the phase and the amplitude of the buncher rf field as measured by a field probe on the cavity.

A large volume sample chamber provides flexibility in experimental design. Fig. 2.3(a) is a diagram of the elements of the sample chamber when configured for ultrafast electron diffraction experiments. Pump pulses enter through a chamber window and a final, in-vacuum mirror determines the position of the pump spot on the sample. A 175 mm lens downstream of the final mirror focuses the pump to form a waist at the sample. An out-of-vacuum, remotely adjustable lens doublet enables tuning of the final spot size on the sample. Prior to entering the chamber, a beam splitter sends part of the pump pulse energy to an out-of-vacuum camera —the virtual sample camera— that monitors the position of the pump pulse on the sample: the path-length to the camera is equal to that of the sample from the splitter, and a lens of equal focal length focuses the picked-off pulse to a waist at the camera CCD. Another camera looking into the sample chamber monitors the position of the sample stage, as well as the physical condition of the sample. Fig. 2.3(b) shows an example image of a 3 mm copper TEM grid (used for the destructive plasma timing diagnostic discussed below), with pump laser damage clearly visible.

The flexibility to modify the sample setup entails routine vacuum venting

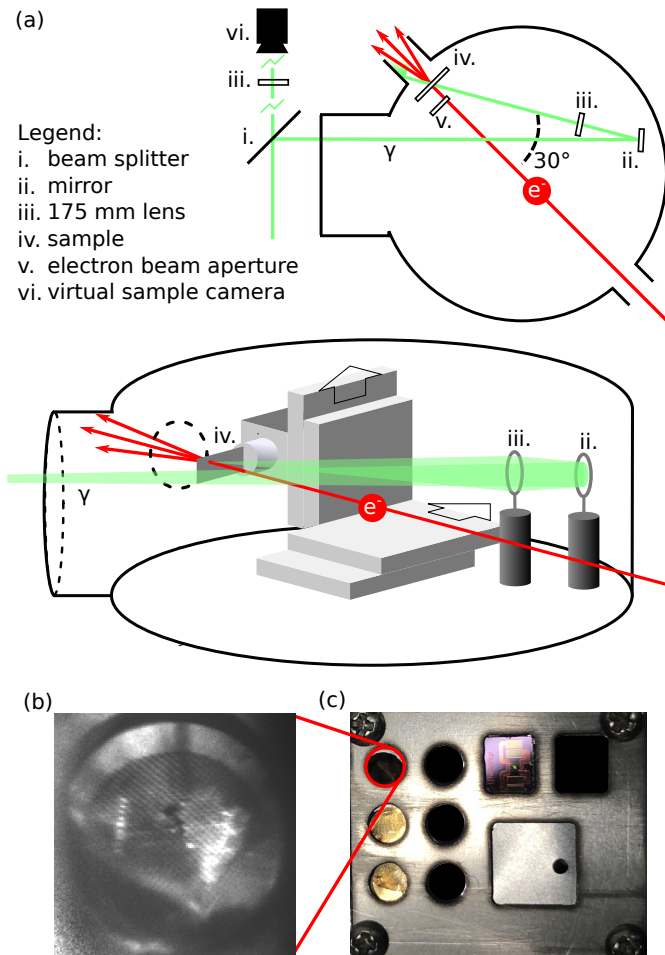


Figure 2.3: (a) Top down illustration of our sample chamber, configured for ultrafast electron diffraction. We split the pump beam at the chamber entrance. The main pump path reflects off a final mirror and passes through a final focusing lens before reaching the sample. An aperture collimates the electron probe. The pump path bypasses the electron aperture and makes a 30° angle with the electron path. The other pump path, split at i., is focused by an equivalent lens onto a camera we use to track the pump position on the sample. (b) A view of a copper TEM mounted in the sample holder inside the chamber from a camera located outside the vacuum. (c) The sample holder accommodates 3 mm TEM grids, among other standard TEM sample mounts, as well as knife edges and pinholes for measuring emittance. The sample can be remotely translated transversely and up to two tilt axes.

of the sample chamber, making a bakeout impractical. Therefore, the vacuum in the sample chamber remains in the mid 10^{-8} Torr level during beam running. To prevent poisoning of the sensitive alkali antimonide photocathode, a vacuum conductance aperture and a large non-evaporable getter pump (~ 1000 l/s pumping speed) separate the beamline into two portions: sample chamber plus detector (10^{-8} Torr) and the ultra-high vacuum portion, consisting of the gun itself ($< 10^{-11}$ Torr) and the beam optics section (10^{-10} Torr). The resulting operational lifetime of our photocathodes is several months.

We place the probe-defining aperture 10 - 15 mm upstream of the sample. This stand-off distance allows the pump beam to reach the sample without clipping on the electron aperture while minimizing the contribution of momentum spread to the probe size on the sample. Pump and probe rays make an angle of 30° at the sample plane. Pulse front tilt does not significantly change the pump pulse length because of the pump's small transverse size: the transverse full width at half max is one third the pulse length.

We have tested two detector modalities. For emittance measurements, or for diffraction measurements where high momentum resolution is required, we use a high spatial resolution $50 \mu\text{m}$ thick Ce:YAG scintillator screen coupled to a cooled, scientific CMOS camera (Teledyne Photometrics Prime BSI-Express) with a lens capable of 1:1 image magnification. For most diffraction experiments, even higher collection efficiency is desired. In this case we use a P11 phosphor with a high numerical aperture lens system on the camera. The detectors are a separate vacuum module from the sample chamber, so they can be exchanged, or the camera length can be modified, without breaking the chamber's vacuum.

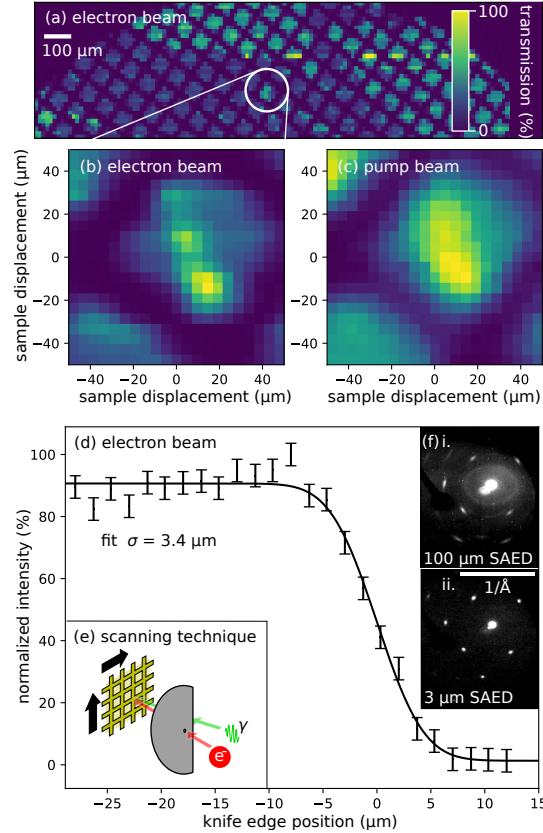


Figure 2.4: (a) Scanning electron transmission image of our ultrafast diffraction sample, a gold film mounted on a 3 mm gold TEM grid. (b) Finer electron beam scan of a unique feature in the sample film. (c) Transmission scan of the same feature with the pump laser beam, for the purpose of verifying alignment of electron beam and pump. (d) Beam size measured at the sample plane through the final collimating aperture. There is a silicon knife edge in the sample plane, and the beam size is measured by fitting an error function to the intensity as a function of the position of the knife edge. The beam size is measured to be 3 microns rms. (e) Illustrating the two transmission modes, in red the electron beam is collimated by a 10 μm diameter aperture, in green the pump beam is steered around the electron aperture, making an angle with the electron beam of 30° at the sample plane; we perform the scan by moving the sample, shown in gold. (f) Selected area electron diffraction of the same gold sample comparing i. a 100 μm rms probe size against ii. a 3 μm rms probe size.

Beam energy	140 keV
Cathode spot size	25 μm rms
Charge on target	Up to 0.1 fC
Probe size on target	3.5 μm rms
Normalized emittance	≤ 1 nm-rad
Bunch length	< 200 fs rms
Pump fluence	Up to 1 J/cm ²
Pump size on target	Down to 10 μm rms

Table 2.1: Routine beamline parameters for ultrafast micro-diffraction experiments.

2.5 Spatial Resolution

Spatial resolution in this beamline can be characterized by both the reciprocal space resolution and the beam size in real space. High reciprocal space resolution results in sharp diffraction peaks, while a small beam size enables the beam to probe small spatial features in the sample.

Reciprocal space resolution Δs can be expressed in terms of the rms spot size on the sample σ_x and normalized emittance ϵ_n as [67]:

$$\Delta s = \frac{2\pi}{\lambda_e} \frac{\epsilon_n}{\sigma_x}, \quad (2.1)$$

where λ_e is the electron de Broglie wavelength.

As shown in Eq. 2.1, there is a tradeoff between reciprocal space resolution and beam size. The beam size is primarily determined by the size of the probe-defining aperture and the size of the target sample, so the reciprocal space resolution in this system can only be improved by lowering the transverse emittance. Thus, it is critical to measure the emittance to quantify the performance of this apparatus, in both the high-charge and micro-diffraction modes of operation.

In the high-charge mode, the probe-defining aperture is removed, and the typical charge is up to 10^5 electrons/bunch, or 16 fC, at the sample plane. This is also the charge per bunch typically delivered to the aperture in micro-diffraction experiments. We measure the emittance of this bunch by first bringing it to a waist at the sample. Next, scanning the 10 micron diameter aperture across the beam both horizontally and vertically, and imaging the transmitted beam distribution on a viewscreen (which in this case represents the sample momentum distribution), we generate a full 4d transverse phase space of the beam. We then directly compute the emittance by calculating the sigma matrix of the beam. With this method, we measure a projected, normalized emittance of 13 nm-rad at 16 fC with an rms beam size of $43 \mu\text{m}$. Achieving this value required not only the correction of normal quadrupole and skew-quadrupole, but also sextupole components in the transverse and longitudinal focusing optics with dedicated quadrupole and sextupole corrector magnets just downstream of the second solenoid. This correction procedure will be described in a forthcoming manuscript, along with the complex space charge dynamics and compensation involved.

The micro-diffraction mode, the routine configuration for diffraction from small crystal flakes, e.g. panel (c) of Fig. 2.1, uses the probe-defining aperture to generate very small probes. Typical beamline operational parameters in this mode are listed in Table 2.1. The right side of Fig. 2.4 shows a knife edge scan performed at the sample plane, yielding a transverse rms probe size of 3 microns. The bunch charge through the aperture is 500 electrons, and the normalized emittance is 0.7 ± 0.1 nm-rad. The emittance in this case was measured by bringing the beam to a focus on the pinhole, measuring its size at the sample with the knife edge and measuring the momentum spread using the beam size

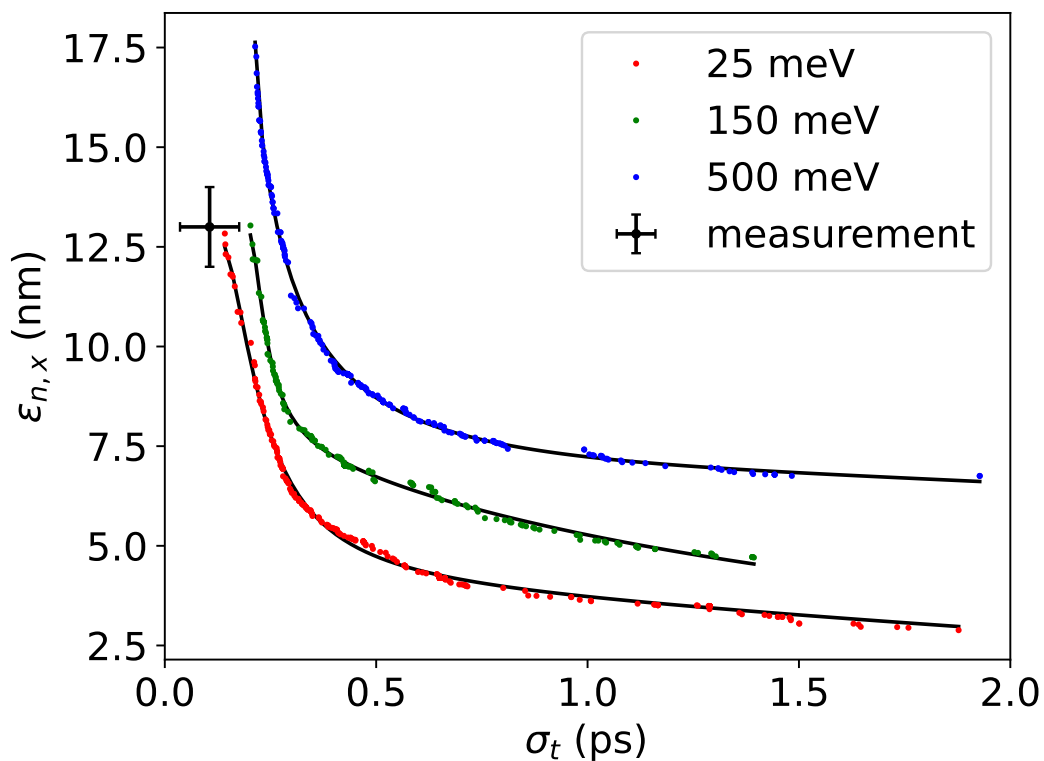


Figure 2.5: Pareto fronts generated in simulation by a genetic algorithm optimizer for cathode MTEs of 25 meV (red), 150 meV (green), and 500 meV (blue) with a final bunch charge of 16 fC. The optimizer was set to minimize emittance and bunch length, holding MTE, gun voltage, and element positions constant while being free to pick operational parameters. The measured emittance and bunch length are consistent with an MTE less than 150 meV. The solid lines are included solely for the purpose of guiding the eye.

on the final screen.

In order to understand the role of low MTE in our space charge dominated conditions, we use General Particle Tracer (GPT) [146], a particle tracking PIC code, to simulate the changes in beam dynamics for various MTEs. GPT is coupled with a multiobjective genetic algorithm [147], which is set to optimize both

bunch length and emittance at the sample plane, generating a curve of optimal emittance for each bunch length, known as a Pareto front. We fix the gun voltage and element positions and allow the electron optics and 3d laser pulse shape to vary, as would be the case in operation. Pareto fronts generated for MTEs of 25, 150, and 500 meV are shown in Fig. 2.5, and in these optimizations, the optimizer was permitted to emit up to 160 fC at the cathode and is required to transmit 16 fC to the sample after traversing physical apertures (for example, the bore of the buncher and pipe) in the beamline. We see a reduction in emittance of roughly 30% from 150 meV to 25 meV and roughly a factor of 2 from 500 meV to 25 meV, averaged over all displayed bunch lengths.

From a physical standpoint, the relationship between MTE, brightness, and bunch length can be understood by considering the emitted charge. To achieve the same final emittance and charge at higher MTE, simulations show that it is necessary to emit a higher charge density and select out a smaller fraction of the total beam. Higher charge density results in larger longitudinal space charge forces prior to the sample plane, leading to longer bunch lengths.

Comparing the measured emittances to simulation, the optimal simulated emittance for a 200 fs bunch length is 17.5 nm-rad at an MTE of 500 meV, 13 nm-rad at 150 meV, and 10 nm-rad at an MTE of 25 meV. As will be covered in section 2.6, the bunch lengths we measure are lower than 200 fs, so the measured high-charge emittances are consistent with an MTE substantially less than 150 meV.

To help locate our machine in the parameter space of other ultrafast electron instruments, we compute 4d and 5d beam brightnesses from our beam diagnostic measurements. It is convenient to define the 5d normalized beam brightness

B_{np} in terms of normalized emittance and peak current I_p as

$$B_{np} := \frac{I_p}{\pi^2 \epsilon_n^2}. \quad (2.2)$$

We define the peak current of a beam with charge per bunch Q and rms bunch length σ_t as

$$I_p := \frac{Q}{\sqrt{2\pi}\sigma_t}. \quad (2.3)$$

In the high-charge mode, the 5d brightness at the sample plane is $4 \times 10^{13} \text{A/m}^2\text{-rad}^2$, and $7 \times 10^{13} \text{A/m}^2\text{-rad}^2$ in the micro-diffraction mode, consistent with the expectation that core brightness is higher than average brightness. For machines operating in the same charge and emittance regime, the natural units of 4d brightness, Q/ϵ_n^2 , are electrons per nanometer-radian squared per pulse. Our machine delivers 600 electrons/(nm-rad)² in high-charge mode and 1000 electrons/(nm-rad)² in micro-diffraction mode at the sample plane. For experimental applications, brightness at the sample plane is the relevant figure, not source brightness, as space charge forces and lens aberrations cause brightness loss in beam transport [135, 148, 149].

It is informative to compare the brightness of MEDUSA with MeV-UED beamlines and ultrafast electron microscopes (UEMs) equipped with nano-tip sources, as this subset of ultrafast electron technology spans multiple orders of magnitude in charge per bunch, repetition rate, emittance, and temporal resolution around our operating point. Additionally, the brightness values of these machines have been well-characterized. Megavolt diffraction beamlines have demonstrated 5d brightnesses in the range of 10^{12} to $10^{14} \text{A/m}^2\text{-rad}^2$ and 4d brightnesses in the range of 10 to 10^3 electrons/(nm-rad)² in both high-charge and micro-diffraction modes [67–70]. On the other end of the charge spectrum, at less than one electron per pulse delivered to the sample, nanotip UEMs

achieve 5d brightnesses in the range of 10^{13} to 10^{15} A/m²-rad² and 4d brightnesses in the range of 10^3 to 10^4 electrons/(nm-rad)² when operated in high coherence mode [131, 150]. Nanotips have been shown to yield 10^{12} A/m²-rad² and 10^2 electrons/(nm-rad)² at charges greater than one electron per pulse delivered to the sample; however, owing to brightness loss, users do not typically operate nanotip UEMs at these charges [150].

This beamline occupies an unfilled position in parameter space, and is complementary to other state-of-the-art time-resolved electron scattering devices. Looking to the examples cited above, this beamline achieves comparable transverse brightness to existing MeV diffraction beamlines, but with high repetition rate and reciprocal space resolution in a compact footprint. However, compared to the same MeV devices, this beamline has coarser temporal resolution and more stringent vacuum requirements, and more complicated space charge compensation. Compared to nanotip UEMs, this beamline offers finer temporal resolution and much larger charge per pulse at the cost of lower transverse brightness.

As stated in the introduction, real space resolution, i.e., probe size, is a critical figure of merit for this beamline. In addition to the aforementioned knife edge scans, the left side of Fig. 4 provides another demonstration of the real space resolution of the electron beam. By scanning the position of the sample, we make a transmission image of the sample. Our target is a gold TEM grid with bar width of 25 microns and a pitch of 83 microns. We resolve fine details of this target using the electron beam scan with better resolution than the equivalent scan with the pump laser, which was measured to have a size of 10 microns rms. Not only does this method provide micron-resolution imaging, it also allows us

to align pump and probe with single micron precision.

2.6 Temporal Resolution

Two terms add in quadrature to determine the temporal resolution of the instrument: (i) the stability of the gun and bunching fields, and (ii) the bunch length of the probe beam. A compact 3 GHz TM110 deflecting cavity (DrX Works) placed very near the plane of the sample transversely streaks the electron beam and provides direct measurements of both (i) and (ii).

The change in beam centroid as the deflector kicks the beam gives the bunch time of arrival. After subtracting off the transverse jitter in quadrature, we measure the time of arrival jitter to be 170 fs. We believe this to be an upper bound, as it includes contributions from deflector phase jitter. We estimate bunch length by deconvolving the beam width with the deflector on from the beam width with the deflector off. By fitting for the kernel of the convolution, we extract the contribution to the beam width from the deflected bunch length. Fig. 2.6 shows measured bunch length as a function of buncher field amplitude. The minimum bunch length is measured to be 110 ± 70 fs rms, with the majority of the uncertainty arising from the deconvolution of the transverse beam size from the deflected bunch length, as well as deflector phase jitter. We plan to improve our measurements of time of arrival jitter by performing streaked diffraction experiments [151, 152] which will provide a time-stamped signal to reconstruct beam time of arrival, mitigating the effects of deflector phase jitter. To generate an estimate of the overall temporal resolution, we add the measured time of arrival jitter in quadrature with the bunch length to yield 200 ± 40 fs rms.

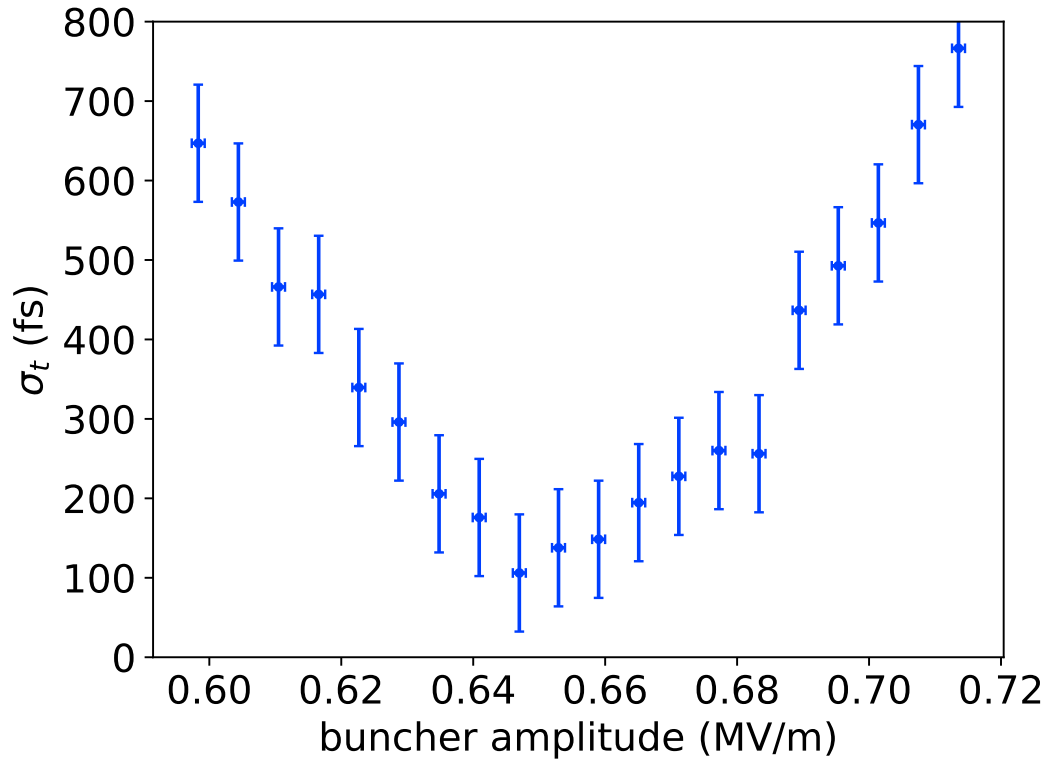


Figure 2.6: RMS bunch length as a function of buncher field amplitude. The minimum bunch length measured is less than 200 fs. The displayed error bars represent the mean of the individual standard errors for each measurement.

A variable path length controls the time of arrival of the pump pulse at the sample plane. Synchronizing the pump and probe beams requires a target sample that responds promptly to the pump pulse. A standard technique is to aim the pump at a copper TEM grid and photoemit an electron gas [153], recording a time-resolved shadowgram of the electron gas with the probe beam. At a pump wavelength of 515 nm, the emitted charge is quadratic in pump energy and the effect on the probe becomes obvious at fluences above 100 mJ/cm². Fig. 2.7(a) shows the signal we measure upon scanning pump delay. Fig. 2.7(b) sketches the physical mechanism: the ejected plasma's coulomb field deflects the probe

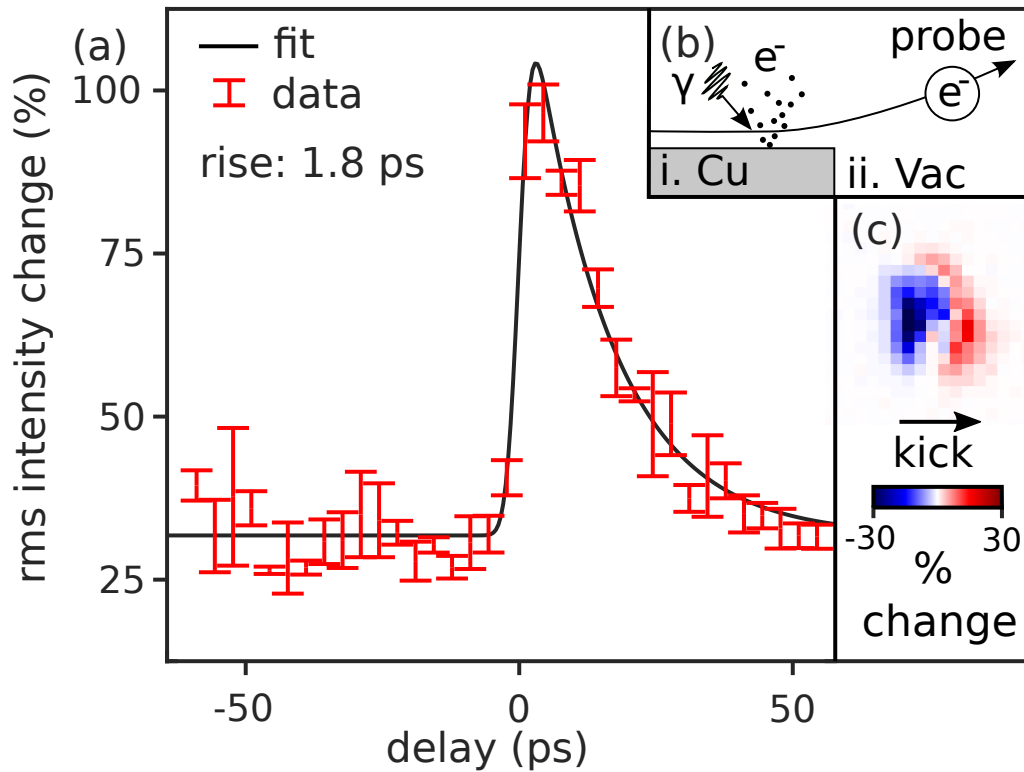


Figure 2.7: (a) Measurement of time-dependent photoemitted plasma lensing, showing the rms per pixel change in beam intensity as a function of time. (b) Schematic of the mechanism that drives the beam response, i. pump laser photoemits an electron gas from a copper grid, ii. Coulomb field from emitted gas deflects the electron beam. (c) Example of the detected difference image used to compute the signal plotted in (a).

beam. The size of the deflection (exaggerated in Fig. 2.7(b)), though small compared to the beam size, is readily apparent in a difference image comparing the probe beam on the final screen between pump on and off. Fig. 2.7(c) shows an example difference image. The signal we compute is the rms intensity of these difference images, cropped to a region of interest, as a function of delay time.

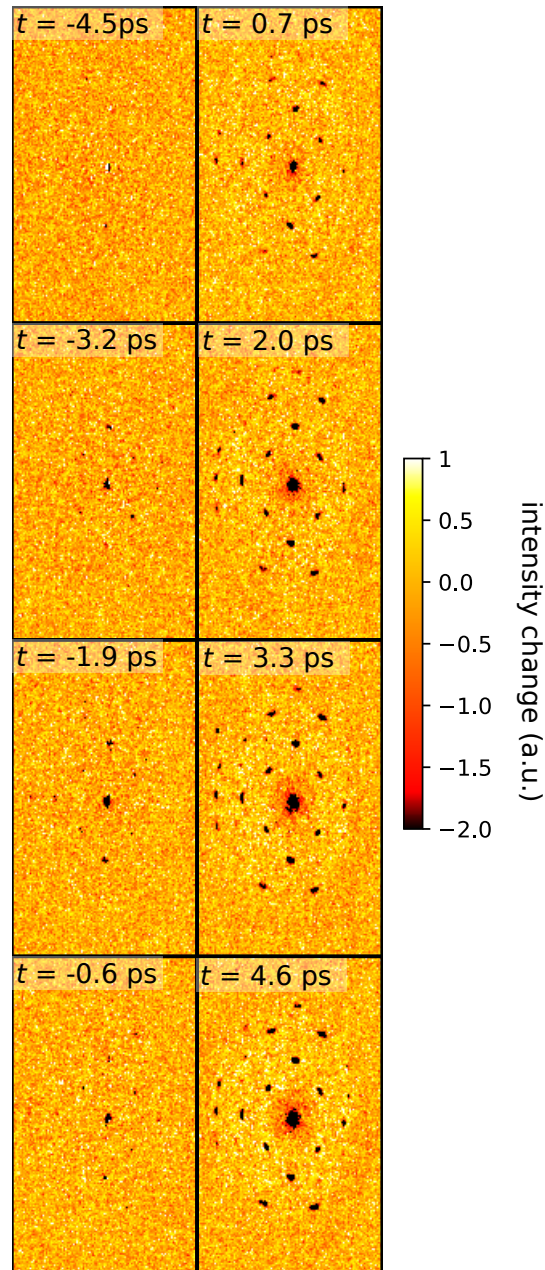


Figure 2.8: Time-dependent diffraction from a gold sample pumped by 515 nm light. Each panel is a composite of 100 acquisitions at a 5 s exposure time and 5 kHz electron beam repetition rate, taken at a fixed pump delay indicated by the inset text.

2.7 Ultrafast Electron Diffraction

As a proof-of-principle experiment, we measure the ultrafast heating of a gold diffraction sample (TED Pella #646) with mosaicity observed in static diffraction patterns indicating domains of sizes $\sim 10 - 100 \mu\text{m}$. According to a two-temperature model of this process, the 515 nm pump beam deposits its energy into conduction electrons, which as a subsystem thermalize on a time scale much shorter than the 200 fs pump pulse length. The hot electron gas then equilibrates with the lattice over a few picosecond relaxation time τ . The transverse profile of the deposited energy is Gaussian with an rms size of $12 \mu\text{m}$. This pump size represents a trade-off between uniform illumination and minimizing the total deposited energy. The probe optics are chosen to maximize transmission through the collimating aperture, producing an rms probe size of $5 \mu\text{m}$. Hence, the sample temperature in the probed region is close to spatially uniform. Measuring the incident, transmitted, and reflected pump power *in situ*, we estimate the absorbed pump fluence to be no greater than $0.8 \text{ mJ}/\text{cm}^2$.

In the data-set shown in Fig. 2.8, we scan delays at 1.3 ps intervals. Each panel in the figure shows the difference in intensity between pump on and pump off on the detector screen, averaging 1.25×10^6 pulses per delay stage position. We alternate acquisitions of 5 s at a repetition rate of 5 kHz between pump-on and pump-off to control for slow drifts in the primary beam current.

Grouping peaks related by lattice symmetries and averaging the change in peak intensity at each delay time gives the results shown in Fig. 2.9(a). To each data set we fit an exponential decay, constraining the fit to find a common decay time τ for all curves and obtaining $\tau = 3.0 \pm 0.3 \text{ ps}$.

Averaging the diffraction data along the azimuth provides a complementary 2D visualization of the ultrafast time-dependent effect. Fig. 2.10(a) shows delay time on the vertical axis and the magnitude of the scattering vector on the horizontal. The four dark streaks that begin to appear at $t = 0$ correspond to the primary beam and the three reflections plotted in Fig. 2.9. The dashed and solid horizontal lines correspond to the cross-sections plotted in Fig. 2.10(b). In addition to the suppression of the diffraction peaks, Figs. 2.10(a) and (b) reveal an enhancement of the diffuse scattering signal at scattering vectors in the interval between 2 and 6 rad/. With an upgrade to our detector we plan to better resolve the momentum dependence of time-dependent diffuse scattering, revealing the non-equilibrium dynamics of lattice phonons [134, 154].

The leading effect of ultrafast heating on the probe beam in the weak scattering limit is to wash out the coherence of the partial waves scattered from individual atoms. If the sample's initial temperature is well above its Debye temperature, and the temperature change ΔT is small compared to the sample's melting point, then the fractional suppression of the beamlet scattered by reciprocal lattice vector \mathbf{k} is proportional to $k^2\Delta T$. Though the gold film is approximately 20 nm thick, at our primary beam energy, multiple scattering is significant and hence the trend in Fig. 2.9(a) does not show a quadratic dependence on scattering angle.

To quantify the importance of multiple scattering, we perform electron diffraction simulations with the slice-method code, μ STEM [155]. Simulation results as a function of thickness and temperature are shown in Fig. 2.9(b). The vertical axis represents the relative change in diffraction peak intensity between the two temperatures 273 and 423 K, and the horizontal axis is the simulated

crystal thickness. The vertical dashed line in Fig. 2.9(b) indicates a simulation thickness that reproduces the ordering of Bragg peaks seen in Fig. 2.9(a). The

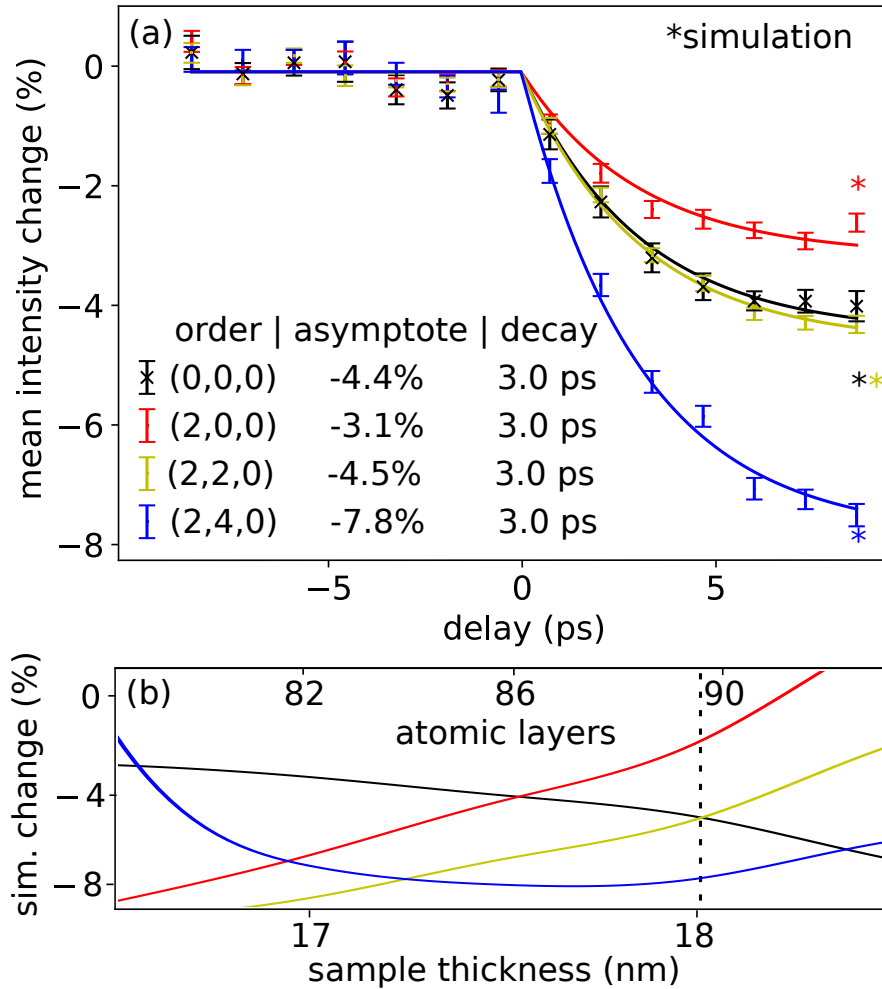


Figure 2.9: Bragg peak intensity as a function of pump delay. Peak intensities are estimated from the data shown in Fig. 2.8 by taking the maxima of Gaussian filtered images. The quantity plotted is the change in this intensity normalized by its fully-relaxed (pump-probe delay 100 microseconds) value. (b) Simulated signal as a function of sample thickness including multiple scattering effects, assuming a cold temperature of 273 K and a hot temperature of 423 K; colors have the same meaning as in panel (a), dashed line indicates a thickness that reproduces qualitatively the dependence on scattering angle in the experimental data, values along this line are plotted as asterisks in panel (a).

range of the horizontal axis in Fig. 2.9(b) covers 12 atomic layers. The figure thus shows that the addition of one atomic layer modulates the temperature response by more than the experimental uncertainty of the data shown in Fig. 2.9(a). The simulations agree qualitatively with our UED data, disagreeing on the scale of 10% of the measured effect. Non-uniform specimen thickness and temperature within the probed region could plausibly account for this discrepancy.

2.8 Summary and Outlook

We have designed and commissioned an ultrafast electron micro-diffraction apparatus with sub-picosecond temporal resolution. Using an alkali antimonide photocathode, we generate beams with low intrinsic emittance allowing for micron scale probe size without significant loss in reciprocal space resolution. A 3 GHz rf bunching cavity compresses the beam longitudinally to a few hundred femtoseconds, while solenoids and a collimating aperture reduce the beam size to $3\ \mu\text{m}$ rms. With this small probe, as a proof-of-principle experiment we showed that the apparatus can clearly resolve the ultrafast evolution of the lattice temperature of a few-micron selected area of a textured gold film.

The capability to perform ultrafast electron diffraction with single-micron scale selected areas enables the study of samples that are challenging (or impossible) to produce in larger sizes. Further, small electron probe sizes allow the commensurate reduction of pump area, which, for a constant excitation fluence, can dramatically reduce the pump energy deposition in the sample, mitigating average heating effects and sample damage at high repetition rates.

Future planned upgrades include the installation of a direct electron detec-

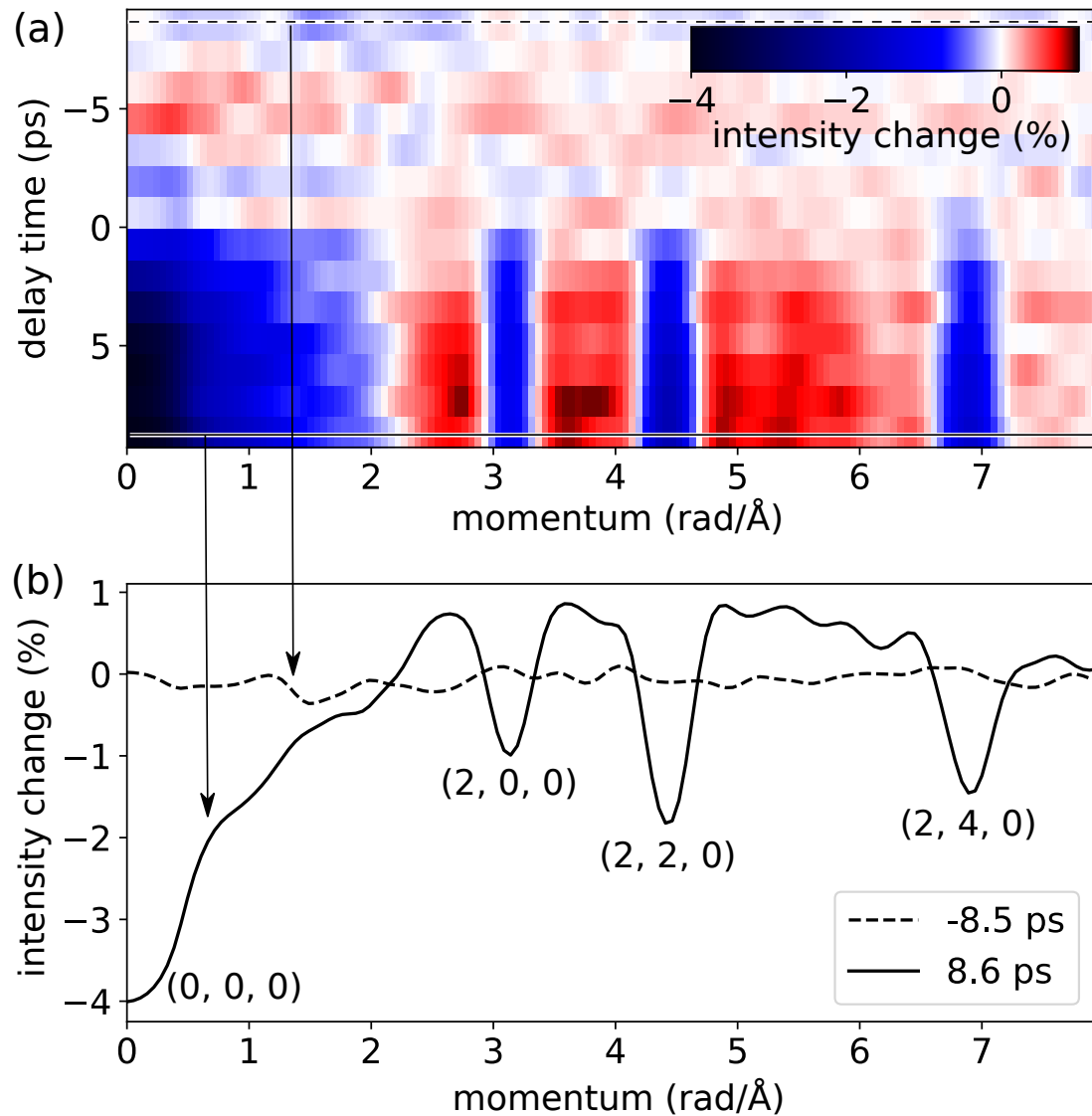


Figure 2.10: (a) Scattering intensity as a function of the magnitude of the scattering vector and pump delay time; the data are calculated by averaging the images in Fig. 2.8 over the azimuthal coordinate, centered on the primary peak. (b) A comparison of two cross sections of panel (a), showing explicitly the percentage change in scattering intensity as a function of the magnitude of the scattering vector; the dashed curve corresponds to the cross section indicated by a dashed line in panel (a), likewise the solid curve.

tor [156], with an expected substantial improvement in both sensitivity and data acquisition rate. Further, low MTE photoemission conditions provide electron beams with low total energy spread (potentially in the 10s of meV). With the addition of a high-resolution spectrometer, this apparatus will have the capability to probe electronic degrees of freedom on ultrafast timescales with very high energy resolution. A single probe that can correlate structural and electronic information promises to provide new insight into the role of electronic-phonon interactions in determining material properties.

ACKNOWLEDGEMENTS

We thank Y. T. Shao and D. A. Muller for suggesting a multiple scattering interpretation of the UED data, and for introducing the authors to the μ STEM software package. This work was supported by the U.S Department of Energy, grant DE-SC0020144 and U.S. National Science Foundation Grant PHY-1549132, the Center for Bright Beams.

CHAPTER 3

OUTRUNNING NOISE IN ULTRAFAST STRUCTURAL DYNAMICS MEASUREMENTS WITH HIGH REPETITION RATE, HIGH DYNAMIC RANGE DIRECT DETECTION

This chapter is a manuscript I am preparing for journal submission as first author.

3.1 Abstract

Optical pump – structural probe measurements, including ultrafast electron and x-ray scattering, provide direct experimental access to the fundamental timescales of atomic motion, and are thus foundational techniques for studying matter out of equilibrium. High-performance detectors are needed in scattering experiments to obtain maximum scientific value from every probe particle. We present the first ultrafast electron diffraction experiments to deploy a hybrid pixel array detector with single-particle sensitivity, 10^6 dynamic range and 1 kHz frame rate. Measurements on a $WSe_2/MoSe_2$ 2D heterobilayer resolve the weak features of diffuse scattering and Moire super-lattice structure without saturating the zero order peak. Utilizing the detector's high frame rate, we show that a lock-in technique eliminates machine drift to provide diffraction difference images at the shot noise limit. Finally, we demonstrate that a fast detector frame rate coupled with a high repetition rate probe can provide continuous time resolution from femtoseconds to seconds, enabling us to perform a scanning-UED experiment that maps thermal transport in $WSe_2/MoSe_2$ and resolves distinct diffusion scales in space and time.

3.2 Introduction

Ultrafast x-ray and electron scattering experiments are essential tools in the materials-by-design thrust of modern materials science and engineering [6–10, 13]. In particular, breakthroughs in the study of atomically thin 2D materials, including twisted bilayers and monolayer heterostructures [157–163], demand advances in instrument sensitivity in space and time, both real and reciprocal. A challenge when characterising 2D materials from information-rich diffraction measurements is that diffraction features are separated by many orders of magnitude in intensity, descending from the (0,0,0) peak, to Bragg scattering, to weaker satellite peaks caused by periodic lattice distortions (PLD), to yet weaker thermal diffuse scattering (TDS). In pump-probe ultrafast electron diffraction, the separation of scales becomes more extreme, and important details of electron-phonon coupling can be hidden in parts per thousand modulation of scattering signals that in static diffraction are already at the 10^{-4} level of total beam current. Moire materials exemplify this challenge, as these samples could plausibly present correlated signatures of inter-layer interactions in Bragg, PLD and TDS scattering. Single electron sensitive CCDs have poor dynamic range, no more than a single decade, making it impossible to investigate correlated but intensity-scale-separated features in the same data set. Integrating direct electron detectors with several decades of dynamic range and kHz frame rates are now coming on-line at (inter)national x-ray user facilities [164–166]. Pulsed probes can cause multiple particles to be incident on a single pixel over the sub-picosecond pulse length, and integrating detectors are able to accurately count the number of particles involved in these multi-particle events. Here we deploy a leading example of this path-breaking detector technology

in a university-scale ultrafast electron diffraction (UED) laboratory to study the multiscale out-of-equilibrium dynamics of a $\text{WSe}_2/\text{MoSe}_2$ bilayer [1, 156, 167, 168].

The aim of this work is both to characterise the performance of our instrumentation and to demonstrate the novel pump-probe methodology this instrumentation makes possible. In addition to the increase in dynamic range, we emphasize two key advances enabled by our detector's kHz frame rate: the reduction in measurement uncertainty via a fast lock-in technique, and the use of fast pulse picking to extend the temporal range of the instrument continuously from femtoseconds to seconds. We demonstrate these novel capabilities in an experiment that maps the diffusion of heat in our sample, from initial femtosecond, ultrafast excitation, out to millisecond thermal relaxation. We resolve the sample temperature in both space and time by scanning a micron sized UED probe and measuring the Debye-Waller effect.

3.3 Methods

Our beamline is shown in Fig. 3.1 and described in detail elsewhere [1]. The probe electron beam is photoemitted with 650 nm laser pulses and accelerated to a primary energy of 140 keV. The Electron Microscope Pixel Array Detector (EMPAD) consists of a grid of 128 x 128 pixels each $150\ \mu\text{m} \times 150\ \mu\text{m}$ in size. Each pixel has a $500\ \mu\text{m}$ thick reverse-biased silicon diode bump bonded to its own read-out electronic circuit. The RMS read noise (where the average is taken over all pixels) is 2.8 ADU, equivalent to 0.011 electrons at 140 keV.

A schematic of our timing system is shown in Fig. 3.2. The base laser repe-

tition rate used in the experiments reported here is 125 kHz, allowing detector exposures as short as a single pulse to be reliably delayed to single pulse precision and repeated at the 1 kHz detector frame rate. An acousto-optic modulator (AOM) controls the duration of pump-pulse trains. The duty cycle of the AOM is also variable to single-pulse precision: we typically choose a duty-cycle to match the detector exposure, eliminating un-detected pulses and thus reducing the thermal load on the sample. We verify the reliability of the timing system by measuring the total pump-energy per exposure with the detector, and we see a sharp quantization of energy as a function of exposure length at intervals of the $8 \mu\text{s}$ laser repetition period.

Our scanning ultrafast electron diffraction technique is illustrated in Fig. 3.3(a), with the sample and sample environment shown in Fig. 3.3(b). The spot size of the electron probe on the sample is defined by a laser-milled aperture 15 mm upstream. An in-vacuum lens focuses the 515 nm pump pulse to a 10 μm spot on the sample, and the pump spot is steered on the sample by an out-of-vacuum mirror. A virtual-sample camera placed out of vacuum monitors the location of central peak of the pump laser to micron precision.

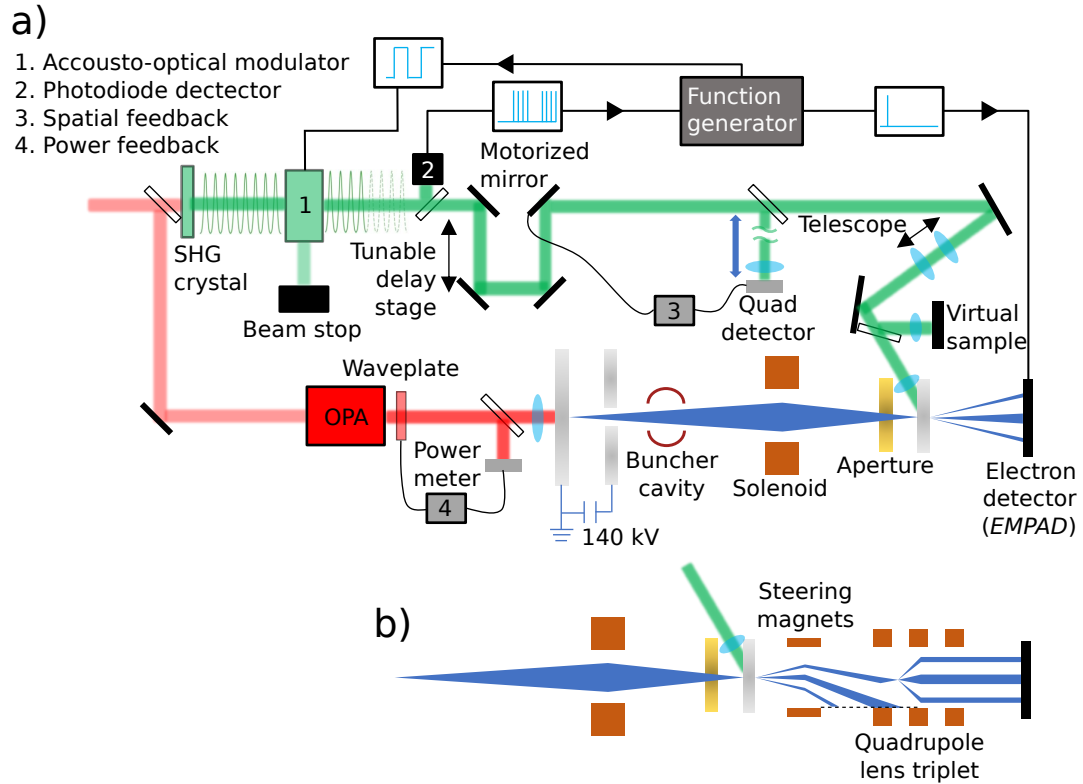


Figure 3.1: (a) Schematic of the UED beamline, see reference [1] for details: a 1030 nm Yb-fiber laser drives an optical parametric amplifier that sends 650 nm light pulses to the photocathode; photoemitted bunches are accelerated to 140 keV, compressed by an rf cavity, collimated by a probe-defining aperture, and are collected by the detector after scattering on the sample; the same 1030 nm pulses are split and frequency doubled to synchronously pump the sample. (b) Modification of the detector section of the beamline to accommodate a magnetic quadruple electron lens triplet. The lens triplet enables angular magnification of the scattering pattern. A diffraction feature is selected for magnification on the detector with a steering magnet upstream of the lens triplet.

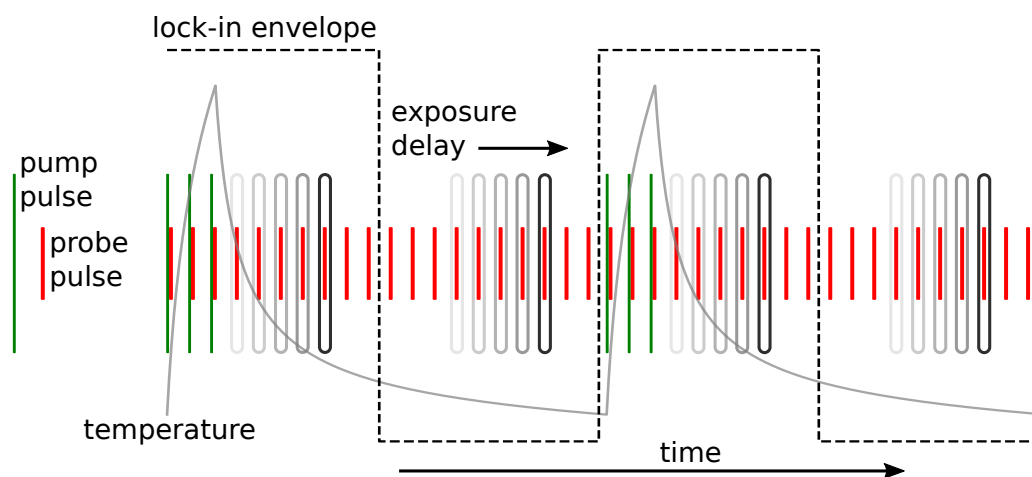


Figure 3.2: Schematic of the pump-probe technique in time; the period between pulses is $8 \mu\text{s}$ and exaggerated here for clarity; the duration of the pump-pulse train is controlled by an acousto-optic modulator; an optical delay stage controls pump-probe delays from 100 fs to 1 ns and detector exposure timing controls pump-probe delays $> 1 \mu\text{s}$. The dashed waveform shows whether exposures are added or subtracted in integrating the pump-probe signal. The solid waveform represents the microsecond-scale temperature envelope predicted by Eq. (3.2).

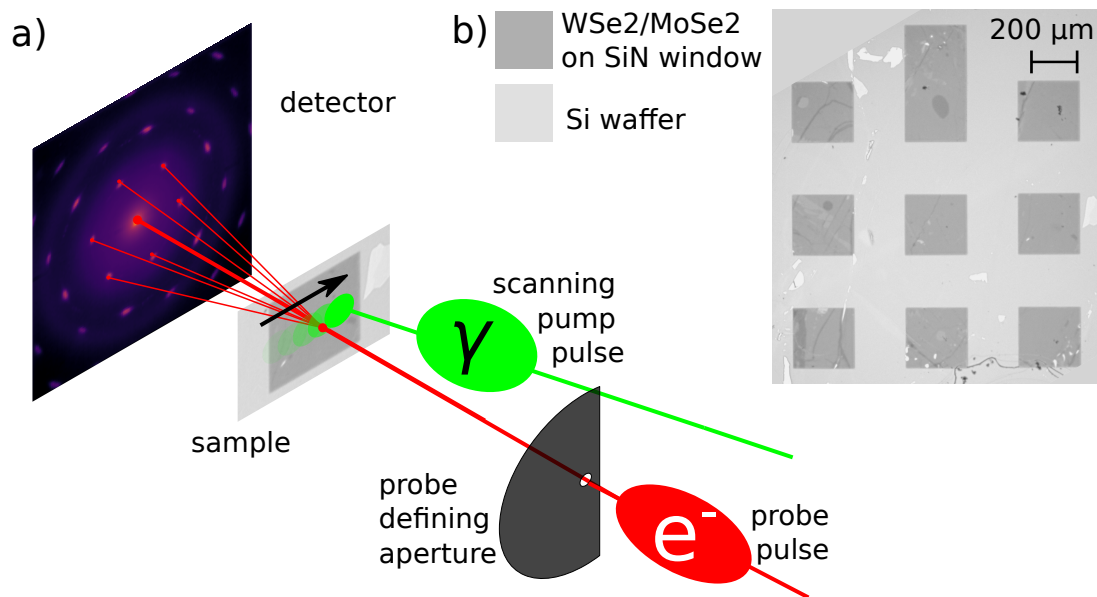


Figure 3.3: (a) Schematic of the spatial scanning technique used to collect the data plotted in Fig. 3.5: a 10 μm aperture defines the size and position of the probe in the sample plane; pump pulses are scanned horizontally across the sample. (b) Optical microscope image of the sample, contrasting 10 nm thin windows hosting the heterobilayer on SiN substrate with Si holder-heat sink.

Figure 3.4(a) shows a static diffraction pattern obtained from the $\text{WSe}_2/\text{MoSe}_2$ sample at short camera length. The logarithmic scale color bar includes over four orders of magnitude of contrast from the (0,0,0) peak to thermal diffuse scattering. The inset to Fig. 3.4(a) shows a long-camera-length diffraction difference pattern isolating a single Moire pair of Bragg peaks (aligned vertically in the image) with two additional satellite peaks visible (aligned horizontally). The difference image is formed by subtracting pumped exposures from unpumped exposures at a delay of 20 ps. We control the detector camera length with a magnetic quadrupole lens triplet downstream of the sample, illustrated in Fig. 3.1.

3.4 Lock-in

We benchmark our experimental uncertainty with pump-probe time-series data, summarized in Fig. 3.4(a)-(c). A standard estimation technique when detector noise and other backgrounds are a source of uncertainty is to fit a peaked function, e.g. a Lorentzian on a pedestal, to pixel counts. A disadvantage of this approach for the purpose of benchmarking is that the non-linear fit function complicates the comparison of the Poisson limit with the experimental uncertainty actually achieved. Instead, we simply make an 8×8 pixel bin centered on the diffraction pair highlighted in Fig. 3.4(a), subtending a solid angle of 10^{-5} Sr at the sample, and count the rate at which electrons arrive anywhere in this momentum-bin.

To analyze the dependence of experimental uncertainty on chopping rate, we divide time series data into n integration time-bins of duration W equal to

the chopping period. We split each time-bin in half, the first half *hot* exposures, when the pump and probe pulses are coincident on the sample, the second half *cold* exposures, when only the probe is incident. The number of hot (N_{hot}) and cold (N_{cold}) electrons counted in a given time-bin is a random variable whose moments we can estimate by taking averages with the respect to our ensemble of n time-bins. In particular, we compute a variance-to-mean ratio (VMR) over W :

$$\text{VMR}(W) := \frac{\text{Var}_W (N_{\text{hot}} - N_{\text{cold}})}{\text{E}_W [N_{\text{hot}} + N_{\text{cold}}]}. \quad (3.1)$$

The VMR defined in Eq. (3.1) can be interpreted as the square of the experimental uncertainty in estimating the effect of pumping the sample, normalized by the shot-noise limit. If $N_{\text{hot}}, N_{\text{cold}}$ are drawn from independent Poisson distributions then the VMR must equal one. The VMR rises above one with the introduction of: i. uncorrelated fluctuations in the mean of the Poisson distribution, due, e.g., to uncorrelated fluctuations in laser power on the photocathode, and, ii. correlated fluctuations in counts over the $\frac{1}{W}$ chopping bandwidth, caused by flicker noise in the steering magnets and accelerating voltage, among other sources.

Figure 3.4(b) plots $\sqrt{\text{VMR}}$ (as defined in Eq. (3.1)) against lock-in frequency and compares two different scattering rates. We change the scattering rate by increasing the diameter of the probe-defining aperture from 10 to 70 μm . The two data sets are each fit to a $1 + Af^{-\alpha}$ trend line with free parameters A, α . At the highest lock-in frequency shown, 500 Hz, both data-sets are at the shot-noise floor. The intuition is that the higher the scattering rate, the higher the lock-in frequency required to hit the shot-noise-floor. This intuition is born out in the

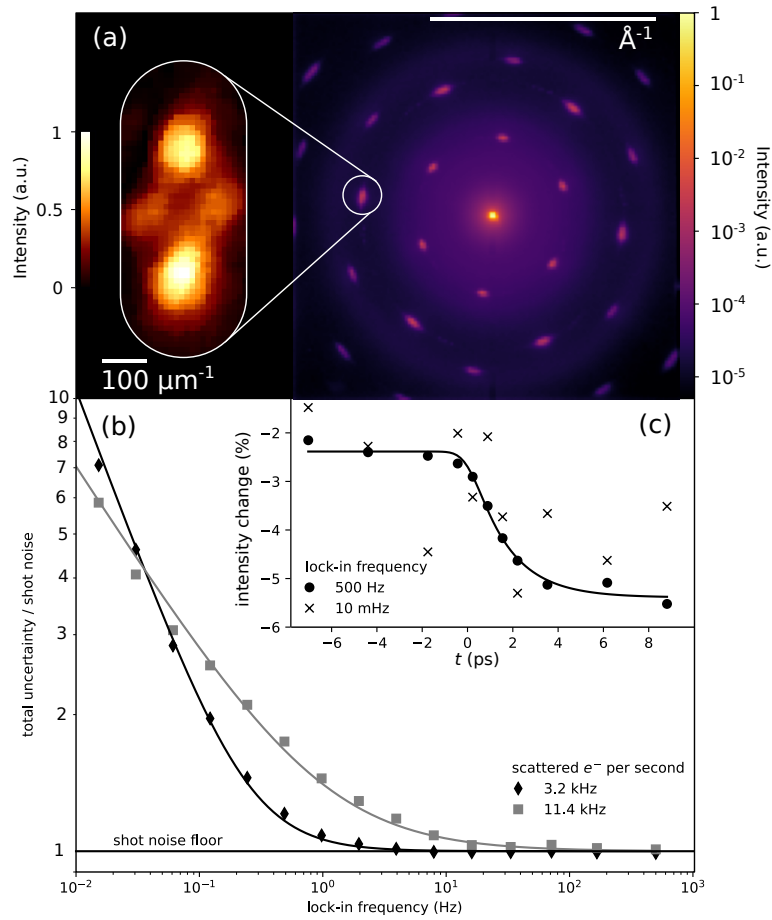


Figure 3.4: (a) Logarithmic scale diffraction pattern obtained from $\text{WSe}^2/\text{MoSe}^2$, demonstrating the EMPAD dynamic range. Highlighted in white, a long camera-length diffraction pattern showing a single, vertically aligned pair of Moire Bragg peaks: also visible, a pair of horizontally aligned satellite peaks, with 10 nm periodicity. Detector camera length is varied with a magnetic quadrupole lens triplet downstream of the sample (see Fig. 3.1). (b) Measurement uncertainty as a function of lock-in frequency: referring to the variance-to-mean ratio (VMR) defined in Eq. (3.1), the vertical axis shows $\sqrt{\text{VMR}}$ and can be interpreted as the ratio of total uncertainty to the shot noise limit set by the total integration time. Two curves compare different rates of scattering into the selected Bragg pair shown in (a); the different rates are obtained by increasing the radius of the probe defining aperture. (c) Measurement of the ultrafast Debye Waller effect, comparing data quality with high and low lock-in frequencies, each data point integrated for two minutes.

data: at the higher scattering rate, the VMR is appreciably greater than unity at lock-in frequencies below 100 Hz, while the VMR of the low scattering rate data only begins to rise above shot-noise below 10 Hz.

To illustrate the practical upshot of the lock-in technique in pump probe experiments, Figure 3.4(c) shows the measurement of the ultrafast Debye-Waller effect at two lock-in frequencies with the small probe beam. The trend is an exponential decay convolved with the instrument response, a good approximation of the curves typically obtained from two-temperature models of ultrafast heating [169]. The non-zero sample response at delay times earlier than the pump arrival is due to 1 kHz thermal cycling, further investigated below. Each data-point shown is acquired with a two-minute integration time. The spread in the data at the slow chopping rate (one minute hot, followed by one minute cold) is seen to be comparable to the size of the ultra-fast effect. In stark contrast, the data acquired at the 500 Hz lock-in frequency follows the fitted trend closely.

3.5 Diffusivity

As a demonstration of the experimental modalities made possible by a kHz frame rate detector, we perform ps- μ s- μ m thermometry on WSe₂/MoSe₂ via the Debye Waller effect. We deploy the pulse-picking method illustrated in Fig. 3.2 to scan pump-probe delays across six orders of magnitude. When employing this method, the detector frame rate sets the effective repetition rate of the probe, so that the kHz frame rate reduces the time required to perform the experiment from weeks with a conventional CCD to eight hours with the EMPAD.

In the double limit that the relaxed sample temperature is well above zero and the temperature change ΔT is small (both compared to the sample Debye temperature) the fractional change in the Bragg scattering rate $\Delta I/I$ with scattering vector \mathbf{k} is proportional to $k^2 \Delta T$. Hence, by scanning $\Delta I/I$ as a function of pump spatial position and pump delay, it is possible to map out thermal transport in the sample. We choose a low pump fluence of 2 mJ/cm^2 as a compromise between two desiderata: on the one hand, the linearity of the relationship between $\Delta I/I$ and T , and on the other, minimising Poisson noise in the measurement of $\Delta I/I$.

To model the heat transport phenomenology, we fit to our data an analytic, approximate solution to the inhomogeneous 2D heat equation,

$$\left[\frac{\partial}{\partial t} - \alpha \nabla^2 \right] T(t, \mathbf{x}; \alpha, A, \sigma_0) = f(t, \mathbf{x}; A, \sigma_0). \quad (3.2)$$

We parameterize the periodic solution $T(t, \mathbf{x}; \alpha, A, \sigma_0)$ with three time-independent scalars: the diffusion constant α , and the amplitude A and width σ_0 of the pump pulses. The forcing term $f(t, \mathbf{x}; A, \sigma_0)$ represents the pump periodically injecting energy into the system. Our model assumes: i. a square domain having side-length $L = 265 \mu\text{m}$, ii. that pump pulses strike the center of the square, and iii. that the boundaries of the square are held at constant temperature. We experimentally verify i. and ii., while iii. is highly plausible given the overwhelming thermal mass of the Si wafer in which the SiN-supported sample window is embedded. Equation (3.2) is solvable by Fourier series, and the analytic approximation we make consists in simply truncating this series to finite order. A subtlety is that the function we fit to our data is not directly the parameterized solution to Eq. (3.2) but instead the temperature difference G

between hot and cold lock-in half-cycles,

$$G(t, \mathbf{x}; \alpha, A, \sigma_0) := T(t, \dots) - T\left(t + \frac{W}{2}, \dots\right), \quad (3.3)$$

with W the lock-in period. From knowledge of G as defined in Eq. (3.3), as well as the boundary conditions on T , it is possible to completely recover T . A detailed derivation of the explicit expression for the fit function T is provided in the Supplemental Material.

The resulting fit of the model to our data is shown in Fig. 3.5. The three data dimensions are probe delay and probe position (both plotted horizontally) and the relative change in diffraction intensity (plotted vertically). The top horizontal axis shows probe delays and the bottom horizontal axes show position dependence. Data-points collected at the same probe delay are shaded the same color to aid in discriminating between spatial and time dependence, and for each spatial scan a gray arrow points to the delay at which the scan is performed. Solid lines show the spatial profile implied by the fitted model; the dashed line shows the fitted temperature envelope at the center of the sample square. The blue curve appearing on the horizontal axis at $0 \mu\text{s}$ shows the ultra-fast response taken at a pump delay of 20 ps.

The interpretation of Fig. 3.5 is that heat dissipates to the sample boundaries on at least two separated timescales: a fast timescale, $1 \text{ ns} < \tau_{\text{fast}} < 1 \mu\text{s}$, and a slow timescale $\tau_{\text{slow}} > 1 \text{ ms}$. The fit implies that the peak energy density in the bilayer following the arrival of the first pump-pulse has decayed to 5% of its value before the arrival of the second. This energy residue accumulates for the duration of the $440 \mu\text{s}$ pulses train and, following the end of the pulse train, relaxes exponentially at a rate set by the sample window size L : $\tau_{\text{slow}} = L^2/(\pi^2\alpha)$.

The fit in Fig. 3.5 gives the value $\tau_{\text{slow}} = 6 \text{ ms}$. When, as in our experiment,

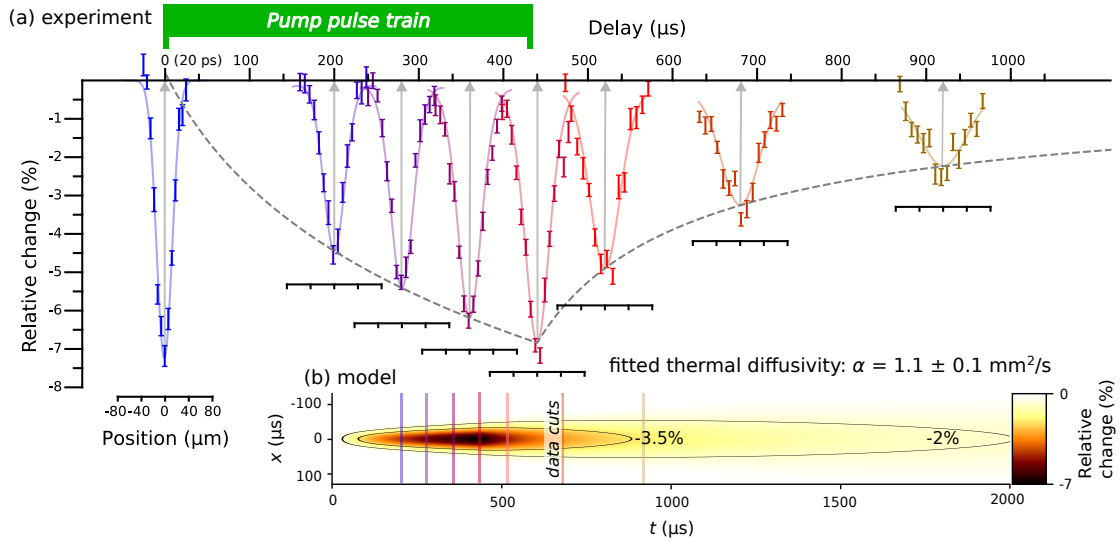


Figure 3.5: Sample thermometry performed at ps- μ s- μ m scales. The timing system, scanning technique and sample are shown in Figs. 3.2, 3.3. (a) The vertical axis shows the relative change in diffraction intensity, $\Delta I/I$, of the second-order Bragg pair highlighted in Fig. 3.4. The bottom horizontal axes show the displacement of the pump beam relative to the probe. Pump delay is indicated on the top horizontal axis: vertical gray arrows point to the delay at which each spatial scan is performed. The data plotted at 0 μ s show the ultrafast response of the sample to heating by the 515 nm, 2mJ/cm² pump laser after a 20 ps delay. Most of the energy deposited by one pump pulse is dissipated before the arrival of the next, but a residue remains trapped. To resolve the ramping of temperature as this residual energy accumulates over multiple pump pulse, we vary the length of the pump pulse train, up to a maximum of 440 μ s. Holding the pump pulse train length fixed at 440 μ s, we continue to increase the delay and spatially resolve the dissipation of energy to the sample boundaries. Pump trains cycle at 250 Hz, and we fit a steady-state, periodic diffusion model to the data described in Eq.(3.2) and following body text. Solid lines show the spatial temperature profiles predicted by the model at each delay, and the dashed line shows the temperature predicted by the model at the sample center. (b) Visualisation of the model, solid lines show contours of equal relative change. Vertical lines show the cuts at which spatial scans are performed, colors match the corresponding data in panel (a).

the period between pump pulse trains is less than the relaxation time, the sample reaches a periodic state in which the minimum temperature of the pumped region during a cycle remains elevated above the temperature of the boundaries. This steady-state offset scales linearly with the duration of the pump pulse train divided by the relaxation time. For example, in the data shown in Fig. 3.5, 440 μs pulse trains arrive every 4 ms and thus the energy density at the lowest ebb in the cycle is only a factor 1.5 times higher than the already small per-pulse residue. The estimate of τ_{slow} unambiguously defines the repetition rate that allows for the sample to relax before the arrival of each pump pulse in stroboscopic data acquisition: a surprisingly low 10^2 Hz.

It is outside the scope of this work to thoroughly investigate the mechanism that causes the separation of diffusion time scales we observe in our data. The spatial width of the bilyaer response shown in Fig. 3.5 is much narrower than the sample size, L , during the ramping phase at delays $< 440 \mu\text{s}$, and broadens to L in the relaxation phase, as the delay approaches 1 ms. The strongly-peaked spatial dependence in the ramping phase rules out the null hypothesis that the slower time scale is due to absorption in the SiN substrate. Recent photoluminescence experiments measuring the diffusivity of $\text{WSe}_2/\text{MoSe}_2$ have also observed a separation of diffusivities from 10^3 to $10^{-1} \text{ mm}^2/\text{s}$ at cryogenic temperatures [168]. Building on the discussion in that work, a possible room-temperature mechanism explaining the separation of scales we observe is that an initially fast-moving, quasi-free electron-hole plasma decays into interlayer-hybridized states; the interlayer states encounter friction from local potential minima created by the Moire pattern [170–172], and thus diffuse at a much slower rate at late times.

3.6 Summary and Outlook

This work has presented the first UED results to show the advantages of an integrating electron detector with high dynamic range and fast frame rate for pump-probe acquisition. Taking advantage of the 1 kHz frame rate, we implement a pulse-picking technique that allows us to investigate the response of a $\text{WSe}_2/\text{MoSe}_2$ bilayer to ultrafast excitation at ps- μ s- μ m scales. A natural extension of this technique is to utilize a GHz oscillator to pick pulses with nanosecond precision prior to the amplification stage. Such a system, when coupled with a delay stage to cover the range < 1 ns, would provide seamless delay capability from femtoseconds to seconds with femtosecond resolution. The next generation EMPAD increases the frame rate to 10 kHz [173], which raises the maximum lock-in detection frequency. Our results suggest that lock-in frequencies above 1 kHz, while unnecessary for our system in micro-diffraction mode, have the potential to dramatically improve signal-to-noise in experiments that involve large bunch charges of 10^5 electrons or more. By measuring the relaxation time of the sample out to the millisecond scale, we are the first to demonstrate an experimental method for unambiguously defining the sample-dependent optimal repetition-rate for ultrafast stroboscopic data collection. Our results highlight the need for pump-probe modalities that can access multiple time and intensity scales when investigating the rich, multi-scale physics of 2D quantum materials.

3.7 Supplemental Material

3.7.1 Materials and Methods

MoSe₂ and WSe₂ monolayers are exfoliated from bulk MoSe₂ and WSe₂ single crystals (HQ graphene) onto 285 nm SiO₂/Si substrate sequentially using a gold tape exfoliation technique [160], forming heterostructures with lateral dimensions of mm scale. The crystal orientations of the monolayers in the heterostructure are aligned with the crystal edges, and further confirmed in electron diffraction. The heterostructures are later transferred onto 10 nm thick, 250 μm \times 250 μm Si₃N₄ windows on TEM grids (SiMPore), using wedging transfer technique with cellulose acetate butyrate (CAB) polymer [174].

Pump and probe beams are aligned by performing knife-edge scans at the vertical and horizontal sample edges. Knife-edge scans gave a 9 μm rms pump size and a 6 μm rms probe size, implying a peak fluence of 2 mJ/cm².

3.7.2 Diffusion Model

In this section we derive an explicit expression for the function used to fit the data in Fig. 3 of the main text.

The fit function $T(x, y, t; \alpha, A, \sigma_0)$ with fit parameters α, A, σ_0 is a solution to the inhomogenous heat equation:

$$\frac{\partial T}{\partial t} - \alpha \left[\frac{\partial^2 T}{\partial x^2} + \frac{\partial^2 T}{\partial y^2} \right] = f(x, y, t; A, \sigma_0). \quad (3.4)$$

Equation (3.4) is subject to the condition that $T \equiv 0$ on a square boundary of side

length L . The origin of the Cartesian coordinate system x, y lies at the center of the square.

We model the forcing term f in Eq. (3.4) as a sequence of delta-function impulses, each having the same Gaussian spatial profile centered at the origin, with amplitude A and r.m.s size σ_0 . Pulses arrive in trains. Trains arrive at the rate ν and, within each train, pulses arrive at the rate R . Each train contains J pulses. The explicit expression for f is then,

$$f(x, y, t; A, \sigma_0) = \frac{4A}{L^2} \sum_{q=-\infty}^{\infty} \sum_{j=0}^{J-1} \sum_{m=0}^{M-1} \sum_{n=0}^{N-1} \cos\left((2m+1)\frac{\pi x}{L}\right) \cos\left((2n+1)\frac{\pi y}{L}\right) \exp\left\{-\frac{\sigma_0^2}{2} \left[(2m+1)^2 + (2n+1)^2\right] \frac{\pi^2}{L^2}\right\} \delta\left(t - \frac{j}{R} - \frac{q}{\nu}\right). \quad (3.5)$$

The sums in n, m are taken over Fourier modes that vanish at the boundary, truncated to orders $M, N = 10$.

We solve the inhomogeneous problem Eq. (3.4) by first solving for the response $T_0(x, y, t; \alpha, A, \sigma_0)$ to a single forcing pulse, treated as a homogenous problem with the forcing term accounted for in the initial conditions. The linearity of Eq. (3.4) then entails that,

$$T(x, y, t; \alpha, A, \sigma_0) = \sum_{q=-\infty}^{\infty} \sum_{j=0}^{J-1} T_0\left(x, y, t - \frac{j}{R} - \frac{q}{\nu}; \alpha, A, \sigma_0\right). \quad (3.6)$$

It is well known that for a single spatial Fourier mode $\hat{T}(k, t)$, the solution to the homogenous heat equation is,

$$\hat{T}(k, t) = \hat{T}(k, 0)e^{-\alpha t k^2}. \quad (3.7)$$

For the first impulse we therefore obtain,

$$T_0(x, y, t; \alpha, A, \sigma_0) = \frac{4A}{L^2} \sum_{m=0}^{M-1} \sum_{n=0}^{N-1} \cos\left((2m+1)\frac{\pi x}{L}\right) \cos\left((2n+1)\frac{\pi y}{L}\right) \exp\left\{-\frac{1}{2}(\sigma_0^2 + 2\alpha t) \left[(2m+1)^2 + (2n+1)^2\right] \frac{\pi^2}{L^2}\right\}. \quad (3.8)$$

Having in hand the expression for T_0 on the right hand side of Eq. (3.8), to compute the sums in Eq. (3.6), we first approximate the sum inside each train as an integral. It convenient to define three expressions that appear at intermediate steps in the computation,

$$E_{mn}(t; \alpha) := \exp\left\{-\alpha t \left[(2m+1)^2 + (2n+1)^2\right] \frac{\pi^2}{L^2}\right\}, \quad (3.9)$$

$$P_{mn}(t; \alpha) := E_{mn}(t; \alpha) * \sum_{j=0}^{J-1} \delta(t - j/R), \quad (3.10)$$

and,

$$\tilde{P}_{mn}(t; \alpha) := \sum_{q=-\infty}^{\infty} P_{mn}(t - q/v). \quad (3.11)$$

The approximating integral is then performed piece-wise in time, first for $t < J/R$, inside the pulse train,

$$P_{mn}(t; \alpha) = R \int_0^t E_{mn}(\tau; \alpha) d\tau \quad (3.12)$$

$$= \frac{L^2 R}{\alpha \pi^2 \left[(2m+1)^2 + (2n+1)^2\right]} [1 - E_{mn}(t; \alpha)] \quad (3.13)$$

Then, after the pulse train has ended, for $t \geq J/R$:

$$P_{mn}(t; \alpha) = \frac{L^2 R}{\alpha \pi^2 \left[(2m+1)^2 + (2n+1)^2\right]} [1 - E_{mn}(J/R; \alpha)] E_{mn}(t - J/R). \quad (3.14)$$

The remaining sum over all pulse trains can be computed using the for-

mula for a geometric series to give, for $t < J/R$:

$$\begin{aligned} \tilde{P}_{mn}(t; \alpha) &= \frac{L^2 R}{\alpha \pi^2 [(2m+1)^2 + (2n+1)^2]} \left\{ 1 - E_{mn}(t; \alpha) \right. \\ &\quad \left. + [1 - E_{mn}(J/R; \alpha)] E_{mn}(t - J/R; \alpha) \sum_{j=1}^{\infty} \exp \left\{ \right. \right. \\ &\quad \left. \left. - \frac{1}{2} \alpha j [(2m+1)^2 + (2n+1)^2] \frac{\pi^2}{fL^2} \right\} \right\} \end{aligned} \quad (3.15)$$

$$\begin{aligned} &= \frac{L^2 R}{\alpha \pi^2 [(2m+1)^2 + (2n+1)^2]} \left\{ 1 - E_{mn}(t; \alpha) \right. \\ &\quad \left. + [1 - E_{mn}(J/R; \alpha)] \frac{E_{mn}(t - J/R; \alpha)}{E_{mn}(-1/\nu; \alpha) - 1} \right\}, \end{aligned} \quad (3.16)$$

and for $t \geq J/R$,

$$\begin{aligned} &\tilde{P}_{mn}(t; \alpha) \\ &= \frac{L^2 R}{\alpha \pi^2 [(2m+1)^2 + (2n+1)^2]} [1 - E_{mn}(J/R; \alpha)] \frac{E_{mn}(t - J/R; \alpha)}{1 - E_{mn}(1/\nu; \alpha)}. \end{aligned} \quad (3.17)$$

The fit function expressed in terms of the \tilde{P}_{mn} is therefore,

$$\begin{aligned} T(x, y, t; \alpha, A, \sigma_0) &= \\ &\frac{4A}{L^2} \sum_{m=0}^{M-1} \sum_{n=0}^{N-1} \cos \left((2m+1) \frac{\pi x}{L} \right) \cos \left((2n+1) \frac{\pi y}{L} \right) \tilde{P}_{mn}(t; \alpha) \exp \left\{ \right. \\ &\quad \left. - \frac{1}{2} \sigma_0^2 [(2m+1)^2 + (2n+1)^2] \frac{\pi^2}{L^2} \right\}. \end{aligned} \quad (3.18)$$

CHAPTER 4

LOSSLESS MONOCHROMATION FOR ELECTRON MICROSCOPY WITH PULSED PHOTOEMISSION SOURCES AND RF CAVITIES

This chapter was originally published as reference [175].

4.1 Abstract

Resonant radiofrequency cavities enable exquisite time-energy control of electron beams when synchronized with laser driven photoemission. We present a lossless monochromator design that exploits this fine control in the one-electron-per-pulse regime. The theoretically achievable maximum beam current on target is orders of magnitude greater than state-of-the-art monochromators for the same space-time-energy resolution. This improvement is the result of monochromating in the time domain, unconstrained by the transverse brightness of the electron source. We show analytically and confirm numerically that cavity parameters chosen to minimize energy spread perform the additional function of undoing the appreciable effect of chromatic aberration in the upstream optics. We argue that our design has significant applications in ultrafast microscopy, as well as potential for use in non-time resolved microscopy, provided future photoelectron sources of sufficiently small size and laser sources of sufficiently high repetition rate. Our design achieves in simulations more than two orders of magnitude reduction in beam energy spread, down to single digit meV. Overcoming the minimum probe-size limit that chromatic aberration imposes, our design clears a path for high-current, high-resolution electron beam applications at primary energies from single to hundreds of keV.

4.2 Introduction

The electron-optical properties of time varying fields have long been of fundamental interest to electron microscopists and accelerator physicists [176–181]. Resonant radio-frequency (rf) cavities in particular have found significant use over the past two decades in time-resolved electron diffraction and microscopy. Highlights of a versatile range of applications include: compressing electron pulses in time to the femtosecond scale and below [182–189], temporal magnification of ultrafast events [190, 191], impulsive acceleration and deceleration of beams over short distances [67, 188, 192–194], chopping continuous beams into short pulses [194–198], and the controlled introduction of time-of-arrival correlations for performing energy measurements [188, 199]. Radio-frequency cavities are the workhorses of particle acceleration at primary energies above 1 MeV. Efforts to adopt rf technology for sub-MeV electron microscopes have faced the demanding requirement for fine precision in the timing of electron bunches. Early work on beam chopping at the picosecond scale resulted in the development of a GHz repetition rate SEM [200, 201], but contemporaneous investigation showed that picosecond precision was insufficient to realize the theoretical potential of cavities as high-quality electron lenses [181]. Today, advances in broadband laser sources and photocathode materials have allowed synchronising electron pulses with rf phases to single femtosecond precision [145], setting the stage for a new round in the fruitful exchange of expertise between the accelerator and microscopy research communities.

The focus of the present work is the use of cavity fields to compress beam energy spreads in the single-electron-per-pulse regime. Lower energy spread beams are advantageous in all electron microscopy, both static and time re-

solved. The importance to electron energy loss spectroscopy (EELS) is clear: monochromation of continuous-wave (CW) cold field emission (CFE) sources to the single meV scale has enabled measurements of phonon spectra with atomic spatial resolution in the scanning transmission electron microscope [202, 203]. Ultrafast pulsed beams of equally narrow energy spread would make it possible to resolve the different contributions of coupled lattice, charge, and spin dynamics to the spectrum of quantum materials [100]. In applications beyond spectroscopy, source energy spread limits the spatial resolution of electron microscopes. Chromatic aberration is the barrier to achieving atomic diameter probes at low primary energies of less than 5 keV [204], a commonplace regime for scanning electron microscopy and industrial meteorology methods, such as time-resolved cathodoluminescence. Finally, designs for damage-mitigating, pulsed multipass electron microscopes employ monochromation [205].

The challenge in producing low-energy spread beams is that the best sources have intrinsic spreads of hundreds of meV. To date, monochromator designs that reach the single meV energy scale have relied on apertures in energy-dispersive locations [206, 207]. Apertures cause a loss of beam current by a factor equal to the ratio between the desired energy spread and the source energy spread. A factor 100 reduction leaves little current for imaging in the continuous case [202], and prohibitively low current in the ultrafast case. Lossy monochromation at low voltages is infeasible because beam current must increase as accelerating voltage decreases to maintain a tolerable detector signal.

Pulsed sources combined with rf fields provide a direct experimental handle on the beam's longitudinal phase space, comprising the conjugate dynamical variables of forward momentum and time of arrival at a given transverse

plane [187, 208]. Photoemission is capable of delivering subpicosecond electron pulses with femtosecond timing precision to experimental targets. Lossless energy spread reduction is therefore possible because the time of arrival — and hence rf accelerating phase — is tightly correlated with the energy of the particle. In spectroscopy applications, rf monochromators and energy selecting apertures are not mutually exclusive elements of the microscope column. Pairing our design with a downstream, large acceptance energy selector, which admits between 50% and 100% of beam current, offers the ability to tailor the tails of the final energy distribution and mitigates subleading sources of energy spread.

The body of this paper begins in Sec. 4.3 with an analysis of the trade-off between current and energy spread in photoemission, and the statement of a fundamental lower bound on energy spread as a function of current on target. Considering photoemission from a planar source, Sec. 4.4 derives and solves analytic conditions on the cavity parameters for energy-spread minimization. Particle tracking simulations confirm these analytic results. Precise synchronization is essential to minimising energy spread in our scheme and Sec. 4.5 analyses the effect of timing jitter at the single femtosecond scale, precision that has been achieved with bunching cavities in ultrafast diffraction beam lines [145]. Section 4.6 investigates the effect of the cavities on the transverse coherence of the beam. Analytic results show that the same cavity parameters that are optimal for energy spread reduction also perfectly cancel the effects of spherical and chromatic aberrations in the electron gun. We compare this prediction of our analytical formula with particle tracking simulations.

4.3 Fundamental trade-off between energy resolution and beam current

Monochromation entails a trade-off between final energy spread and average current on target, both in existing aperture-based energy-selectors and our proposed lossless design. Figure 4.1 shows a schematic of our design side-by-side an energy-selector. The constraints that impose the current-energy trade-off are different between the two devices. A comparison helps to situate our design in relation to the state of the art. A first analysis is simplified by neglecting the contribution that transverse momenta make to total particle energy. The end of this section returns to the complication introduced by accounting for the transverse store of energy.

The conservation of longitudinal emittance in a pulsed beam relates the minimum energy spread achievable in lossless transport $\Delta\mathcal{E}_{\min}$ to the initial laser pulse length Δt_l at the source, the final electron pulse length Δt_f , and the initial electron energy spread ΔK :

$$\Delta\mathcal{E}_{\min} = \frac{\Delta t_l}{\Delta t_f} \Delta K \geq \frac{\hbar}{2t_f}. \quad (4.1)$$

The rightmost inequality is a consequence of the Heisenberg uncertainty principle, which sets the fundamental limit to longitudinal emittance. The factor Δt_l includes the response time of the photocathode: on the scale of 10 fs [209] for typical metallic photocathodes, and extending much longer (up to 100 fs and above) for semiconductor photocathodes [210, 211]. The single-electron-per-pulse regime reaches the lowest possible emittances (both transverse and longitudinal) because of the absence of Coulomb interactions that would otherwise broaden the energy distribution and spoil transverse coherence. At GHz

or slower repetition rates, and primary energies of 10 keV or more, successive pulses are separated by distances greater than 1 cm, so that interactions between pulses are safely neglected. In this regime, an upper bound on the average current of a laser-driven system synchronized to rf cavities is $I_{av} = fe$, where e is the electron charge and f is the resonant frequency of the cavities. Poisson emission statistics imply that a current less than this upper bound is required to adequately mitigate the effect of Coulomb interactions, but the difference is an order unity factor and appropriately neglected in the present scaling analysis. In time-resolved, pump-probe systems, the maximum practicable repetition rate is set by the time it takes the sample to relax to the ground state after pump excitation. Relaxation times vary significantly depending on the sample and the desired excitation strength.

Pulses that stretch to fill the entire rf cycle acquire unwanted nonlinear energy-time correlations, and these higher-order effects thus bound the allowable final pulse length. Let the *duty cycle* D denote the ratio of final pulse length to rf period. Substituting the duty cycle into Eq. (4.1) yields an expression for our design's maximum average current:

$$I_{av} = \frac{De}{\Delta t_l} \frac{\Delta \mathcal{E}_{\min}}{\Delta K} = I_{pk} D \frac{\Delta \mathcal{E}_{\min}}{\Delta K}, \quad (4.2)$$

where $I_{pk} := e/\Delta t_l$ is the peak current at the cathode. Energy-selecting monochromators also show a linear scaling of average current with the fractional reduction in energy spread. The optimal performance of our monochromator is thus equivalent to an energy selector with an effective input current of $I_{pk}D$. An estimate of the allowable values of D depends on the details of our monochromator design. As shown in Sec. 4.4, minimising final energy spread requires that the energy gain from the cavities depends quadratically on time. Figure 4.2 plots the cubic and higher-order time dependence of the work done

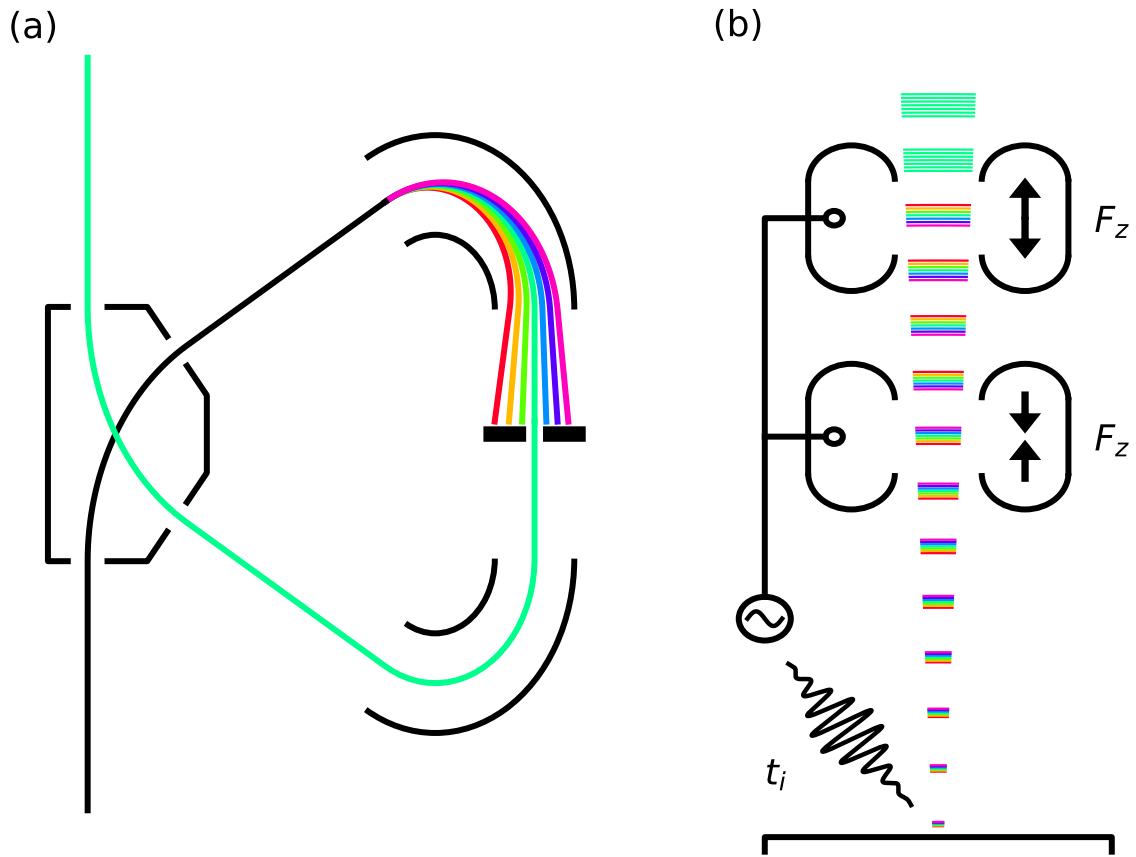


Figure 4.1: (a) Energy selecting monochromator as described in [206]: magnetic prisms disperse the energy spectrum of the electron beam in the transverse direction and a narrow acceptance slit selects the desired bandwidth at the cost of lost current. (b) Our lossless monochromator design: photoemission is triggered by a laser pulse and the beam energy spectrum disperses in the longitudinal direction. Time-correlated acceleration in the pair of cavities, indicated by force vectors in the figure, equalizes the energies of the dispersed beam. The average current in our design is limited by the cavity frequency.

by a single cavity on a logarithmic scale. Inspection of the figure indicates that choosing $D < 0.1$ suppresses the higher-order contributions to the 1% level or lower. Modern ultrafast laser oscillator sources can provide multiple GHz repetition rates with pulse durations well below 30 fs [212]. For a total emission time of $\Delta t_l = 30$ fs, and assuming $D = 0.01$, we arrive at $I_{pk}D = 50$ nA, which compares favorably with the order 1 nA current delivered from CFE sources to state-of-the-art TEM monochromators [202], of like design to the diagram shown in Fig. 4.1(a). It bears repeating with respect to this example that 50 nA is not the average current input into the rf monochromator — our rf design is lossless and so the average current is the same upstream and downstream, equal to $50 \text{ nA} \times \Delta \mathcal{E}_{\min} / \Delta K$.

Constrained by the transverse brightness of the electron source, energy selection in the spatial domain confronts a trade-off between energy and spatial resolution. The 10 pA scale of the maximum current the CFE energy selector delivers to the experimental target is a consequence of balancing the objectives of angstrom scale spatial resolution against 10 meV scale energy resolution [213]. A CFE source delivering 1 nA to the selector input, accelerated to 100 keV at a brightness of $10^9 \text{ A cm}^{-2} \text{ Sr}^{-1}$, has a normalised transverse emittance of 1 pm, less than the Compton wavelength of the electron and a factor five greater than the fundamental lower bound set by the quantum uncertainty principle. There is thus room for increases in current on target with existing energy selector technology as the transverse emittance of the highest-resolution instruments approaches the quantum limit.

The rf monochromator presented in this paper balances an orthogonal trade-off between temporal resolution and energy resolution, constrained by longitu-

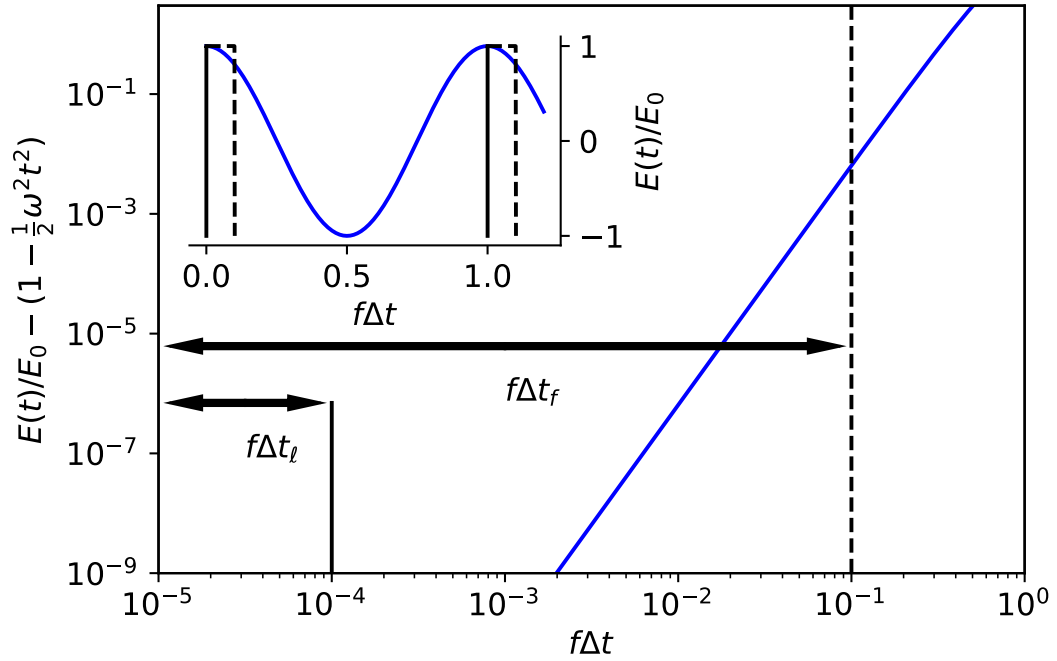


Figure 4.2: Normalized energy gain versus the single particle time of arrival, expressed as a fraction of the full rf period. The quadratic coefficient of the energy gain is subtracted, leaving only unwanted higher-order terms. Vertical lines show the initial pulse length Δt_ℓ (solid) and final pulse length Δt_f (dashed). The duty cycle in Eq. (4.2) is $f\Delta t_f$. Inset shows the full sinusoidal energy gain versus the scaled time of arrival, with the quadratic term restored.

dinal brightness. Holding the pulse length and energy spread at the sample constant, a reduction in the initial pulse length results in higher current on the target. Compared to transverse brightness, there is far greater scope for future improvements in longitudinal brightness, given that the best ultrafast sources in use today — at 10 to 100 fs pulse lengths and 100 meV energy spread — are hundreds of times poorer than the fundamental brightness limit. To calculate the fundamental theoretical ceiling on the current that the rf monochromator can deliver to an experimental target, we assume an initial pulse length that

approaches the quantum limit, $\Delta t_i \Delta K = \hbar/2$. Then, letting the duty cycle be $D = 0.01$ and the final energy spread be 10 meV, the current on target is 20 nA, three orders of magnitude potential improvement. The implied repetition rate at an average current of 20 nA is 120 GHz, not practically feasible with present technology. Nevertheless, this example serves as a signpost of the ultimate, physical limits of rf monochromation in the one-electron-per-pulse regime.

Both metallic photoemission and cold field emission sources in use today produce energy spreads of multiple hundreds of meV [202, 214–216]. A final spread of 5 meV is an appropriate benchmark, being the resolution required to resolve phonons in EELS and to reduce chromatic aberration in objective lenses by more than an order of magnitude. A target $\Delta \mathcal{E}_{\min}$ of 5 meV from a $\Delta K = 500$ meV source with initial pulse length $\Delta t_i = 30$ fs implies a final pulse length of 3 ps, a resonant cavity frequency of ~ 3 GHz, and an average current of 500 pA. An average current of 500 pA is more than sufficient for imaging above 10 keV primary energy, and cavities and rf sources at 3 GHz are well explored in both accelerator and time-resolved experimental work. Additionally, with the reduction in laser repetition rate (by pulse picking, for example) to accommodate sample recovery times in pump probe experiments, 3 ps resolution enables the tracking of phonon population evolution in time [217].

In the applications of interest, the cathode makes the dominant contribution to energy spread, with the subleading contribution coming from fluctuations in the accelerating voltage. Our design specifically corrects source energy spread, relying on the correlation between *initial* kinetic energy and time and position of arrival. Section 4.5, on jitter, suggests how to incorporate into our design fast feedback from existing beam diagnostic devices so as to compensate subleading

sources of energy spread.

The advantage of lossless monochromation over energy selectors for time-resolved applications is that users can obtain improved energy resolution without paying a cost in average current. For applications that at present obtain the best performance from CW beams, the scaling with peak current in Eq. (4.2) points to the potential superiority of pulsed beams with lossless monochromation as higher-brightness photoemission sources become available. The two dimensions of active research toward higher-brightness photoemitters are lower source energy spread and smaller source size. Measurements of photoemission from cryo-cooled alkali-antimonide photocathodes have shown source energy spreads on the 10 meV scale [24, 218], an order of magnitude smaller than CFE sources. Photoemitting tips yield nanometer source sizes, smaller than the diffraction limited laser spot diameter [215]. A hypothetical alternative to a tip geometry is to layer a photoemission mask on planar cathodes, exposing a photoemitting disc with a diameter on the scale of 10 nm. The simulation results we present in Sec. 4.4 make practical assumptions about the photoemission source that anticipate future trends. We consider a planar cathode geometry with an rms source size of 12 nm and initial uniform energy spreads of 0.1, 0.5 and 1 eV. The physics that makes rf monochromation possible, which the next section describes, does not depend on assumptions about source quality.

The discussion in this section is completed by considering transverse spatial degrees of freedom. The contribution that the transverse momenta make to total energy spread implies a parallel trade-off between transverse beam size and energy spread. Therefore, including the transverse contribution makes possible a reduction in energy spread without a compensating increase in pulse length. A

natural mechanism to imagine realizing this possibility is a radial electric field that performs work to reduce the energy stored in the transverse momentum and, as a byproduct, collimates the beam. Our design employs a similar mechanism, conceptually more complicated but simpler to engineer. Our design, after expanding the beam, applies a spatially varying longitudinal field so as to balance an energy surplus in the transverse direction by creating an energy deficit in the longitudinal direction.

Altogether, our design achieves its final energy spread by stretching the beam both transversely and longitudinally. The spatial and temporal trade-offs do not originate from two distinct constraints, but are instead both consequences of the conservation of the six-dimensional phase space volume. Thus, if the expanded, reduced energy spread beam is again focused down to its source size or smaller by magnetostatic lenses, then the pulse length stretches as the beam size shrinks. Magnetostatic lenses do no work and hence have no effect on energy spread, but produce pulse stretching due to variations in the path lengths traced by particles. In the applications of our monochromator previewed in the Introduction, there is more experimental flexibility to trade longer pulses for lower energy spread than there is to vary beam size at the experimental target. Hence, Eq. (4.1) formulated only in terms of the longitudinal variables captures the essential physics of our monochromator design.

4.4 Energy equalization

4.4.1 Qualitative summary

Our monochromator design operates in two steps. First, the system of electron source and optical column correlates energy with time and position of arrival, stretching the electron pulse in time and space. The uncorrelated energy spread decreases as the pulse is stretched. In the second step, the rf fields remove the correlated energy spread.

Correlations between energy, time and space naturally arise near zero energy in the low-to-moderate extraction fields (1 – 10 MV/m) of a dc (i.e. electrostatic) gun, which our design exploits. Figure 4.3 shows the field-map used to simulate the electron gun alongside a plot of the position of downstream beamline elements. Illustrative snap shots of the evolution of energy correlations in simulation are shown in Fig. 4.4. An alternative method for stretching electron pulses is to insert a dedicated device comprising rf cavities and drift space [186, 219]. Our omission of dedicated stretching cavities has the advantage of simplicity. Furthermore, by relying on the gun field to stretch the pulse, our design does not require significant drift space for stretching to develop. In this section, we derive an analytical model of stretching in an idealized gun field and confirm the model’s accuracy in particle tracking simulations.

Two rf cavities correct the kinetic energy spread contained in the time (cavity one) and transverse position (cavity two) degrees of freedom. Both cavities are identical in design, comparable to the device described in [187]. A three-dimensional rendering of our cavity is shown in Fig. 4.5. This section computes

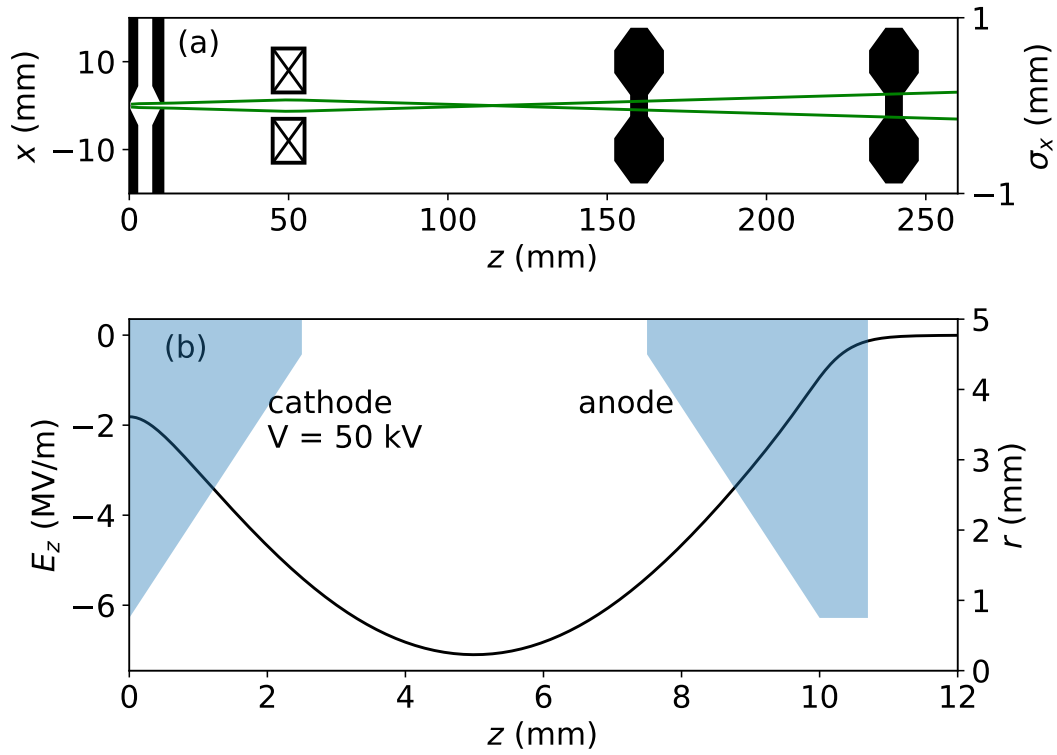


Figure 4.3: (a) Simulated source and monochromator layout in the x - z plane. The left axis is the transverse scale for the optical elements. All elements are axially symmetric. The transverse beam size is shown by the green curve, with the scale indicated by the axis on the right. The cathode and anode are at $z = 0, 10$ mm, respectively. At $z = 50$ mm is a focusing solenoid; at $z = 160, 240$ mm, dumbbell silhouettes approximate cavity cross sections. (b) Electrode profile and axial field $E_z(z)$ in the gun for a voltage of 50 kV.

to good accuracy the settings of cavity phases and amplitudes that minimize the final energy spread.

Simply knowing the initial kinetic energy of a particle does not uniquely determine its time and position of arrival at the cavities. Instead, we derive the inverse relationship: the initial kinetic energy as a function of the time and

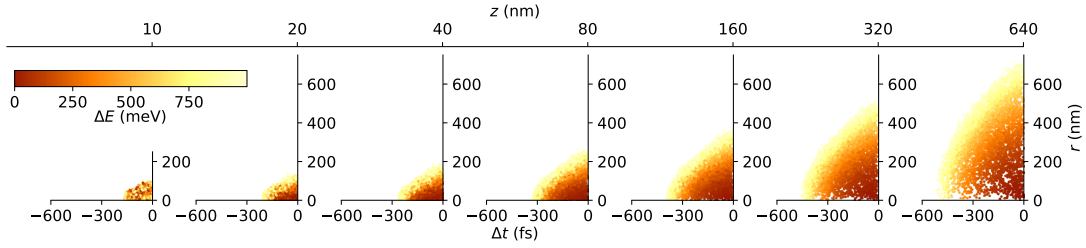


Figure 4.4: Evolving correlation between the energy, radial position r , and time of arrival Δt in a dc electron gun. Results plotted are of single particle trajectory simulations. The accelerating field is uniform with a gradient of 5 MV/m. Each subplot shows the cross section of radial position and time of arrival at the exponentially increasing values of z indicated on the top axis. Color indicates particle energy $\Delta\mathcal{E}$ relative to the minimum energy in the statistical ensemble; Δt is defined relative to the last arriving particle. As the uncertainty in time and position grows, the correlation with energy tightens. Uncertainty in time of arrival asymptotically approaches the value predicted by Eq. (4.5) as the energy gained in acceleration comes to dominate the initial kinetic energy. The initial statistical ensemble in all our simulations, unless otherwise specified, is uniformly distributed in energy, time of emission, and solid angle over the forward hemisphere [214].

position of arrival at the cavities. The exit of the gun serves as the primary reference plane for particle coordinates. Any equipotential plane downstream of the anode would fulfil this role equally well. Our analytic model ignores fringing effects and thus takes the anode to be the gun exit. The initial kinetic energy is nonrelativistic and thus proportional to the sum of squares of initial momenta. Our problem thus reduces to expressing each of the three initial momenta separately in terms of their conjugate coordinates at the gun exit.

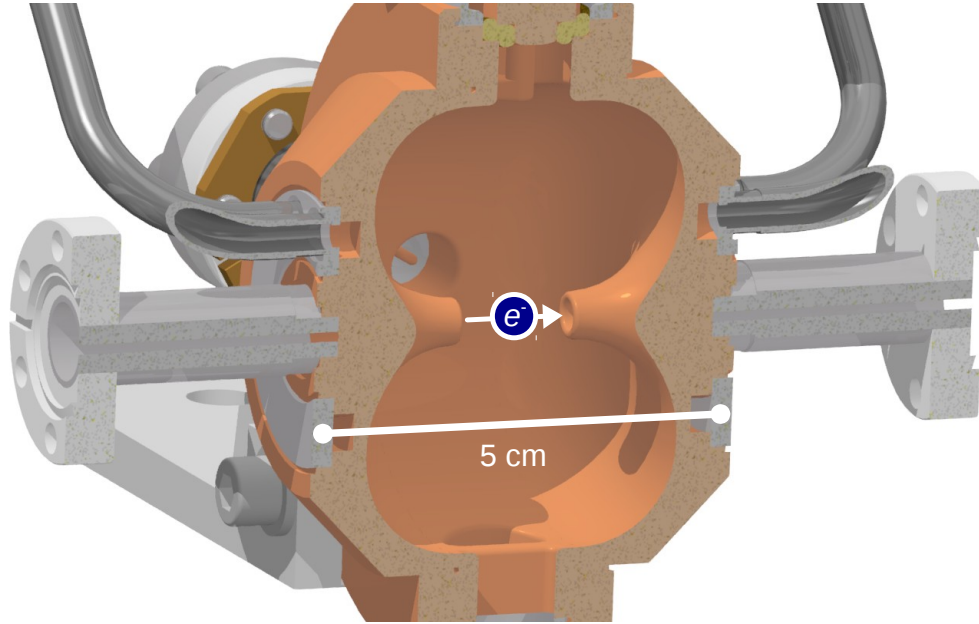


Figure 4.5: Cross section of the 3 GHz TM010 mode cavity used in the energy equalization device described in this paper.

4.4.2 Correlation between emission energy, arrival time, and position

We begin by deriving the initial longitudinal momentum of a particle as a function of time of arrival at the reference plane, the gun exit. For our analytic derivation, we assume that the gun is a uniform field of strength $E_z^{\text{cat}}\hat{\mathbf{z}}$. We relax this assumption later. As is standard in electron optics, we take longitudinal position z to be the independent variable of electron motion and treat time of arrival t as a function of z . Differences in times of arrival Δt , as measured by a clock at rest in the laboratory frame, play a crucial role in the derivation and should not be mistaken for time as measured in a frame comoving with the beam. Our reference frame is at rest with respect to the laboratory throughout. The relativistic equations of motion for a charged particle in a uniform electric

field $E_z^{\text{cat}}\hat{\mathbf{z}}$, solved for $t(z)$, give,

$$t(z) = t_0 + \frac{p_{z0}}{eE_z^{\text{cat}}} + \sqrt{\frac{z^2}{c^2} - \frac{2z\gamma_0 m_e}{eE_z^{\text{cat}}} + \frac{p_{z0}^2}{(eE_z^{\text{cat}})^2}}, \quad (4.3)$$

where t_0 is the time of emission, p_{z0} is the initial longitudinal momentum at the cathode, and γ_0 is the initial relativistic energy factor at the cathode. Three terms add in quadrature under the square root, and we name them for convenience. First, the *ultra-relativistic time of flight*, z/c , which is the time it would take a photon to travel the distance to z . Next, the *Newtonian time of flight* $\sqrt{-2zm/eE_z^{\text{cat}}}$ is the time it would take a nonrelativistic particle of mass $m = \gamma_0 m_e$ to reach z , starting at rest. Finally, the *stopping time* $-p_{z0}/eE_z^{\text{cat}}$ is the time it would take the accelerating gradient to stop a particle fired toward the cathode with initial momentum $\mathbf{p} = -p_{z0}\hat{\mathbf{z}}$.

In the regime of interest — particles with ~ 1 eV initial energies and > 1 keV final energies — the smallest term is the stopping time. If we have $E_z^{\text{cat}} = -1$ MV/m, the stopping time of an electron with velocity $v_z/c = 0.002$ is 3 ps, the ultra-relativistic time of flight across a cathode gap of 1 cm is 30 ps, and the corresponding Newtonian time of flight is 500 ps.

In order to estimate the error that arises from neglecting the stopping time, we can expand the square root appearing in Eq. (4.3) in powers of the small quantity

$$\delta = \frac{p_{z0}^2}{(eE_z^{\text{cat}})^2} \left(\frac{z^2}{c^2} - \frac{2z\gamma_0 m_e}{eE_z^{\text{cat}}} \right)^{-1}, \quad (4.4)$$

which is proportional to the square of the stopping time. Then, for the example values cited above, the correction term first order in δ is ~ 10 as. The relevant scale to compare is the uncertainty in the time of emission of a single electron packet Δt_l , equal to the the laser pulse length and photoemission response time, which are on the order of 10 fs. Thus, the stopping time can safely be neglected

inside the square root. Under the assumption that all initial kinetic energies are of single eV scale or less, it is also safe to assume that $\gamma_0 = 1$, and no remaining term inside the square root appearing in Eq. 4.3 depends on the initial conditions. Thus, the square root drops out from the difference in arrival times Δt between two particles, and Δt becomes linearly proportional to the difference in their initial longitudinal momenta Δp_{z0} ,

$$\Delta t = \frac{\Delta p_{z0}}{eE_z^{\text{cat}}} + \Delta t_0, \quad (4.5)$$

with Δt_0 the difference in emission times (relative to the arrival time of the laser pulse).

The most convenient choice of reference particle is the particle with zero initial kinetic energy. Arrival time differences Δt therefore give us the p_{z0} of all particles up to the precision set by Δt_l , which is 1% for the example values.

The coefficient of proportionality appearing in Eq. (4.5) is independent of z and thus the gun length. A dependence on gun length is absent because the relative time of arrival is frozen for z large enough that $\delta \ll 1$, per Eq. (4.4). To describe this freezing effect more explicitly, consider two particles with longitudinal velocities $\beta_{z1}(z)c$, $\beta_{z2}(z)c$ that differ in arrival time by $\Delta t(z_1)$ at longitudinal position z_1 . The difference in arrival time of the same two particles at a downstream location z_2 is

$$\Delta t(z_2) = \Delta t(z_1) + \int_{z_1}^{z_2} \frac{[\beta_{z2}(z) - \beta_{z1}(z)] dz}{\beta_{z1}(z)\beta_{z2}(z) c}. \quad (4.6)$$

Now suppose an accelerating gradient such that as z_1 goes further downstream, the greater is the mean particle energy. It then follows that, for z_1 sufficiently far from the cathode, the integrand on the right-hand side of Eq. (4.6) vanishes and Δt becomes independent of z , no matter the functional dependence of velocity on position. The freezing of time of arrival differences makes it possible to

generalize Eq (4.5) to nonuniform accelerating fields by replacing E_z^{cat} with the photocathode field. The resulting expression is accurate so long as (i) the photocathode field is approximately uniform over a distance z such that $\delta \ll 1$ and (ii) the particle velocities are increasing functions of z for the remaining length of the gun.

Fluctuations in the accelerating gradient, typically at the 10^{-5} level or below, affect electron time of flight and are a subleading source of uncertainty in the correlation between Δt and p_{z0} . To estimate the significance of this effect, we expand Eq. (4.3) to linear order in the gradient fluctuation ΔE_z^{cat} . Letting z_{gun} be the location of the gun exit and z a location in the drift region downstream of the gun, the resulting change in arrival time $\Delta t_{\text{gun}}(z)$ is,

$$\Delta t_{\text{gun}}(z) = -\frac{1}{4} \frac{\Delta E_z^{\text{cat}}}{E_z^{\text{cat}}} \left(1 + \frac{z}{z_{\text{gun}}}\right) \sqrt{-\frac{2z_{\text{gun}}m_e}{eE_z^{\text{cat}}}}. \quad (4.7)$$

The expression in Eq. (4.7) neglects relativistic terms, which, if included, further suppress the size of Δt_{gun} . The estimate for $E_z^{\text{cat}} = -1$ MV/m and $z_{\text{gun}} = 1$ cm, $z = 10$ cm is $\Delta t_{\text{gun}}(z) < 10$ fs, less than the dominant contribution to time of flight uncertainty from the emission process Δt_l .

As for the transverse coordinates, the solution to the equation of motion in x (without transverse focusing) is,

$$x = \frac{p_{x0}}{m_e} \tau + x_0, \quad (4.8)$$

with x_0 the coordinate of the particle at emission and τ the proper time that elapses between emission of the particle and its crossing the transverse plane at z . The coordinate y follows from cylindrical symmetry. Let $\tau_*(z)$ be the proper time to reach z of the reference particle (initially at rest). Expanding τ in p_{z0}

around $\tau_*(z)$,

$$\begin{aligned}\tau &= \tau_* + \frac{d\tau}{dp_{z0}} p_{z0} + \mathcal{O}(p_{z0}^2) \\ &= -\frac{m_e c}{e E_z^{\text{cat}}} \mathcal{A}(\gamma_*) + \frac{p_z}{e E_z^{\text{cat}}} + \mathcal{O}(p_{z0}^2).\end{aligned}\quad (4.9)$$

Here, the variable $\gamma_*(z)$ is the relativistic factor for the reference particle and,

$$\mathcal{A}(\gamma_*) := \ln \gamma_* + \ln(1 + \beta_*), \quad (4.10)$$

with $\beta_*(z)c$ the velocity of the reference particle. Dividing Eq. (4.8) by Eq. (4.5) shows that \mathcal{A} approximates the aspect ratio $x/c\Delta t$; hence, the choice of notation.

To find the initial kinetic energy K as a function of a particle's position and time of arrival, we simply square previous expressions derived for momenta, i.e.,

$$K(\Delta t, x, y) = \frac{(e E_z^{\text{cat}})^2}{2m_e} \left[(\Delta t - t_0)^2 + \frac{(x - x_0)^2 + (y - y_0)^2}{c^2 \mathcal{A}^2} \right], \quad (4.11)$$

recalling that Eq. (4.10) defines the aspect ratio \mathcal{A} and that E_z^{cat} is the cathode field. To arrive at this result, we make the approximation $\tau = \tau_*$. Simulation results verifying Eq. (4.11) are presented below in Sec. 4.4 D. The leading correction to Eq. (4.11) comes from considering the linear order in the expansion of τ shown in Eq. (4.9), which contributes a cubic term to the right-hand side of Eq. (4.11),

$$\frac{\partial^3 K}{\partial t \partial r^2} = \frac{2(e E_z^{\text{cat}})^3}{m_e^2 c^3 \mathcal{A}^3}. \quad (4.12)$$

The relative size of this cubic term is,

$$\frac{\partial^3 K}{\partial t \partial r^2} \Delta t \Big/ \frac{\partial^2 K}{\partial r^2} = \frac{2\gamma_0 \beta_{z0}}{\ln \gamma_* + \ln(1 + \beta_*)} \sim \frac{\beta_{z0}}{\beta_*}. \quad (4.13)$$

The initial longitudinal particle velocity β_{z0} is on the order 10^{-3} for electrons emitted with kinetic energies less than 1 eV. The final velocity $\beta_* \approx 0.5$ at an accelerating voltage of 50 kV. Thus, for pulse stretching factors approaching

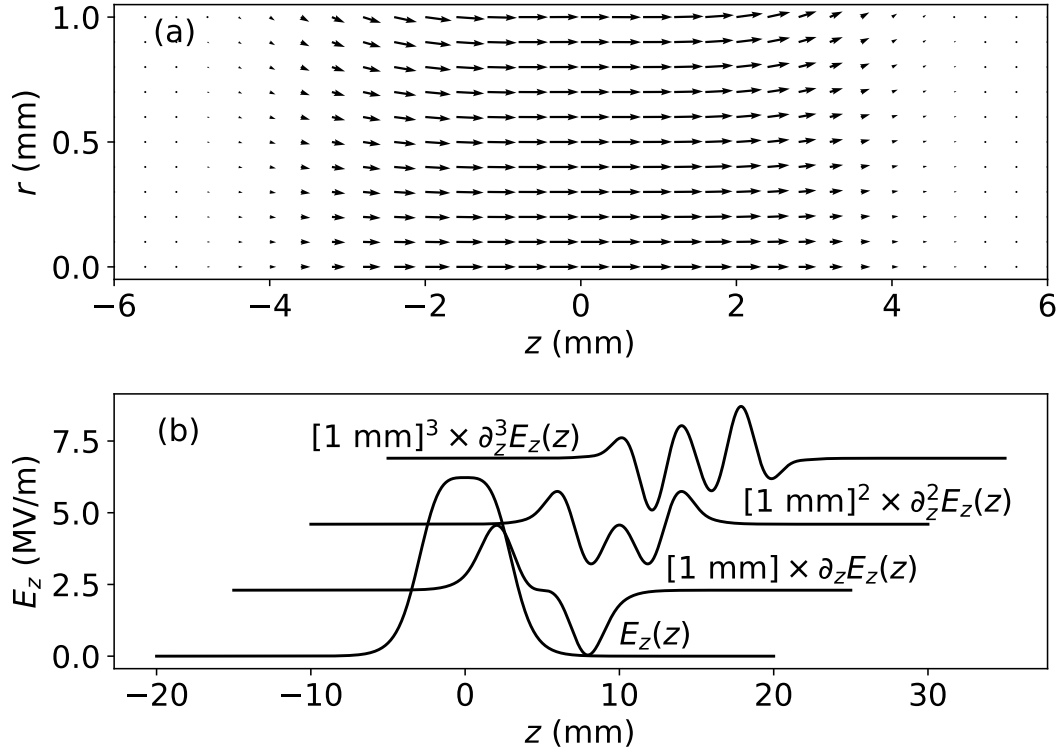


Figure 4.6: Simulation cavity field map: (a) z, r cross section of the radially symmetric cavity \mathbf{E}^{rf} field at nominal amplitude and phase; (b) the axial cavity field $E_{0,z}^{\text{rf}}$ and its leading spatial derivatives, from which we construct the simulation field map.

1000 or more, cubic-order correlations put a floor on the final energy spread achievable with our two-cavity solution at parts per thousand the initial energy spread.

4.4.3 Cavity fields

Knowing the initial kinetic energy of a particle as a function of the coordinates $\Delta t, x, y$ in the transverse plane at z , we must derive the matching expression

for the work done by the cavity fields on transiting particles. For the purpose of this derivation, we make the following rigid-beam approximation, which is exact in the limit that the change in momentum due to the cavity field is small compared to the mean particle momentum. Namely, we assume that particles transit with constant velocity βc parallel to the symmetry axis. In this limit, only the longitudinal component of the cavity electric field contributes to the work done. Figure 4.6 shows the electric field of the TM010 mode supported by our cavity design.

The longitudinal component of *any* axially symmetric transverse magnetic mode expands in powers of derivatives of the on-axis longitudinal field $E_{0,z}^{\text{rf}}$ as,

$$E_z^{\text{rf}}(t, z, r) = J_0 \left[r \sqrt{\frac{\partial^2}{\partial z^2} + \frac{\omega^2}{c^2}} \right] E_{0,z}^{\text{rf}}(z) \cos(\omega t + \phi_0), \quad (4.14)$$

where J_0 is the zeroth-order Bessel function, which for operator arguments is defined by the power series,

$$J_0 \left[\frac{\partial}{\partial z} \right] := \sum_{k=0}^{\infty} \left(\frac{-1}{4} \right)^k \frac{1}{(k!)^2} \frac{\partial^{2k}}{\partial z^{2k}}. \quad (4.15)$$

We define the free parameter ϕ_0 such that at $\phi_0 = 0$ the reference particle undergoes the maximum change in energy. Appendix 4.9 presents a derivation of Eq. (4.14). Integrating the right-hand side of Eq. (4.14) by parts to all orders in the derivative expansion gives the work W as a function of the radial coordinate $r = \sqrt{x^2 + y^2}$ and the time of arrival t ,

$$\begin{aligned} W(r, t) &= - \int_{-\infty}^{\infty} e \mathbf{E}^{\text{rf}} \cdot d\mathbf{s} \approx - \int_{-\infty}^{\infty} e E_z^{\text{rf}}(t(z), z, r) dz \\ &= -J_0 \left(\frac{2\pi i r}{\beta \gamma \lambda} \right) \cos(\phi) \int_{-\infty}^{\infty} e E_{0,z}^{\text{rf}}(z) \cos \left(\frac{2\pi z}{\beta \lambda} \right) dz, \end{aligned} \quad (4.16)$$

with $\phi = \omega \Delta t + \phi_0$ and Δt the difference in time of arrival at the gun exit, the same variable appearing in Eq. (4.11). Referring the time of arrival to the gun

exit in this way is an approximation valid in the limit that drift sections between elements after the anode are short, which is the regime of interest. The intermediate steps in performing the integrations by parts are presented in Appendix 4.10. The integrand on the right-hand side of Eq. (4.16) is independent of r and t . Hence, neglecting the small spread in β , it is possible to define an effective cavity length d_{rf} and voltage [187]. Letting E_{\max}^{rf} be the maximum accelerating field on axis,

$$d_{\text{rf}} := \frac{1}{E_{\max}^{\text{rf}}} \int_{-\infty}^{\infty} E_{0,z}^{\text{rf}}(z) \cos\left(\frac{2\pi z}{\beta_* \lambda}\right) dz. \quad (4.17)$$

Choosing $\phi_0 = 0$ simplifies the conditions for canceling the quadratic dependence of energy on time appearing in Eq. (4.11). With $\phi_0 = 0$, the expression for W expands to quadratic order in r and t as,

$$W(r, t) = -d_{\text{rf}} e E_{\max}^{\text{rf}} \left(1 - \frac{1}{2} \omega^2 \Delta t^2 + \frac{\pi^2}{\beta^2 \gamma^2} \frac{r^2}{\lambda^2} \right). \quad (4.18)$$

The term in r enters Eq. (4.18) with the opposite sign to its counterpart in t because Eq. (4.14) requires the peak of $E_{z,0}^{\text{rf}}(z)$ to be a saddle point in three dimensions.

4.4.4 Analytic prediction of cavity parameters

By incorporating two cavities in the monochromator, it is possible to make the cumulative energy gain a concave down quadratic function of both time and space. A negative quadratic dependence cancels the positive dependence imprinted at the electron source. This strategy introduces the design problem of optimising beam transport between the cavities. It is conceptually simplest to suppose transfer optics that image the reference plane of the gun exit successively at the mid planes of the two cavities. If the imaging condition is satisfied,

the transfer map that relates the particle transverse coordinates at the gun exit to the particle coordinate at a given cavity midplane is described by a single parameter, namely, the magnification factor M , $x \mapsto Mx$. Let M_1 and M_2 denote the magnification factors at each respective cavity, and let $E_{\max,1}^{\text{rf}}$ and $E_{\max,2}^{\text{rf}}$ be the two cavity amplitudes. It follows from Eqs. (4.11) and (4.18) that the difference in energy $\Delta\mathcal{E}$ between any particle and the reference particle, referred to the particle coordinates at the plane of the gun exit, splits into the two terms

$$\Delta\mathcal{E}(t, r) = \Delta\mathcal{E}(t) + \Delta\mathcal{E}(r), \quad (4.19)$$

where, ignoring terms in t_0 , x_0 and y_0 , as well as longitudinal drift,

$$\Delta\mathcal{E}(t) = \left[\frac{(eE_z^{\text{cat}})^2}{2m_e} + d_{\text{rf}}e \left(E_{\max,1}^{\text{rf}} - E_{\max,2}^{\text{rf}} \right) \frac{\omega^2}{2} \right] \Delta t^2, \quad (4.20)$$

$$\Delta\mathcal{E}(r) = \left[\frac{(eE_z^{\text{cat}})^2}{2m_e c^2 \mathcal{A}^2} - \frac{\pi^2 d_{\text{rf}} e}{\beta_*^2 \gamma_*^2 \lambda^2} \left(E_{\max,1}^{\text{rf}} M_1^2 - E_{\max,2}^{\text{rf}} M_2^2 \right) \right] r^2. \quad (4.21)$$

Again, β_* and γ_* are the values for a particle initially at rest. To optimize the cavities for monochromation, we set $\Delta\mathcal{E}(t)$ and $\Delta\mathcal{E}(r)$ to zero, yielding an under-constrained system of equations in the free variables $E_{\max,1,2}^{\text{rf}}$ and $M_{1,2}$. That the system is under constrained suggests the freedom to optimize a second design objective beyond energy spread. The most relevant second objective for microscopy applications is transverse emittance preservation, which we consider below in Sec. 4.6. Though under-constrained, Eq. (4.20) does predict the net energy added to the beam by the monochromator. The net energy added is a self-consistency test on the assumption that particle velocities remain approximately constant as they transit the cavities, which was made in deriving Eq. (4.21). The total energy gain of the beam is,

$$-ed_{\text{rf}} \left(E_{\max,1}^{\text{rf}} - E_{\max,2}^{\text{rf}} \right) = \frac{1}{4\pi^2} \frac{(eE_z^{\text{cat}} \lambda)^2}{m_e c^2}. \quad (4.22)$$

Given a 3 GHz cavity and an accelerating gradient of 1 MV/m, the total energy added is 500eV. This energy scale indicates that rf amplitude noise at the 10^{-5} level or larger makes a non-negligible contribution to the final energy spread.

Equation (4.20) ignores the uncertainty in emission time t_0 set by the laser pulse length and the photocathode response time Δt_l . A nonzero laser pulse length imposes another limit on the lowest achievable energy spread. If we take the laser pulse length into account then there is a linear correlation between emission time and energy in the final longitudinal distribution. The associated energy spread induced by nonzero emission time is,

$$\Delta\mathcal{E}(t_0) = d_{\text{rf}} e \left(E_{\text{max},1}^{\text{rf}} - E_{\text{max},2}^{\text{rf}} \right) \omega^2 \frac{p_{z0}}{eE_z^{\text{cat}}} t_0. \quad (4.23)$$

Substituting the expression for the net energy gain at the optimal cavity parameters into Eq. (4.22) yields

$$\Delta\mathcal{E}(t_0) = -\frac{eE_z^{\text{cat}}}{m_e} p_{z0} t_0. \quad (4.24)$$

Equation (4.24) shows that the final energy spread is bounded by the longitudinal emittance at the source, i.e., by the product of the spread in initial longitudinal momentum and time of emission. For the residual energy spread associated with non-zero initial transverse size $\Delta\mathcal{E}(r_0)$ to be of the same magnitude as or smaller than the residual $\Delta\mathcal{E}(t_0)$, the source transverse size must be on the scale of single microns, provided beam sizes in the cavities of ~ 100 microns. Source sizes for the highest brightness microscopy applications, both pulsed and continuous wave, are on the nanometer scale, and the simulation results presented in Sec. 4.4 E assume a nanometer-scale source. Thus, we can neglect $\Delta\mathcal{E}(r_0)$ in estimating the final energy spread. A subtle implication of Eq. (4.24) is then that, even for initial momenta with a statistical distribution in solid angle that spans

the whole forward hemisphere, only the marginal distribution over p_{z0} determines the final energy spread. Marginalising over solid angles tends to weight the marginal p_{z0} distribution toward $p_{z0} = 0$, reducing the final energy spread.

4.4.5 Simulation results

This section presents simulation results for four sets of initial beam conditions, to elucidate the beam dynamics and indicate the practical utility of our monochromator design. The first three sets are highly idealized and designed to isolate in turn the longitudinal and transverse degrees of freedom (Figs. 4.7 and 4.8), as well as the effects of cubic and higher-order nonlinear cavity fields on final energy spread (Fig. 4.9). The fourth set corresponds to realistic photoemission beam size and momentum spread and demonstrates monochromation from 1 eV to final energy spreads on the few meV scale (Fig. 4.10). The cases considered do not include the effects of timing jitter, which are accounted for in Sec. 4.5.

Our physics simulations are performed in General Particle Tracer (GPT) [220], a Runge-Kutta particle tracking code. Simulation beamline elements and field maps are shown in Figs. 4.3, 4.6. The GPT physics model does not include the photoemission process. Instead, our initial statistical distributions of particle transverse position, time and momenta are intended to replicate the results of photoemission, as summarized in Table 4.1. The physics of photoemission is an active area of theoretical and experimental research. We allow ourselves a margin of safety by assuming a larger initial spread of energies and emission times than has been experimentally demonstrated with cold photocathodes [125]. The

Dynamical variable	Distribution type
Time	Uniform
Energy	Uniform
Angle	Uniform
Position	Gaussian

Table 4.1: Initial particle distributions assumed in all simulations. Measures of spread for each variable in particular simulation runs are indicated in the main text and figures.

uncorrelated statistical uncertainty in our initial particle ensemble thus leads to poorer performance in simulations of our monochromator than would be expected with a more physically accurate treatment of photoemission.

Simulating quasi-one-dimensional initial beam conditions allows for easy graphical evaluation of the accuracy of Eqs. (4.20) and (4.21). The first set of initial conditions is designed to isolate the longitudinal phase space, having a source with vanishing transverse size, no transverse momentum and a laser pulse length of $\Delta t_\ell = 30$ fs. Figure 4.7(a) shows in blue a scatter plot of this beam in energy and time as it exits the gun. The simulated gun field map is a uniform gradient with a total accelerating voltage of 50 kV over a distance of 1 cm. The results in Fig 4.7(a) are in close agreement with Eq. (4.11), shown in the same figure as a white curve.

Figure 4.7(a) shows in red the final distribution of the same beam in energy and time after transiting a single cavity with amplitude chosen according to Eq. (4.20). Because the beam is quasi-one-dimensional, the second cavity is unnecessary. Inspection of the figure shows that the cavity removes the energy spread up to a small residual linear correlation apparent in the figure at negative arrival times. Equation (4.24) accurately predicts the coefficient of this linear correlation, shown in Fig 4.7(a) as a white line, confirming that the cavity

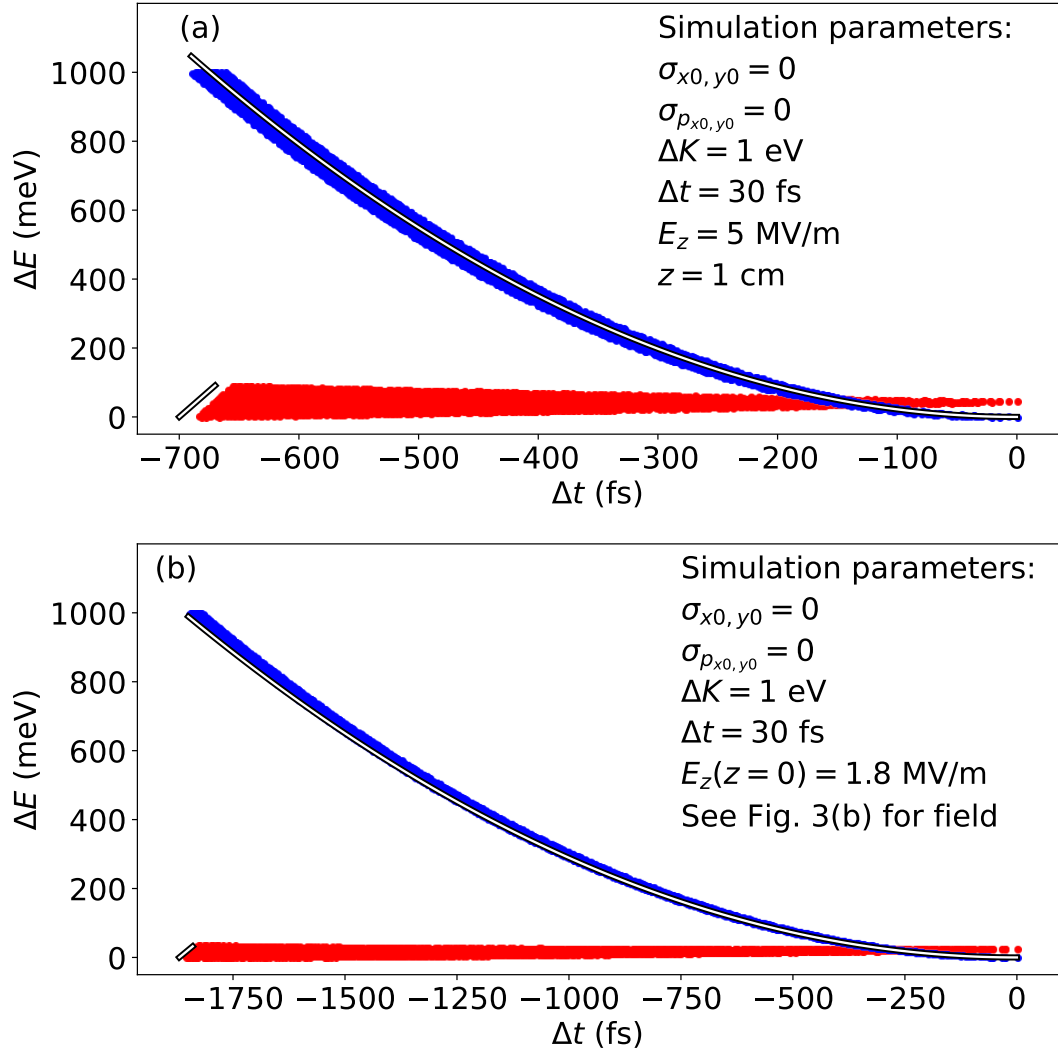


Figure 4.7: Simulation of a beam with $\Delta t_l = 30$ fs and only longitudinal momentum spread. Transverse size and momentum spread are set to zero. In (a), an idealized, uniform field gun is used. In (b), the realistic gun field shown in Fig. 4.3 is used. Blue points denote the energy-time correlation just after the gun. Red points show the result after transiting a single cavity with amplitude set by the solution of solution of Eq. (4.20). White lines are the predictions of Eq. (4.11) and Eq. (4.24), where in (b) we use the field at the cathode for E_z^{cat} .

restores the longitudinal emittance to its initial value.

Figure 4.7(b) shows results for the same quasi-one dimensional distribution as Fig. 4.7(a) but now accelerated in the non-uniform gun field map shown in Fig. 4.3(b). The field is nonuniform because of the electrode geometry, also shown in Fig. 4.3(b). The accelerating voltage is 50 kV over a distance of 1 cm. The field on the cathode is 1.8 MV/m, less than half the average gradient in the gun. The prediction of Eq. (4.11) is again shown by the white curve. In evaluating Eq. (4.11), E_z^{cat} is taken to be the field on the cathode. These results show that it is indeed the photocathode field, rather than the voltage or average gradient, which sets the final pulse length and the correlation between time of arrival and energy. The red curve shows the final energy time distribution after transiting a single cavity with amplitude chosen according to Eq. (4.20), again identifying the accelerating gradient with the field on the cathode.

The second set of initial conditions isolates the transverse direction. The beam at the source has nonzero size and transverse momentum spread but vanishing longitudinal momentum spread, so that all particles are emitted parallel to the photocathode surface. Figure 4.8 shows in blue the distribution of energy against radial displacement as this beam exits the gun. The prediction of Eq. (4.11) is shown as a white curve and again agreement is close. In this case, the gun field map is a uniform accelerating gradient, which simplifies the transverse focusing in the gun. A nonuniform accelerating field results in a lens effect that spoils the agreement between the transverse distribution and Eq. (4.11), but the qualitative picture is the same, with the energy depending quadratically on radial displacement. Figure 4.8 shows in red the beam after transiting a single cavity with amplitude chosen according to Eq. (4.21). Again, because the beam

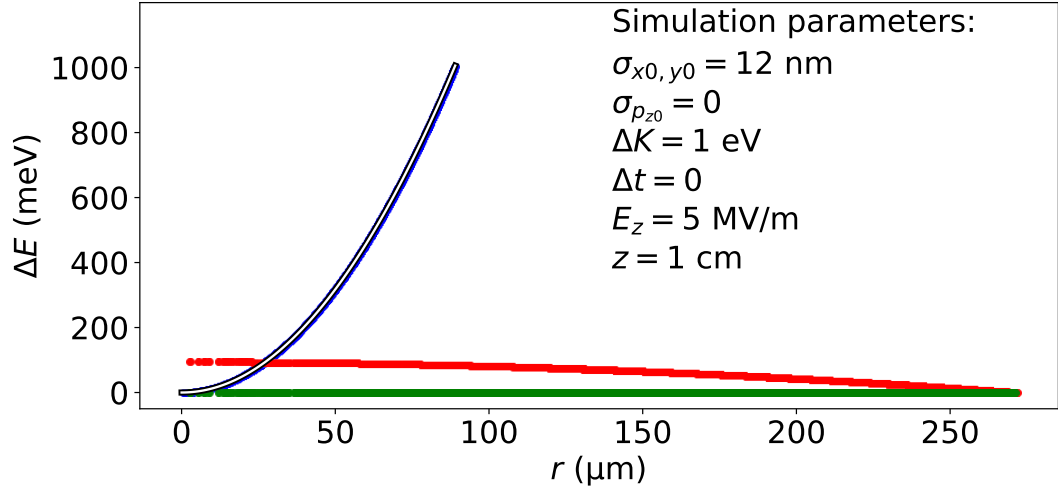


Figure 4.8: Simulation of a beam with initial size $\sigma_x = 12$ nm and nonzero transverse momentum spread. Here the beam has no longitudinal momentum spread and has zero duration. Blue points show the energy-space correlation just after the gun, and red points show the result after transiting a single cavity with amplitude set by Eq. (4.21). The white line is the prediction of Eq. (4.11). Due to thick lens effects, the cavity settings predicted by Eq. (4.21) slightly overcorrect the energy-space correlation. The green curve is the result of numerical optimization of the cavity amplitude.

is quasi-one-dimensional, the first cavity appearing in Eq. (4.21) is unnecessary. The magnification factor M_2 is set equal to the ratio of beam sizes at the gun exit and cavity midplane. Inspection of the red ensemble in Fig. 4.8 shows that a cavity with the analytically estimated settings overcorrects the energy-space correlation by 10%. Numerically optimizing the cavity amplitude then eliminates the overcorrection, as Fig. 4.8 shows in green.

Next, we simulate point source initial conditions with instantaneous emission, which isolates the evolution of correlated energy spread. The results of this simulation are presented in Fig. 4.9. The initial energy spread is 1 eV with

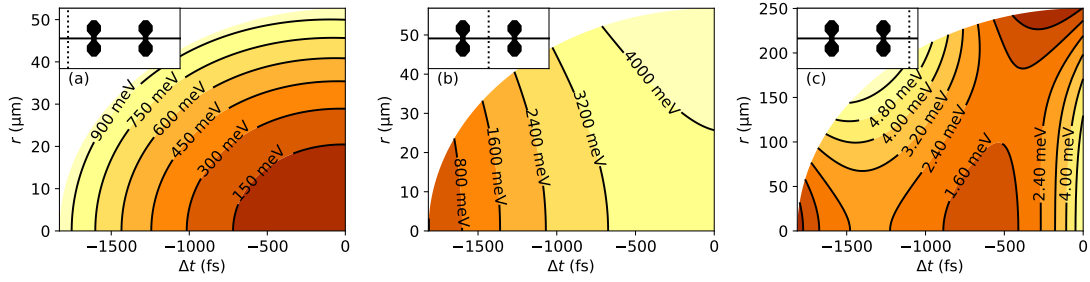


Figure 4.9: Simulated evolution of energy correlations on transiting two rf cavities, with an initial energy spread of 1 eV, vanishing initial transverse source size, and vanishing initial pulse length: (a) post gun but before the first cavity, the paraboloid distribution predicted by Eq. (4.11); (b) between the two cavities, the first cavity imparts a hyperboloid distribution as predicted by Eq. (4.18), with energy increasing in time and space; (c) after the second cavity, the residual energy spread involves cubic corrections to Eq. (4.11), shown in Eq. (4.12).

momenta uniformly distributed in solid angle over the forward hemisphere. The gun is modeled with the realistic fields shown in Figure 4.6(a). The cavity amplitude and phases are optimized numerically. Parameter values calculated from Eqs. (4.20) and (4.21) provide good initial guesses for the optimization algorithm and consistently overestimate the optimal cavity amplitudes, which likely arise from thick lens (nonimpulsive) effects, as evidenced by inspection of individual simulated particle tracks. The sequence of transformations presented in the three panels of Fig. 4.9 confirms qualitatively the analytic approximation in Eq. (4.18) for the work done by the cavities on the beam. Stepping through the panels, the initially paraboloid energy surface in Fig. 4.9(a) is transformed after transit through the first cavity into a hyperboloid in Fig. 4.9(b). Transit through the second cavity produces a surface of constant energy in Fig. 4.9(c), up to cubic corrections of order 10^{-3} the initial energy spread, a scale consistent with the expression for the leading cubic correction in Eq. (4.12).

Having tested the accuracy of our analytic model with idealized beam distributions, we present the results of simulations with realistic initial conditions. Figure. 4.3 shows gun electrode geometry, axial field profile and the layout of the remaining simulated beamline. The simulation beamline includes exactly one focusing solenoid downstream of the gun. A minimum of two such lenses is required to image the gun exit successively at the midplanes of each cavity, the transport we assume for the sake of convenience in deriving the analytic results of Sec. 4.4. Simulation results not reported here reveal that a two-solenoid design does not outperform a single-solenoid design. The simulation cavity field map is shown in Fig. 4.6. Figure 4.10 shows the final energy distribution obtained from simulating a source of 12 nm rms transverse radius and a uniform 1 eV energy spread distributed uniformly in solid angle over the forward hemisphere. The two curves in Fig 4.10 correspond to primary energies of 10 and 50 keV. The final full width at half maximum (FWHM) for both primary energies is 4 meV .

The evolution of energy spread as function of position down the simulated beamline is shown in Fig. 4.11(b), alongside pulse length in Fig. 4.11(c) and (d). Comparing Fig. 4.11(b) with Figs. 4.11(c) and (d), the final value of the product $\sigma_E \sigma_t$ is less than the initial value, in apparent contradiction with Eq. (4.1). The contribution the transverse momenta make to energy spread accounts for the discrepancy, with a significant fraction of the reduction in energy spread being made possible by expanding the transverse size of the beam. The ratio of final-to-initial transverse size is order 10^3 compared to the order 10 ratio of final-to-initial pulse lengths. A system of magnetostatic lenses can subsequently demagnify the beam without affecting energy spread and in the process further stretch the pulse length. For the initial conditions $\Delta K = 250$ meV shown in

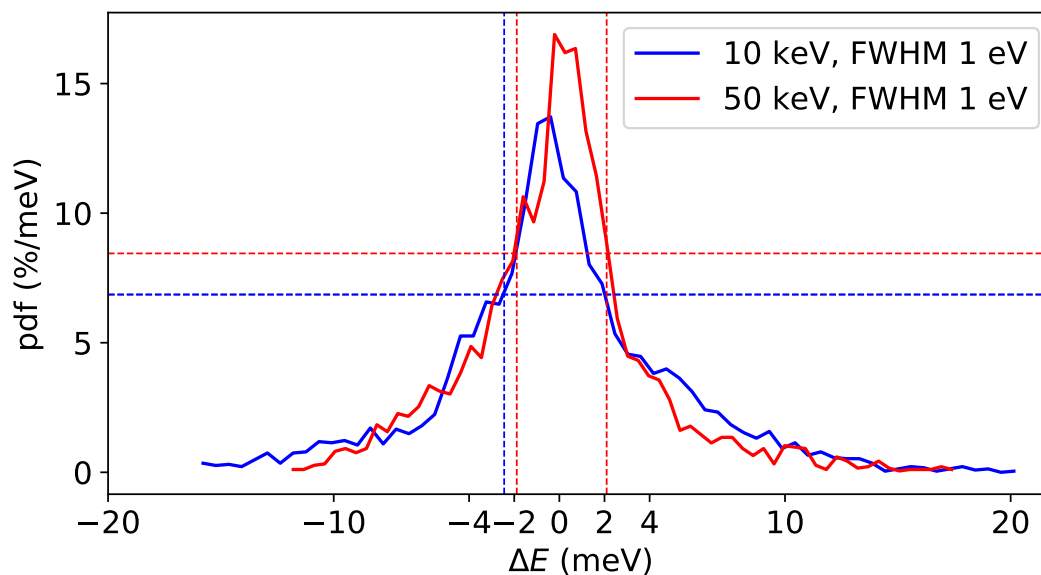


Figure 4.10: Results of simulating the beamline shown in Fig. 4.6(a). Particle ensembles initially have uniform energy spreads of 1 eV, distributed uniformly in solid angle over the forward hemisphere. Results for two accelerating voltages are shown, 10 kV (blue), 50 kV (red). Dashed horizontal and vertical lines indicate the FWHM.

Fig. 4.11, the final product $\sigma_\epsilon\sigma_t$ exceeds $\hbar/2$ by only 30%. Even as the quantum limit is approached, summary statistics calculated from classical particle tracking continue to describe the size of the beam envelope [221].

4.5 Jitter

Jitter in the phase of the cavities relative to the photoemitting laser pulse train contributes to the final energy spread. The study in [187] finds that the scale of phase jitter is set by thermal fluctuations in the length of the cavities. The fundamental frequency of the cavity varies with changes in the cavity length,

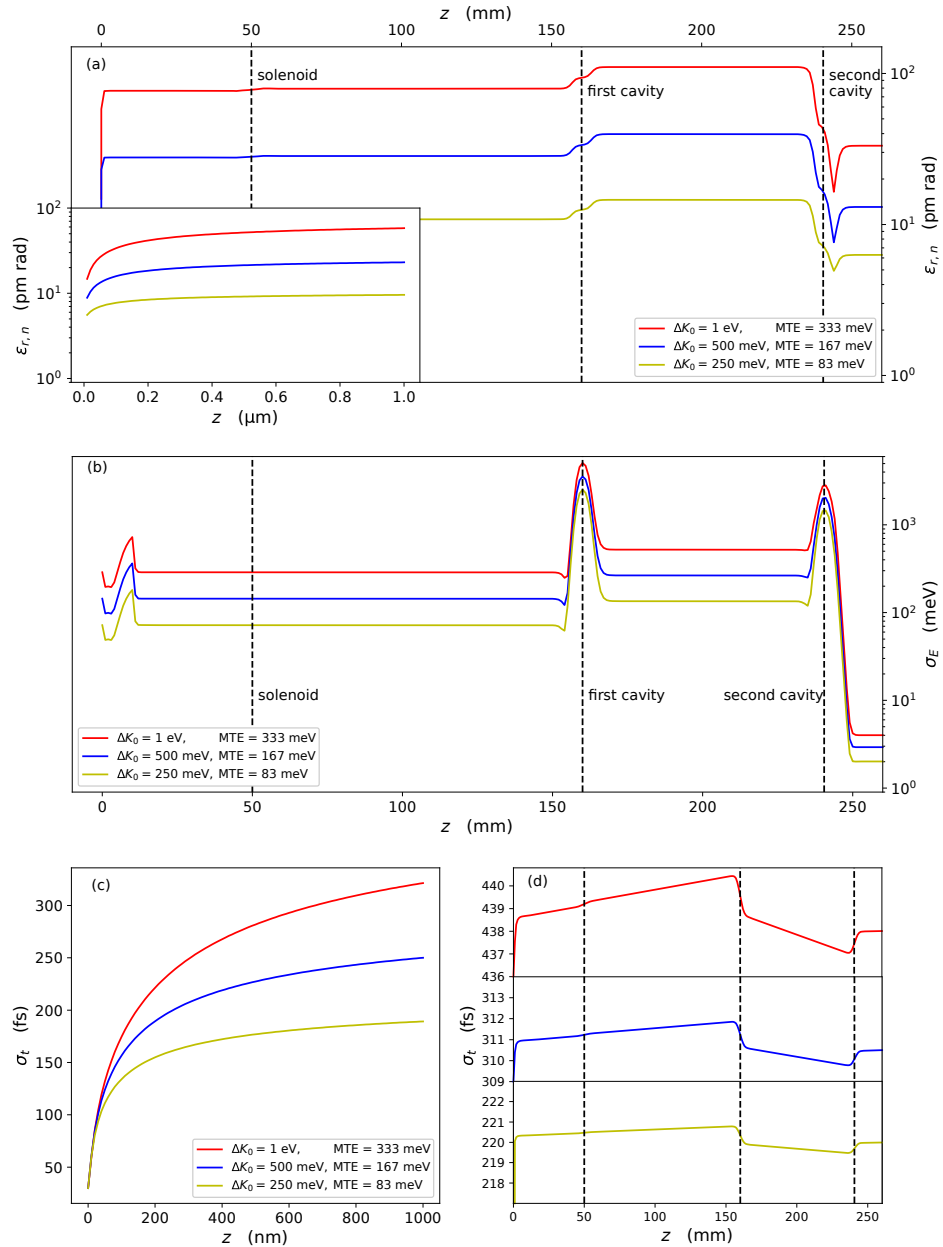


Figure 4.11: Simulation results showing beam sizes and emittance as a function of beamline position for three different initial energy spreads; all particle ensembles have initial transverse size of 12 nm rms and momenta distributed uniformly over the forward hemisphere; with initial uniform energy spreads of 1 eV (red), 500 meV (blue), and 250 meV (yellow). Cavity settings are chosen to achieve the smallest final energy spread. (a) Transverse normalized emittance; (b) rms energy spread; (c), (d) rms pulse duration.

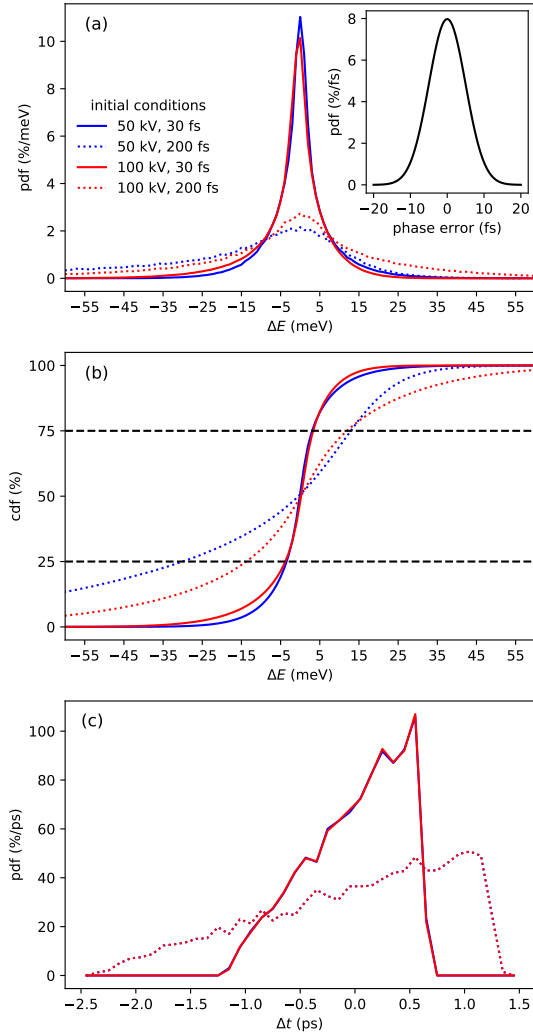


Figure 4.12: Simulated energy distribution in the presence of white rf phase noise at the same 5 fs rms scale reported experimentally in [145]. Four sets of initial conditions are shown, with initial energy spreads of 1 eV in all. Colors indicate two sets of primary energies: 50 keV (blue), 100 keV (red). Line style indicates the initial pulse length; 30 fs (solid line), 200 fs (dotted line). (a) Probability density per meV downstream of the rf monochromator. Inset shows the distribution of the timing noise in the simulation, with the noise identically and independently distributed in each cavity. (b) Cumulative probability density with dashed horizontal lines indicating interquartile range. (c) Probability of time of arrival per picosecond relative to the mean, downstream of the gun.

thereby shifting the phase difference between the driving oscillator and cavity response. In terms of a change in temperature ΔT , the change in phase $\Delta\phi$ is [187],

$$\Delta\phi = -2Q\kappa_T\Delta T, \quad (4.25)$$

where Q is the unloaded quality factor of the resonator, typically 10^4 for a normal conducting copper cavity, and κ_T is the coefficient of thermal expansion, $1.64 \times 10^{-5} \text{ K}^{-1}$ for copper. At a temperature stability of 1 mK, the uncertainty in phase is $\Delta\phi = 3.3 \times 10^{-4}$, or 17 fs at 3 GHz.

A phased locked loop was experimentally shown in [145] to reduce the rms phase noise of a bunching cavity to 5 fs when averaged over a 16 hour time series, and to eliminate long-term phase drift. Figure 4.12 shows the simulated broadening of the zero-loss peaks (ZLP) due to phase jitter for four sets of initial conditions when the phase correction scheme of [145] is implemented. The simulations add to the phase of each cavity independent 5 fs rms Gaussian white noise. The assumption of white noise is a simplification with respect to the $1/f$ noise typically encountered in electron microscopy. Our white noise model therefore significantly overestimates the size of phase fluctuations on time periods of 100 ms or less that are typical for EELS acquisition.

The solid blue lines in Fig. 4.12 correspond to a primary energy of 50 keV, a 1 eV energy spread, and an initial pulse length of 30 fs. Figure 4.12(a) shows a FWHM of 5 meV, a broadening of 1 meV compared to the jitter-free result shown in Fig. 4.10. The impact of tails in the ZLP is more easily visualized in a plot of the cumulative energy distribution downstream of the monochromator, shown in Fig. 4.12(b), which reveals that 50 % of particles lie in a 6 meV bandwidth. Figure 4.12(c) shows the spread of arrival times at the monochromator

exit, the trade-off imposed by narrowing the energy spread. The solid red lines in Fig. 4.12 correspond to a primary energy of 100 keV, a 1 eV energy spread and an initial pulse length of 30 fs. The greater primary energy is achieved by lengthening the gun field map shown in Fig. 4.3, leaving the field strength on the cathode unchanged. Comparison of the solid blue and red lines show that the change in primary energy has little effect on the energy resolution and final pulse length.

The dotted blue and red lines in Fig. 4.12 correspond to 200 fs initial pulse length and 1 eV initial energy spread. Dotted blue lines correspond to a primary energy of 50 keV and dotted red lines to 100 keV. A primary energy of 100 keV and pulse length of 200 fs is typical for ultrafast electron microscopy with field emission electron sources. The value 200 fs is representative because it approaches the bandwidth limit of Yb gain media, which are commonly chosen for high power, higher repetition rate lasers. Established techniques for increasing bandwidth allow a 200 fs pulse to be compressed to the 10 fs scale [222]. A greater uncertainty in emission time demands a compensating reduction in the field strength on the cathode, here to 1 MV/m, performed in the simulation by scaling the dimensions of the gun-field map shown in Fig. 4.3. The dotted red line in Fig. 4.12(a) shows a 22 meV FWHM, and the dotted red line in Fig. 4.12(b) shows that 50% of particles lie in a 26 meV bandwidth. The spread of arrival times downstream of the gun, shown as a dotted red line in Fig. 4.12(c), is 3 ps. The energy width figures for the 200 fs initial pulse are five times worse than for the 30 fs length. To improve the resolution of the 200 fs pulse to the same level as the 30 fs pulse would require stretching the final pulse length a further factor five, or 5% of the 3 GHz cavity period. At a duty cycle of 5%, the problem of optimizing cavity parameters goes beyond the quadratic approximations made

in Sec. 4.4, and thus we do not explore this regime in the simulation.

The time-averaged uncorrelated energy spread introduced by phase fluctuations follows by expanding the sinusoidal time dependence of the work done by the cavities,

$$\Delta\mathcal{E} = -ed_{\text{rf}} \left(E_{\text{max},1}^{\text{rf}} + E_{\text{max},2}^{\text{rf}} \right) \left(\frac{1}{2} \Delta\phi^2 - \frac{\omega\sigma_{p_{z0}}}{eE_z^{\text{cat}}} \Delta\phi \right), \quad (4.26)$$

with $\sigma_{p_{z0}}$ the spread in initial longitudinal momenta. The factor containing p_{z0} is the estimate of pulse length obtained from Eq. (4.5). For particles arriving earlier than average, the linear term in $\Delta\phi$ dominates because pulses are 100 fs to single picoseconds long for accelerating gradients below 10 MV/m at an initial energy spread of 1 eV or more. However, the statistical distribution peaks at late arrival times, if the particle ensemble has an initially uniform distribution in energy. For particles near this peak, the term quadratic in $\Delta\phi$ dominates the right-hand side of Eq. (4.26). The takeaway from Eq. (4.26) is thus that phase fluctuations move the tails of the energy distribution much more than they do the location of the peak, by a factor 10 to 100.

At 1 mK temperature stability in the absence of rf phase correction, Eq. (4.26) predicts a broadening near the peak of the probability distribution of less than one meV and a broadening in the tails of tens of meV. The prefactor in Eq. (4.26) is 7 keV for our simulation example of a 50 kV gun with nonuniform gradient shown in Fig. 4.6, and 1 keV for the 10 kV example. These estimates are confirmed in the simulation, as shown in Fig. 4.13. The simulations cycle through a range of phase offsets $\Delta\phi_1, \Delta\phi_2$, one independent offset for each of the two cavities. For each pair of phase offsets, the right panel of Fig. 4.13 shows a scatter plot in arrival time and the final energy of particles in the beam. Comparison of the scatter plots supports our interpretation of Eq. (4.26), indicating in particu-

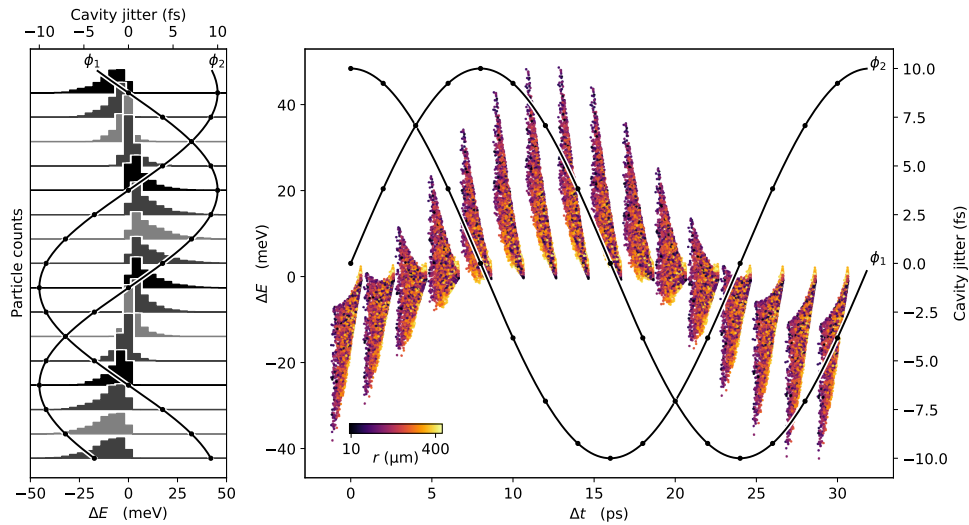


Figure 4.13: Simulations of cavity timing jitter. The initial particle ensemble has a uniform 1 eV energy spread distributed uniformly in solid angle over the forward hemisphere. Plots show the ensemble after transiting two 3 GHz cavities with timing offset from the optimal solution by ϕ_1, ϕ_2 respectively. Offsets add in quadrature to 10 fs. At left, histograms of final energy show single meV movement in peak location and 10 meV scale movement in tails. On the right, energy-time correlation are shown as a function of cavity phase, where different phases are offset on the time axis for clarity.

lar that the jitter-induced movement in the tails of the final energy distribution is due to early arriving particles. The left panel of Fig. 4.13 shows the corresponding sequence of final energy histograms. On inspection, the jittery peak locations remain within order 1 meV the nominal peak location at $\Delta\mathcal{E} = 0$.

Comparatively slow fluctuations in the gun voltage are uncorrelated with differences in time of arrival between successive pulses at the relevant order of precision, according to Eq. (4.3). Energy spread due to these fluctuations is therefore not removed by our rf monochromator design. One strategy for eliminating this sub-leading source of energy spread is to implement a feedback

loop, such as is included in the magnetic prism monochromator design [206]. Our implementation would place an energy selector downstream of the cavities with a slit width chosen so that all particles are accepted at the nominal accelerating voltage. As the accelerating voltage changes, particles clipping the slit edge trigger the feedback mechanism to change the gun high-voltage set point.

4.6 Brightness conservation

To achieve maximum gains in average current, our design must omit transverse collimation. The ensemble of particles transported to the experimental target consequently includes large excursions from the optical axis, which are typically ignored in electron-microscope design. Brightness averaged over all emission angles and positions is therefore the more informative figure of merit for our unconventional beam, rather than the peak brightness more commonly encountered in a microscopy context. Our preferred figure of merit is the phase space area occupied by the beam, which is inversely proportional to the square root of the brightness. The most general measure of phase space area is *normalized transverse emittance*, defined as:

$$\epsilon_{nx} = \frac{1}{m_e c} \sqrt{\langle x^2 \rangle \langle p_x^2 \rangle - \langle x p_x \rangle^2}. \quad (4.27)$$

Minimum physically achievable emittance corresponds to a normalized emittance equal to half the reduced Compton wavelength of the electron. At the source, the cross term in x and p_x drops out of Eq. (4.27) and it is convenient to define a new quantity, the *mean transverse energy* (MTE):

$$\text{MTE} = \frac{\langle p_x^2 \rangle}{m_e}. \quad (4.28)$$

For a statistical distribution that is uniform in energy and uniformly distributed in solid angle over the forward hemisphere, the MTE is equal to 2/3 the mean energy. Letting σ_{x0} be the rms source size, the source emittance is then,

$$\epsilon_{nx}(z = 0) = \sigma_{x0} \sqrt{\frac{\text{MTE}}{m_e c^2}}. \quad (4.29)$$

Our simulations show significant emittance degradation occurring just after emission for nanometer-sized sources with energy spreads on the 100 meV scale. Surprisingly, we find that the action of the monochromator largely undoes this emittance growth. The emittance growth we observe can be understood as the contribution of the uniform accelerating field to the spherical and chromatic aberration of the optical column [216], which amounts to a series expansion of the emittance around a vanishing solid angle. However, since our design is unlike a conventional microscope, this section explicitly derives time-of-arrival dependent expressions for the emittance growth valid at all emission angles. These expressions then predict that, up to the accuracy of the analytical model of energy-equalization presented in Sec. 4.4, the final emittance after transiting the monochromator cavities is equal to the source emittance. Simulation results reported in Fig. 4.11 show that, beyond the rigid-beam approximation, parameters optimised for energy spread reduction overcorrect the emittance loss, imparting to the beam a correlation between time of arrival and divergence that is opposite in sign to the gun.

During acceleration of a pulsed beam, correlations evolve between time of arrival and beam divergence, so that projecting onto the transverse phase space results in brightness loss. Starting from the solution to the equations of motion

in x for a uniform accelerating field, the transverse emittance at proper time τ is,

$$\epsilon_{n,x}^2 = \frac{\langle x_0^2 \rangle \langle p_{x0}^2 \rangle}{m_e^2 c^2} + \frac{\langle p_{x0}^2 \rangle \langle p_{x0}^2 \tau^2 \rangle}{m_e^4 c^2} - \frac{\langle p_{x0}^2 \tau \rangle^2}{m_e^4 c^2}. \quad (4.30)$$

The simplest physically plausible picture of emission from a flat cathode is that the initial momenta are uniformly distributed in solid angle over the forward hemisphere, implying a correlation between p_{x0} and p_{z0} , and hence between p_{x0} and τ . These correlations are better disentangled by going over to polar coordinates,

$$p_{x0} = p_0 \sin \phi \cos \theta, \quad (4.31)$$

$$p_{z0} = p_0 \cos \theta, \quad (4.32)$$

and assuming that the momentum magnitude p is uncorrelated with the emission angles ϕ, θ . Letting the probability of emission be uniform in azimuth ϕ , expanding τ to first order in Δt per Eq. (4.9), and substituting the expression for Δt in terms of Δp_{z0} given by Eq. (4.5), the result is that Eq. (4.30) becomes

$$\epsilon_{n,x}^2 = \frac{\langle \beta_0^2 \rangle}{3} (\langle x_0^2 \rangle + \sigma_{x0*}^2), \quad (4.33)$$

with

$$\sigma_{x0*}^2 = \frac{m_e^2 c^4}{e^2 E_z^2} \left(\frac{1}{15} \langle \beta_0^4 \rangle - \frac{3}{64} \frac{\langle \beta_0^3 \rangle^2}{\langle \beta_0^2 \rangle} \right). \quad (4.34)$$

where, again, E_z is the longitudinal field in the gun. The term σ_{x0*}^2 is a new, critical feature of near-cathode dynamics for nanometer-scale photoemission sources: an effective source size growth arising from photoemission momentum spread. The scaling of this effective source size with mean transverse energy has practical importance for active research toward higher brightness photocathodes. Assuming a uniform distribution in energy at the source, Eq. (4.34) simplifies to,

$$\sigma_{x0*} = 0.363 \times \frac{\langle \text{MTE} \rangle}{|eE_z|}. \quad (4.35)$$

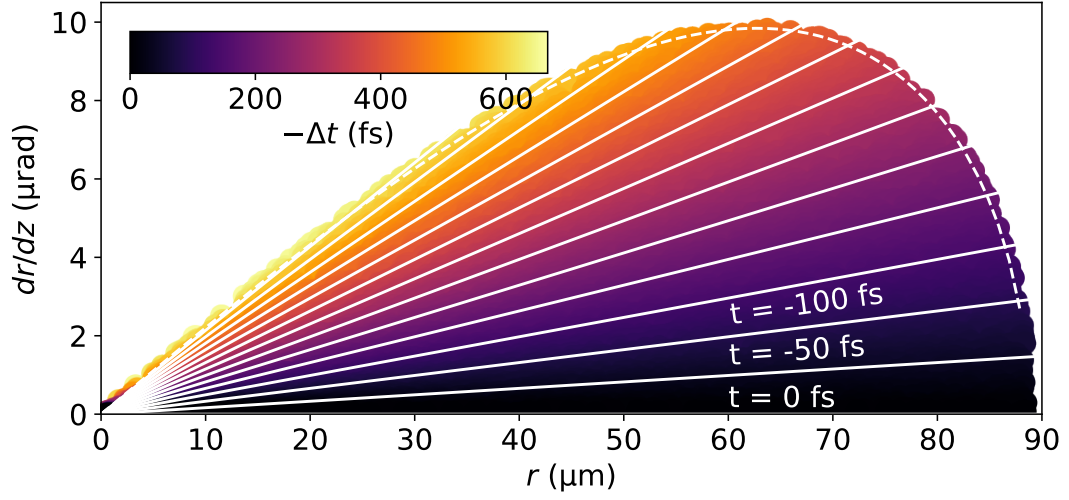


Figure 4.14: Correlations between particle divergence and time of arrival in particle tracking simulations of a uniform accelerating gradient of 5 MV/m. The initial conditions of the particle distribution are a 1 eV uniform energy spread distributed uniformly in solid angle over the forward hemisphere, and vanishing transverse size and pulse length. The time-dependent divergence predicted by Eq. (4.37) are shown by the white lines at constant time increments of 50 fs.

Thus, for nano-scale sources, photocathode emittance goes like $MTE^{3/2}$ and not the expected $MTE^{1/2}$, enhancing the potential impact of new low MTE materials on the future performance of photoemitters [24].

To see that the emittance growth expressed in Eq. (4.33) can be undone by a time-dependent lens, we invert the solution to the equations of motion in x and expand τ to obtain the following expression for the particle angle dx/dz as a function of Δt ,

$$\frac{p_x}{p_z} = \frac{m_e(x - x_0)}{p_{z*}\tau_*} - \frac{m_e(x - x_0)}{p_{z*}\tau_*^2} \Delta t. \quad (4.36)$$

The term in Eq. (4.36) proportional to Δt is the same as the expression for the change in angle imparted by an ideal thin lens with time-dependent focal

length,

$$f_{\text{gun}}^{-1} = \frac{(eE_z^{\text{cat}})^2 \Delta t}{\gamma_* \beta_* m_e^2 c^3 \mathcal{A}^2}. \quad (4.37)$$

Equation (4.37) is not meant to be an explanation of the cause of the emittance growth in the gun. Instead, Eq. (4.37) makes the linear correlation with time of arrival explicit in a manner that serves to explain how the time-dependent focusing power of an rf cavity is able to counteract the emittance growth in the gun.

Simulation results verifying Eq. (4.37) are shown in Fig. 4.14. To produce the plot, the beam divergence of the time-independent term in Eq. (4.36) is subtracted. Figure 4.14 overlays the divergence predicted by Eq. (4.37) as white lines at fixed increments in time of arrival. A color scale indicates the simulation time of arrival. The curved beam envelope, indicated by a dashed white line in Fig. 4.14, is derivable from Equation (4.37) by expressing divergence as a function of initial kinetic energy:

$$\frac{p_x}{p_z}(K, x) = \frac{-eE_z^{\text{cat}} x}{\gamma_* \beta_* \mathcal{A}^2} \sqrt{\frac{2K}{m_e^3 c^6} - \frac{e^2 E_z^{\text{cat}2} x^2}{m_e^4 c^8 \mathcal{A}^2}}. \quad (4.38)$$

The envelope is found by holding K at a constant value equal to the maximum initial kinetic in the particle ensemble: 1 eV for Fig. 4.14. Comparing Eq. (4.38) and Eq. (4.37) clarifies an unexpected advantage of time-dependent focusing fields: explicit control in the time domain makes linear an effect that appears nonlinear in the transverse phase space.

The transverse focusing power of a cavity, calculated by making the same thin-lens approximation assumed in the derivation of Eq. (4.18), is [187],

$$f_{1,2}^{-1} = \mp \frac{eE_{\text{max},1,2}^{\text{rf}} d_{\text{rf}}}{2\gamma_*^3 \beta_*^3 m_e c^3} \omega^2 \Delta t, \quad (4.39)$$

where the cavity phase is taken to maximize (in magnitude) the reference particle.

If the gun exit is successively imaged at the midplanes of the two cavities, with magnification factors M_1 and M_2 , then the condition for cancellation of the emittance growth is,

$$\frac{1}{f_{\text{gun}}} + \frac{M_1^2}{f_1} + \frac{M_2^2}{f_2} = 0. \quad (4.40)$$

The derivation of Eq. (4.40) assumes the pulse length remains constant after exiting the gun, a good approximation for the compact beamline shown in Fig. 4.6(a). Substituting the expressions in Eqs. (4.37) and (4.39) into Eq. (4.40) gives a third equation on the system of monochromator parameters $E_{\text{max},1}^{\text{rf}}, M_1, E_{\text{max},2}^{\text{rf}}, M_2$,

$$ed_{\text{rf}}E_{\text{max},1}^{\text{rf}}M_1^2 - ed_{\text{rf}}E_{\text{max},2}^{\text{rf}}M_2^2 = \frac{(eE_z^{\text{cat}}\lambda)^2}{2\pi^2} \frac{\gamma_*^2\beta_*^2}{m_e c^2 \mathcal{A}^2}, \quad (4.41)$$

where \mathcal{A} is again the aspect ratio defined in Eq. (4.10). Equation (4.41) is equivalent to the equation obtained by setting the energy spread to zero in Eq. (4.21).

Simulation results presented in Fig. 4.11 show that cavity parameters optimal for reducing energy spread actually overcorrect the brightness loss in the gun. Simulated particle tracks show that this overcorrection is due to particles not obeying the rigid-beam approximation made in deriving Eq. (4.21). Thus, there is a trade-off between energy spread reduction and brightness conservation in a scheme involving only two cavities. Simulations show that, at the cost of reintroducing energy spread at the 10^{-1} level compared to the source, reducing the second cavity amplitude does perfectly restore the source emittance. Figure 4.11 shows simulation results for three values of the source energy spread: uniform distributions over 1 eV, 500 meV and 100 meV. The trend in energy reveals that at 250 meV and below, the excess final emittance at the min-

imum achievable final energy spread exceeds the source emittance by less than 30%.

4.7 Discussion and conclusion

This paper has shown in simulation the feasibility of a high-energy resolution, pulsed electron source design. The design utilizes radiofrequency accelerating cavities to top-off the primary energy delivered by a dc gun. Relying on correlations between energy on the one hand and time and position of arrival at the cavities on the other, the additional cavity acceleration equalizes energies in the particle ensemble. An initial energy spread of 1 eV is reduced in simulation to 4 meV at primary energies of 10 kV and 50 kV assuming arbitrary precision in cavity timing. Simulating the effect of cavity jitter at 5 fs timing precision shows the peak of the energy distribution broadening on the single meV scale. The efficacy of the design is explicable by simple yet accurate analytic expressions, strongly suggesting that our results are not sensitive to peculiar choices of simulation parameters and that the scheme could be realized experimentally with presently available technology.

A near at hand application of our design is to install two rf cavities in an existing ultrafast electron transmission microscope. Existing UEM instruments photoemit from nanometer-scale tips, where significant field enhancement occurs. Typical gradients are 1 GeV/m at nanometer distances. The importance of field enhancement for our scheme is that the rapid acceleration of particles escaping the field-enhanced region implies a shorter final pulse length and hence a larger final energy spread, following Eq. (4.1). Strategies to compensate for

this unwanted side effect of field enhancement include: reducing the extraction voltage, increasing the tip radius, and introducing an extended drift space immediately following extraction.

Our results readily extend to monochromation at primary energies of hundreds of keV. At higher primary energies, the rigid-beam approximation made in our analytic treatment of the cavities becomes more accurate. Conversely, the rigid beam approximation breaks down as the primary energy approaches zero. The error in the approximation becomes significant when the transit time through a single cavity is comparable to the cavity period. For a 3 GHz cavity with a 1 cm gap, the ratio of transit time to rf period is unity at a primary energy of 2.6 keV. Exploring cavity monochromation at primary energies below 3 keV thus requires a nonimpulsive treatment of the work done by the cavities.

This paper also investigated, analytically and numerically, the effect of the rf cavities on transverse brightness. Fortuitously, time-dependent cavity lensing undoes brightness loss in the gun. Effects apparent in simulation that go beyond the impulsive approximation made in our analytic treatment result in the cavities overcorrecting the brightness loss. Simulations show that the overcorrection becomes negligible at source energy spreads of 250 meV and below, a finding that underscores the importance for future electron-beam technologies of ongoing research into photocathode materials with low intrinsic energy spreads [24].

4.8 Acknowledgements

We thank J. P. Gonzalez Aguilera for help with particle tracking simulations. This research was supported by the Center for Bright Beams, U.S. National Science Foundation Grant No. PHY-1549132.

4.9 Appendix A: Cavity field expansion

The derivation of the field expansion shown in Eq. (4.14) proceeds by the method of Frobenius. The assumption of harmonic time dependence simplifies the wave equation to the condition that,

$$\left(\nabla^2 + \frac{\omega^2}{c^2}\right) \sum_{n=0}^{\infty} \sum_{m=0}^{\infty} \sum_{q=0}^{\infty} a_{nmq} r^n \frac{\omega^m}{c^m} \frac{d^q}{dz^q} E_{0,z}^{\text{rf}}(z) = 0, \quad (4.42)$$

in the unknown coefficients a_{nmq} . The special case in which $\omega = 0$ is commonly treated in textbooks on electron optics; see, e.g., [223]. Computing the action of the differential operator term by term, Eq. (4.42) leads to,

$$\sum_{n=0}^{\infty} \sum_{m=0}^{\infty} \sum_{q=0}^{\infty} a_{nmq} \left(n^2 r^{n-2} \frac{\omega^m}{c^m} \frac{d^q}{dz^q} + r^n \frac{\omega^{m+2}}{c^{m+2}} \frac{d^q}{dz^q} + r^n \frac{\omega^m}{c^m} \frac{d^{q+2}}{dz^{q+2}} \right) E_{0,z}^{\text{rf}}(z) = 0. \quad (4.43)$$

Since Eq. (4.43) must hold for arbitrary ω and $E_{0,z}^{\text{rf}}(z)$, the left-hand side vanishes order by order in r, ω and d/dz . The implied recursion relation that the a_{nmq} satisfy is therefore,

$$n^2 a_{n,m,q} + a_{n-2,m-2,q} + a_{n-2,m,q-2} = 0, \quad (4.44)$$

subject to the boundary conditions that $a_{0,0,0} = 1$ and that the coefficients for negative powers of r vanish. These boundary conditions are necessary and jointly

sufficient for the field at $r = 0$ to coincide with $E_{0,z}^{\text{rf}}(z)$. Let us state and then verify that the solution to Eq. (4.44) is,

$$a_{2n,2m,2q} = \left(\frac{-1}{4}\right)^n \frac{1}{n!m!q!} \quad \text{if } n = m + q, \quad (4.45)$$

with all remaining coefficients vanishing. To verify, substituting the right-hand side of Eq. (4.45) into the left-hand side of Eq. (4.44) gives,

$$\left(\frac{-1}{4}\right)^n \frac{1}{n!m!q!} [4n^2 - 4nm - 4nq] = 0. \quad (4.46)$$

The second and third terms inside the square brackets on the left hand side of Eq. (4.46) follow from the property of factorials that $(n-1)! = n!/n$. Equation (4.46) holds if and only if $n = m + q$; hence, we have solved the recursion relation expressed in Eq. (4.44). Using the constraint $n = m + q$, the solution can be simplified to

$$a_{2n,2k,2(n-k)} = \left(\frac{-1}{4}\right)^n \frac{1}{(n!)^2} \binom{n}{k}. \quad (4.47)$$

The appearance of the binomial coefficient in the simplified solution then implies that the contributions from ω and d/dz sum to give

$$\begin{aligned} & \sum_{n=0}^{\infty} \sum_{m=0}^{\infty} \sum_{q=0}^{\infty} a_{nmq} r^n \frac{\omega^m}{c^m} \frac{d^q}{dz^q} \\ &= \sum_{n=0}^{\infty} \left(\frac{-1}{4}\right)^n \frac{r^{2n}}{(n!)^2} \sum_{k=0}^n \binom{n}{k} \frac{\omega^{2k}}{c^{2k}} \frac{d^{2(n-k)}}{dz^{2(n-k)}} \end{aligned} \quad (4.48)$$

$$= \sum_{k=0}^{\infty} \left(\frac{-1}{4}\right)^k \frac{r^{2k}}{(k!)^2} \left(\frac{d^2}{dz^2} + \frac{\omega^2}{c^2}\right)^k. \quad (4.49)$$

The coefficients $(-1/4)^k/(k!)^2$ appearing on the right-hand side of Eq. (4.48) are the power series expansion of the zeroth-order Bessel function of the first kind, from which Eq. (4.14) in the main text immediately follows.

4.10 Appendix B: Integration by parts

To perform the integration by parts, we need to derive an intermediate result, namely,

$$\int_{-\infty}^{\infty} \frac{d^{2n} f(x)}{dx^{2n}} \cos(kx) dx = (-1)^n k^{2n} \int_{-\infty}^{\infty} f(x) \cos(kx) dx, \quad (4.50)$$

for arbitrary $f(x)$ satisfying, for all n ,

$$\lim_{x \rightarrow \pm\infty} \frac{d^n f}{dx^n} = 0. \quad (4.51)$$

The derivation is by mathematical induction. The base case, $n = 0$, is trivially true. Now assume that Eq. (4.50) holds for arbitrary n . It then follows, integrating by parts twice, that Eq. (4.50) also holds for $n + 1$:

$$\begin{aligned} & \int_{-\infty}^{\infty} \frac{d^{2n+2} f(x)}{dx^{2n+2}} \cos(kx) dx \\ &= \left[\frac{d^{2n+1} f(x)}{dx^{2n+1}} \cos(kx) \right]_{-\infty}^{\infty} + k \int_{-\infty}^{\infty} \frac{d^{2n+1} f(x)}{dx^{2n+1}} \sin(kx) dx \end{aligned} \quad (4.52)$$

$$= k \int_{-\infty}^{\infty} \frac{d^{2n+1} f(x)}{dx^{2n+1}} \sin(kx) dx \quad (4.53)$$

$$= \left[\frac{d^{2n} f(x)}{dx^{2n}} \sin(kx) \right]_{-\infty}^{\infty} - k^2 \int_{-\infty}^{\infty} \frac{d^{2n} f(x)}{dx^{2n}} \cos(kx) dx, \quad (4.54)$$

where the terms in square brackets vanish, following Eq. (4.51). Applying the inductive hypothesis to the integral on the right-hand side of Eq. (4.54), yields

$$\begin{aligned} & \int_{-\infty}^{\infty} \frac{d^{2n+2} f(x)}{dx^{2n+2}} \cos(kx) dx \\ &= (-1)^{n+1} k^{2n+2} \int_{-\infty}^{\infty} f(x) \cos(kx) dx, \end{aligned} \quad (4.55)$$

completing the demonstration of Eq. (4.50).

Making use of Eq. (4.50) to more perform explicitly the calculation in the

main text:

$$W(r, t) = - \int_{-\infty}^{\infty} e \mathbf{E} \cdot d\mathbf{s} \approx - \int_{-\infty}^{\infty} e E_z(t(z), z, r) dz \quad (4.56)$$

$$\begin{aligned} &= -e \sum_{n=0}^{\infty} \sum_{k=0}^{\infty} \left(\frac{-1}{4} \right)^n \frac{r^{2n}}{(n!)^2} \frac{\omega^{2(n-k)}}{c^{2(n-k)}} \binom{n}{k} \\ &\times \int_{-\infty}^{\infty} \frac{d^{2k}}{dz^{2k}} E_{z,0}^{\text{rf}}(z) \cos \left(\frac{2\pi z}{\beta \lambda} + \omega \Delta t + \phi_0 \right) dz, \end{aligned} \quad (4.57)$$

where Δt is the difference in times of arrival of the given particle and the reference particle. The cosine function expands as,

$$\begin{aligned} \cos \left(\frac{2\pi z}{\beta \lambda} + \omega \Delta t + \phi_0 \right) &= \cos \left(\frac{2\pi z}{\beta \lambda} \right) \cos (\omega \Delta t + \phi_0) \\ &\quad - \sin \left(\frac{2\pi z}{\beta \lambda} \right) \sin (\omega \Delta t + \phi_0). \end{aligned} \quad (4.58)$$

The integral over the factor in the sine of z vanishes because sine is an odd function. Hence, the expression on the right-hand side of Eq. (4.57) further simplifies to,

$$\begin{aligned} W(r, t) &= -e \cos(\omega \Delta t + \phi_0) \int_{-\infty}^{\infty} E_{z,0}^{\text{rf}}(z) \cos \left(\frac{2\pi z}{\beta \lambda} \right) dz \\ &\times \sum_{n=0}^{\infty} \sum_{k=0}^{\infty} \left(\frac{-1}{4} \right)^n \frac{r^{2n}}{(n!)^2} \frac{\omega^{2(n-k)}}{c^{2(n-k)}} \binom{n}{k} \left(\frac{2\pi i}{\beta \lambda} \right)^{2k}. \end{aligned} \quad (4.59)$$

The imaginary unit appearing in Eq. (4.59) simplifies the prefactor $(-1)^k$, which the integration by parts contributed. Summing over k ,

$$\begin{aligned} &\sum_{k=0}^{\infty} \frac{\omega^{2(n-k)}}{c^{2(n-k)}} \binom{n}{k} \left(\frac{2\pi i}{\beta \lambda} \right)^{2k} \\ &= \sum_{k=0}^{\infty} \frac{\omega^{2n}}{c^{2n}} \binom{n}{k} \left(\frac{i}{\beta} \right)^{2k} \end{aligned} \quad (4.60)$$

$$= \frac{\omega^{2n}}{c^{2n}} \left(1 - \beta^{-2} \right)^n \quad (4.61)$$

$$= \left(\frac{2\pi i}{\beta \gamma \lambda} \right)^{2n}. \quad (4.62)$$

The remaining sum over n in Eq. (4.59) is the power series expansion of the zeroth-order Bessel function of the first kind; hence,

$$\begin{aligned}
 W(r, t) &= -e \cos(\omega\Delta t + \phi_0) \int_{-\infty}^{\infty} E_{z,0}^{\text{rf}}(z) \cos\left(\frac{2\pi z}{\beta \lambda}\right) dz \\
 &\quad \times \sum_{n=0}^{\infty} \left(\frac{-1}{4}\right)^n \frac{r^{2n}}{(n!)^2} \left(\frac{2\pi i}{\beta\gamma\lambda}\right)^{2n} \quad (4.63)
 \end{aligned}$$

$$\begin{aligned}
 &= -J_0\left(\frac{2\pi i}{\beta\gamma\lambda}\right) \cos(\omega\Delta t + \phi_0) \\
 &\quad \times e \int_{-\infty}^{\infty} E_{z,0}^{\text{rf}}(z) \cos\left(\frac{2\pi z}{\beta \lambda}\right) dz, \quad (4.64)
 \end{aligned}$$

completing the calculation.

CHAPTER 5

CONCLUSION: MORE TO LEARN FROM UED

Ultrafast science directly measures the time elapsed in physical, chemical and biological processes at a precision finer than 10^{-9} s. Photon-pump, photon-probe experiments are now approaching 10^{-18} s resolution. Methods that resolve these timescales are essential for studying complex systems, in which the interplay of many competing mechanisms makes the approach of fitting a dynamical model to time-independent data less reliable. Ultrafast pump-probe techniques are conveniently categorized by the particle species of the probe. Optical, x-ray and electron probes each have unique capabilities.

Electron probes are especially suited to investigate the structure of atomically-thin synthetic materials, such as graphene, on which future technological advances are likely to rely. There are many ways to extract information about samples from ultrafast electron probes: common examples are diffraction, transmission imaging and electron energy loss spectroscopy. Ultrafast electron diffraction is uniquely suited to detecting subtle, correlated structural changes, including transitions between structural phases. Moreover, at the present stage of technical development, UED offers the most scope to minimise the brightness-degrading effects of Coulomb repulsion. For this reason, dedicated ultrafast electron diffraction machines achieve the most intense beams and finest time resolution of all ultrafast electron probe modalities. Intense beams give UED the ability to resolve molecular and crystal structure in single-shot experiments, and to resolve subtle structural changes in stroboscopic experiments.

This thesis describes a novel ultrafast electron diffraction apparatus that employs a high-brightness electron source. It presents the design, commissioning,

first science results and potential future upgrades of the diffraction apparatus. The design of the diffraction apparatus incorporates a semiconductor photocathode with a band gap matched to the wavelength of the photoemission laser. The beam at the source therefore has low energy spread and exits the electron gun highly collimated. The brightness-diluting effects of Coulomb repulsion are mitigated in the design by emitting a 10 ps pulse, accelerating to 140 keV and then compressing to 100 fs. Beam diagnostic measurements show that the 5D beam-brightness thus attained is comparable to MeV UED facilities, remarkable given the sub-relativistic final beam energy, and only explicable thanks to the high source brightness. A 10^{-2} eV energy spread at the source is inferred by comparing beam-diagnostic measurements to beamline simulations, making the 6D brightness of the probe state of the art.

When coupled with a direct electron detector, the use of lock-in style data acquisition at 1 kHz frame rate allows the diffraction apparatus to reach high signal-to-noise, limited only by the average probe particle flux. Flexible beam transport allows the experimenter to exploit high brightness to form a micron sized diffraction probe. Making use of the small probe, first science results from the diffraction apparatus resolve in both space and time the diffusion of heat in a twisted heterobilayer composed of $\text{WSe}_2/\text{MoSe}_2$. Twisted 2D materials are scientifically and technologically interesting because their properties are highly tunable via the choice of twist angle. A novel pulse-picking technique, made possible by the high detector framerate, resolves two timescales in diffusion, pointing to the role played by interlayer excitonic quasiparticles in energy transport. Future experiments will explore the dependence of diffusivity on the bilayer twist angle.

The scientific reach of a diffraction machine is expanded by the addition of an electron spectrometer. Sensitivity to the full spectrum of electronic transitions and phonon excitations in a material requires a beam energy spread less than 10^{-2} eV. Conventional monochromators reduce energy spread by selecting out a fraction of the probe beam, but this technique becomes infeasible when pulsed operation leaves little room for further reduction in beam current. This thesis presents a feasibility study of a device that would achieve lossless monochromation, and shows that single meV energy spread at the sample is achievable even in the presence of realistic system jitter. Theory and simulation also show that this monochromation scheme removes the brightness-diluting effects of chromatic aberration via a 6D correlation between electron energy, time of flight and place of arrival at the radiofrequency lenses. The study thus illustrates what is possible when the full 6D phase space is made amenable to experimental control in a pulsed beam.

Future experiments could explore lensless imaging with the diffraction apparatus. Lensless imaging attempts to reconstruct a real space image numerically from diffraction data. *Holography* is one lensless imaging method [224], with a broad range of other applications, e.g., providing magnetic contrast in a microscope column with conventional image-forming lenses [225, 226].

Ptychography is a second method of lensless imaging that has undergone much recent development. Real-space resolution in ptychography is limited by the angular acceptance of the detector, the probe size and the uncertainty in the probe position on the sample [227]. To provide a brief sketch of the physical principles underlying the technique: it is well known that, in the weak-scattering limit, the diffraction pattern produced by plane wave-illumination is

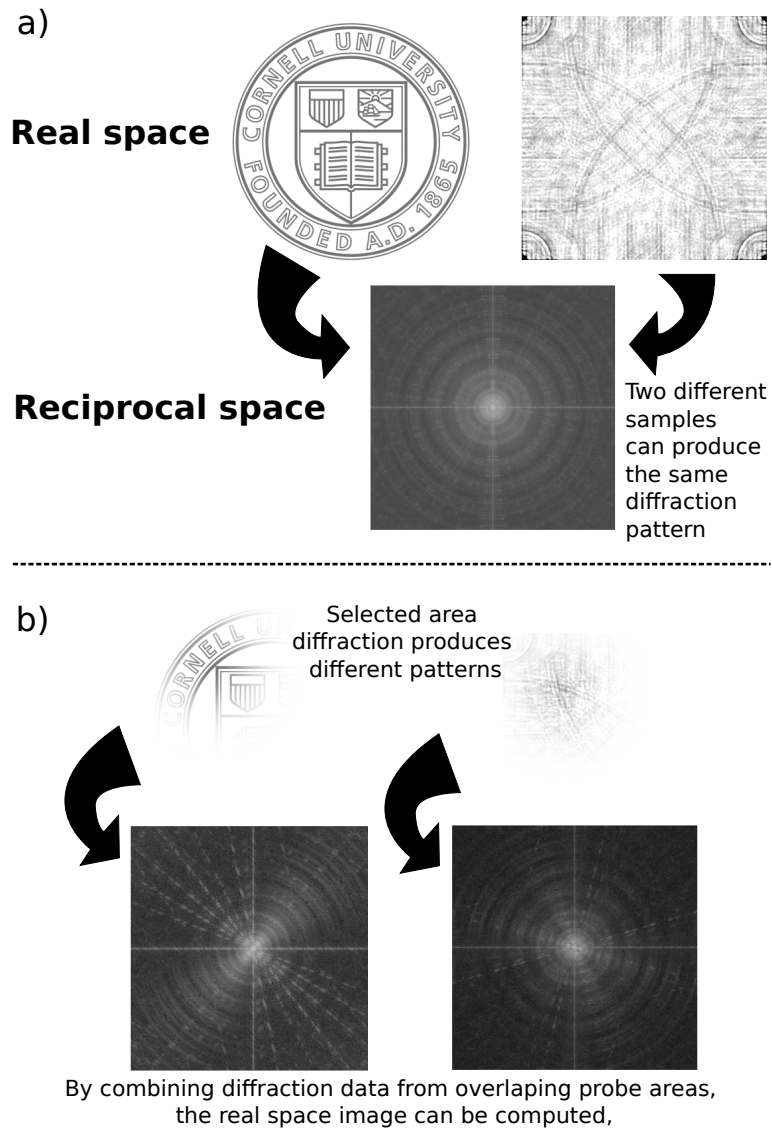


Figure 5.1: Computing a real-space image with diffraction data. (a) The diffraction pattern of an atomic lattice is not unique. (b) By performing selected area diffraction of overlapping subregions of a sample, it is possible to solve for the real-space atomic configuration. This *ptychography* technique might allow more flexibility in mitigating Coloumb forces and thus achieve higher resolution ultrafast electron imaging.

proportional to the squared-amplitude of the Fourier transform of the scattering potential. The phase information necessary to invert the Fourier transform is thus absent. To account for non-plane wave illumination, the Fourier transform of the potential is convolved with the Fourier transform of the illuminating wavefunction. Phase-interference terms contribute to the convolution and modulate the diffraction pattern, as illustrated in Fig. 5.1. Interference terms due to finite probe size thus open the door to the iterative estimation of the missing phase information.

In state of the art static electron beam ptychography today, subnanometer probes reach 10^{-11} m resolution [93, 228]: these probe sizes are presently well out of reach using ultrafast instruments. More realistically, earlier experiments with a $5\ \mu\text{m}$ diameter hard x-ray probe were able to resolve in ptychography features less than 10^{-7} m in size [229], comparable to the resolution achieved in UTEM [77]. As Chapter 2 of this thesis shows, our beamline can deliver a micron sized probe with 10^3 particles per pulse. It thus might be possible with the apparatus described in this thesis to perform nanometer scale ultrafast imaging via ptychography, but with much more than one electron per pulse, thereby increasing instrument sensitivity compared to existing UTEMs.

The ultimate limit on experimental precision is set by the quantum uncertainty principle. Instrumentalists cannot do better than provide a probe with a time-of-arrival, energy spread, divergence and size that is quantum limited. Ultrafast optical probes reached the transform limit some 50 years ago, but ultrafast electron probes remain orders of magnitude away. The diffraction apparatus described in this thesis, by employing an optimized source, as well as sophisticated beam control techniques, represents a significant step towards

quantum limited 6D brightness. The results reported here point to the potential for high impact science results from a quantum limited ultrafast electron probe. This thesis also lays theoretical and design groundwork for upgrading the machine to perform high-resolution, ultrafast electron energy loss spectroscopy in the future.

BIBLIOGRAPHY

1. Li, W. *et al.* A kiloelectron-volt ultrafast electron micro-diffraction apparatus using low emittance semiconductor photocathodes. *Structural Dynamics* **9**, 024302 (2022).
2. Aghanim, N. *et al.* Planck 2018 results-VI. Cosmological parameters. *Astronomy & Astrophysics* **641**, A6 (2020).
3. Particle-Data-Group. Review of Particle Physics. *Progress of Theoretical and Experimental Physics* **2020** (2020).
4. Yang, J. *et al.* Diffractive imaging of coherent nuclear motion in isolated molecules. *Physical Review Letters* **117**, 153002 (2016).
5. Einstein, A. Zur elektrodynamik bewegter körper. *Annalen der Physik* **4** (1905).
6. Cavalleri, A. *et al.* Femtosecond structural dynamics in VO 2 during an ultrafast solid-solid phase transition. *Physical Review Letters* **87**, 237401 (2001).
7. Siwick, B. J., Dwyer, J. R., Jordan, R. E. & Miller, R. D. An atomic-level view of melting using femtosecond electron diffraction. *Science* **302**, 1382–1385 (2003).
8. Gedik, N., Yang, D.-S., Logvenov, G., Bozovic, I. & Zewail, A. H. Nonequilibrium phase transitions in cuprates observed by ultrafast electron crystallography. *Science* **316**, 425–429 (2007).
9. Stojchevska, L. *et al.* Ultrafast switching to a stable hidden quantum state in an electronic crystal. *Science* **344**, 177–180 (2014).
10. Sie, E. J. *et al.* An ultrafast symmetry switch in a Weyl semimetal. *Nature* **565**, 61–66 (2019).

11. Bowman, R., Dantus, M. & Zewail, A. Femtosecond transition-state spectroscopy of iodine: From strongly bound to repulsive surface dynamics. *Chemical Physics Letters* **161**, 297–302 (1989).
12. Mokhtari, A., Cong, P., Herek, J. & Zewail, A. Direct femtosecond mapping of trajectories in a chemical reaction. *Nature* **348**, 225–227 (1990).
13. Ihee, H. *et al.* Direct imaging of transient molecular structures with ultrafast diffraction. *Science* **291**, 458–462 (2001).
14. Bressler, C. *et al.* Femtosecond XANES study of the light-induced spin crossover dynamics in an iron (II) complex. *Science* **323**, 489–492 (2009).
15. Austin, R. H., Beeson, K., Eisenstein, L., Frauenfelder, H. & Gunsalus, I. Dynamics of ligand binding to myoglobin. *Biochemistry* **14**, 5355–5373 (1975).
16. Millar, D., Robbins, R. & Zewail, A. Direct observation of the torsional dynamics of DNA and RNA by picosecond spectroscopy. *Proceedings of the National Academy of Sciences* **77**, 5593–5597 (1980).
17. Ansari, A. *et al.* Protein states and proteinquakes. *Proceedings of the National Academy of Sciences* **82**, 5000–5004 (1985).
18. Abadeer, N. S. & Murphy, C. J. Recent progress in cancer thermal therapy using gold nanoparticles. *The Journal of Physical Chemistry C* **120**, 4691–4716 (2016).
19. Nguyen, H. A., Srivastava, I., Pan, D. & Gruebele, M. Ultrafast nanometric imaging of energy flow within and between single carbon dots. *Proceedings of the National Academy of Sciences* **118** (2021).
20. Bacellar, C. *et al.* Femtosecond X-ray spectroscopy of haem proteins. *Faraday Discussions* **228**, 312–328 (2021).

21. Zewail, A. H. Femtochemistry: atomic-scale dynamics of the chemical bond using ultrafast lasers (Nobel Lecture). *Angewandte Chemie International Edition* **39**, 2586–2631 (2000).
22. Siegman, A. E. *How to (maybe) measure laser beam quality in Diode Pumped Solid State Lasers: Applications and Issues* (1998), MQ1.
23. Chao, A. W., Mess, K. H., et al. *Handbook of accelerator physics and engineering* (World scientific, 2013).
24. Musumeci, P. et al. Advances in bright electron sources. *Nuclear Instruments and Methods* **907**, 209–220 (2018).
25. Maiman, T. H. Stimulated optical radiation in ruby. *Nature* **4736**, 493–494 (1960).
26. McClung, F. & Hellwarth, R. Giant optical pulsations from ruby. *Applied Optics* **1**, 103–105 (1962).
27. Novak, J. & Windsor, M. Laser photolysis and spectroscopy in the nanosecond time range: Excited singlet state absorption in coronene. *The Journal of Chemical Physics* **47**, 3075–3076 (1967).
28. Lamb Jr, W. E. Theory of an optical maser. *Physical Review* **134**, A1429 (1964).
29. Ippen, S., Shank, C. & Dienes, A. Passive mode locking of the cw dye laser. *Applied Physics Letters* **21**, 348–350 (1972).
30. Shank, C. & Ippen, E. Subpicosecond kilowatt pulses from a mode-locked cw dye laser. *Applied Physics Letters* **24**, 373–375 (1974).
31. Millar, D., Shah, R. & Zewail, A. Picosecond saturation spectroscopy of cresyl violet: rotational diffusion by a “sticking” boundary condition in the liquid phase. *Chemical Physics Letters* **66**, 435–440 (1979).

32. Knox, W., Downer, M., Fork, R. & Shank, C. V. Amplified femtosecond optical pulses and continuum generation at 5-kHz repetition rate. *Optics Letters* **9**, 552–554 (1984).
33. Knox, W. *et al.* Optical pulse compression to 8 fs at a 5-kHz repetition rate. *Applied Physics Letters* **46**, 1120–1121 (1985).
34. Moulton, P. Recent advances in transition-metal-doped lasers. *Tunable Solid State Lasers*, 4–10 (1985).
35. Alain Zaouter, Y. *et al.* *Amplification d'impulsions ultra-courtes en régime non-linéaire dans les fibres dopées aux ions Ytterbium* PhD thesis (Bordeaux 1, 2008).
36. Gaumnitz, T. *et al.* Streaking of 43-attosecond soft-X-ray pulses generated by a passively CEP-stable mid-infrared driver. *Optics Express* **25**, 27506–27518 (2017).
37. Fausti, D. *et al.* Light-induced superconductivity in a stripe-ordered cuprate. *Science* **331**, 189–191 (2011).
38. Strickland, D. & Mourou, G. Compression of amplified chirped optical pulses. *Optics Communications* **55**, 447–449 (1985).
39. Rosker, M. J., Dantus, M. & Zewail, A. H. Femtosecond real-time probing of reactions. I. The technique. *The Journal of Chemical Physics* **89**, 6113–6127 (1988).
40. Murnane, M. M., Kapteyn, H. C., Rosen, M. D. & Falcone, R. W. Ultrafast x-ray pulses from laser-produced plasmas. *Science* **251**, 531–536 (1991).
41. Schoenlein, R. W. *et al.* Femtosecond X-ray pulses at 0.4 Å generated by 90 Thomson scattering: a tool for probing the structural dynamics of materials. *Science* **274**, 236–238 (1996).

42. Rischel, C. *et al.* Femtosecond time-resolved X-ray diffraction from laser-heated organic films. *Nature* **390**, 490–492 (1997).
43. Rose-Petruck, C. *et al.* Picosecond–millisecond lattice dynamics measured by ultrafast X-ray diffraction. *Nature* **398**, 310–312 (1999).
44. Emma, P. *et al.* First lasing and operation of an angstrom-wavelength free-electron laser. *Nature Photonics* **4**, 641–647 (2010).
45. Larson, B., Tischler, J. & Mills, D. Nanosecond resolution time-resolved x-ray study of silicon during pulsed-laser irradiation. *Journal of Materials Research* **1**, 144–154 (1986).
46. Lindenberg, A. *et al.* Time-resolved x-ray diffraction from coherent phonons during a laser-induced phase transition. *Physical Review Letters* **84**, 111 (2000).
47. Schoenlein, R. *et al.* Generation of femtosecond pulses of synchrotron radiation. *Science* **287**, 2237–2240 (2000).
48. Beaud, P. *et al.* Spatiotemporal stability of a femtosecond hard-X-ray undulator source studied by control of coherent optical phonons. *Physical Review Letters* **99**, 174801 (2007).
49. Wernet, P. *et al.* Orbital-specific mapping of the ligand exchange dynamics of Fe (CO) 5 in solution. *Nature* **520**, 78–81 (2015).
50. Kunnus, K. *et al.* Identification of the dominant photochemical pathways and mechanistic insights to the ultrafast ligand exchange of Fe (CO) 5 to Fe (CO) 4EtOH. *Structural Dynamics* **3**, 043204 (2016).
51. Dean, M. P. *et al.* Ultrafast energy- and momentum-resolved dynamics of magnetic correlations in the photo-doped Mott insulator Sr₂IrO₄. *Nature Materials* **15**, 601–605 (2016).

52. Huang, Z. & Kim, K.-J. Review of x-ray free-electron laser theory. *Physical Review Special Topics-Accelerators and Beams* **10**, 034801 (2007).
53. Deacon, D. A. *et al.* First operation of a free-electron laser. *Physical Review Letters* **38**, 892 (1977).
54. Milton, S. *et al.* Exponential gain and saturation of a self-amplified spontaneous emission free-electron laser. *Science* **292**, 2037–2041 (2001).
55. Allaria, E. *et al.* Highly coherent and stable pulses from the FERMI seeded free-electron laser in the extreme ultraviolet. *Nature Photonics* **6**, 699–704 (2012).
56. Ackermann, W. a. *et al.* Operation of a free-electron laser from the extreme ultraviolet to the water window. *Nature Photonics* **1**, 336–342 (2007).
57. Prat, E. *et al.* A compact and cost-effective hard X-ray free-electron laser driven by a high-brightness and low-energy electron beam. *Nature Photonics* **14**, 748–754 (2020).
58. Glowia, J. M. *et al.* Time-resolved pump-probe experiments at the LCLS. *Optics Express* **18**, 17620–17630 (2010).
59. Li, S. *et al.* Attosecond coherent electron motion in Auger-Meitner decay. *Science*, 285–290 (2022).
60. Ratner, D., Cryan, J., Lane, T., Li, S. & Stupakov, G. Pump-probe ghost imaging with SASE FELs. *Physical Review X* **9**, 011045 (2019).
61. Levantino, M. *et al.* Observing heme doming in myoglobin with femtosecond X-ray absorption spectroscopy. *Structural Dynamics* **2**, 041713 (2015).
62. Bird, P., Bradley, D. & Sibbett, W. in *High Speed Photography* 112–117 (Springer, 1975).

63. Mourou, G. & Williamson, S. Picosecond electron diffraction. *Applied Physics Letters* **41**, 44–45 (1982).
64. Williamson, J., Dantus, M., Kim, S. & Zewail, A. Ultrafast diffraction and molecular structure. *Chemical Physics Letters* **196**, 529–534 (1992).
65. Waldecker, L., Bertoni, R. & Ernstorfer, R. Compact femtosecond electron diffractometer with 100 keV electron bunches approaching the single-electron pulse duration limit. *Journal of Applied Physics* **117**, 044903 (2015).
66. Zong, A. *et al.* Evidence for topological defects in a photoinduced phase transition. *Nature Physics* **15**, 27–31 (2019).
67. Weathersby, S. P. *et al.* Mega-electron-volt ultrafast electron diffraction at SLAC National Accelerator Laboratory. *Review of Scientific Instruments* **86**, 073702 (2015).
68. Shen, X. *et al.* Femtosecond mega-electron-volt electron microdiffraction. *Ultramicroscopy* **184**, 172–176 (2018).
69. Zhu, P. *et al.* Femtosecond time-resolved MeV electron diffraction. *New Journal of Physics* **17**, 063004 (2015).
70. Filippetto, D. & Qian, H. Design of a high-flux instrument for ultrafast electron diffraction and microscopy. *Journal of Physics B: Atomic, Molecular and Optical Physics* **49**, 104003 (2016).
71. Chatelain, R. P., Morrison, V. R., Godbout, C. & Siwick, B. J. Ultrafast electron diffraction with radio-frequency compressed electron pulses. *Applied Physics Letters* **101**, 081901 (2012).
72. Gao, M. *et al.* Full characterization of RF compressed femtosecond electron pulses using ponderomotive scattering. *Optics Express* **20**, 12048–12058 (2012).

73. Van Oudheusden, T. *et al.* Compression of subrelativistic space-charge-dominated electron bunches for single-shot femtosecond electron diffraction. *Physical Review Letters* **105**, 264801 (2010).
74. Gliserin, A., Apolonski, A., Krausz, F. & Baum, P. Compression of single-electron pulses with a microwave cavity. *New Journal of Physics* **14**, 073055 (2012).
75. Zandi, O., Wilkin, K. J., Xiong, Y. & Centurion, M. High current tabletop setup for femtosecond gas electron diffraction. *Structural Dynamics* **4**, 044022 (2017).
76. Löhl, F. *et al.* Electron bunch timing with femtosecond precision in a superconducting free-electron laser. *Physical Review Letters* **104**, 144801 (2010).
77. Schliep, K. B., Quarterman, P., Wang, J.-P. & Flannigan, D. J. Picosecond Fresnel transmission electron microscopy. *Applied Physics Letters* **110**, 222404 (2017).
78. Plemmons, D. A. & Flannigan, D. J. Ultrafast electron microscopy: Instrument response from the single-electron to high bunch-charge regimes. *Chemical Physics Letters* **683**, 186–192 (2017).
79. Bostanjoglo, O., Elschner, R., Mao, Z., Nink, T. & Weingärtner, M. Nanosecond electron microscopes. *Ultramicroscopy* **81**, 141–147 (2000).
80. LaGrange, T. *et al.* Single-shot dynamic transmission electron microscopy. *Applied Physics Letters* **89**, 044105 (2006).
81. Kim, J. S. *et al.* Imaging of transient structures using nanosecond in situ TEM. *Science* **321**, 1472–1475 (2008).

82. Li, R. & Musumeci, P. Single-shot MeV transmission electron microscopy with picosecond temporal resolution. *Physical Review Applied* **2**, 024003 (2014).
83. Lu, C. *et al.* Imaging nanoscale spatial modulation of a relativistic electron beam with a MeV ultrafast electron microscope. *Applied Physics Letters* **112**, 113102 (2018).
84. Jin, N., Phillipp, F. & Seeger, A. Investigation of defect ordering in heavily irradiated metals by high-voltage electron microscopy. *Physica Status Solidi (A)* **116**, 91–111 (1989).
85. Zewail, A. H. Four-dimensional electron microscopy. *Science* **328**, 187–193 (2010).
86. Zhang, Y. & Flannigan, D. J. Observation of anisotropic strain-wave dynamics and few-layer dephasing in MoS₂ with ultrafast electron microscopy. *Nano Letters* **19**, 8216–8224 (2019).
87. Danz, T., Domröse, T. & Ropers, C. Ultrafast nanoimaging of the order parameter in a structural phase transition. *Science* **371**, 371–374 (2021).
88. Berruto, G. *et al.* Laser-induced skyrmion writing and erasing in an ultrafast cryo-Lorentz transmission electron microscope. *Physical Review Letters* **120**, 117201 (2018).
89. Barwick, B., Flannigan, D. J. & Zewail, A. H. Photon-induced near-field electron microscopy. *Nature* **462**, 902–906 (2009).
90. Piazza, L. *et al.* Simultaneous observation of the quantization and the interference pattern of a plasmonic near-field. *Nature Communications* **6**, 1–7 (2015).

91. Wang, K. *et al.* Coherent interaction between free electrons and a photonic cavity. *Nature* **582**, 50–54 (2020).
92. Urban, K. W. Studying atomic structures by aberration-corrected transmission electron microscopy. *Science* **321**, 506–510 (2008).
93. Chen, Z. *et al.* Electron ptychography achieves atomic-resolution limits set by lattice vibrations. *Science* **372**, 826–831 (2021).
94. Morimoto, Y. & Baum, P. Diffraction and microscopy with attosecond electron pulse trains. *Nature Physics* **14**, 252–256 (2018).
95. Porat, G. *et al.* Attosecond time-resolved photoelectron holography. *Nature communications* **9**, 1–6 (2018).
96. Maxson, J. *et al.* Direct measurement of sub-10 fs relativistic electron beams with ultralow emittance. *Physical Review Letters* **118**, 154802 (2017).
97. Li, J. & Sun, J. Application of X-ray diffraction and electron crystallography for solving complex structure problems. *Accounts of Chemical Research* **50**, 2737–2745 (2017).
98. Mo, M. *et al.* Heterogeneous to homogeneous melting transition visualized with ultrafast electron diffraction. *Science* **360**, 1451–1455 (2018).
99. Cremons, D. R., Plemmons, D. A. & Flannigan, D. J. Femtosecond electron imaging of defect-modulated phonon dynamics. *Nature Communications* **7**, 1–8 (2016).
100. Pomarico, E. *et al.* Ultrafast electron energy-loss spectroscopy in transmission electron microscopy. *MRS Bulletin* **43**, 497–503 (2018).
101. Vogelgesang, S. *et al.* Phase ordering of charge density waves traced by ultrafast low-energy electron diffraction. *Nature Physics* **14**, 184–190 (2018).

102. Wang, X., Wu, Z. & Ihee, H. H. *Femto-seconds electron beam diffraction using photocathode RF gun in Proceedings of the 2003 Particle Accelerator Conference* **1** (2003), 420–422.
103. Yang, J. *et al.* 100-femtosecond MeV electron source for ultrafast electron diffraction. *Radiation Physics and Chemistry* **78**, 1106–1111 (2009).
104. Ji, F. *et al.* Ultrafast relativistic electron nanoprobe. *Communications Physics* **2**, 1–10 (2019).
105. Fu, F. *et al.* High quality single shot ultrafast MeV electron diffraction from a photocathode radio-frequency gun. *Review of Scientific Instruments* **85**, 083701 (2014).
106. Williamson, J. C., Cao, J., Ihee, H., Frey, H. & Zewail, A. H. Clocking transient chemical changes by ultrafast electron diffraction. *Nature* **386**, 159–162 (1997).
107. Ischenko, A. A. *et al.* A stroboscopical gas-electron diffraction method for the investigation of short-lived molecular species. *Applied Physics B Photophysics and Laser Chemistry* **32**, 161–163 (1983).
108. Dudek, R. C. & Weber, P. M. Ultrafast Diffraction Imaging of the Electrocyclic Ring-Opening Reaction of 1, 3-Cyclohexadiene. *The Journal of Physical Chemistry A* **105**, 4167–4171 (2001).
109. Badali, D. S., Gengler, R. Y. & Miller, R. Ultrafast electron diffraction optimized for studying structural dynamics in thin films and monolayers. *Structural Dynamics* **3**, 034302 (2016).
110. Vanacore, G. M. *et al.* Attosecond coherent control of free-electron wave functions using semi-infinite light fields. *Nature Communications* **9**, 1–11 (2018).

111. Vanacore, G. M. *et al.* Ultrafast generation and control of an electron vortex beam via chiral plasmonic near fields. *Nature Materials* **18**, 573–579 (2019).
112. Zong, A. *et al.* Ultrafast manipulation of mirror domain walls in a charge density wave. *Science Advances* **4**, 5501 (2018).
113. Pomarico, E. *et al.* meV resolution in laser-assisted energy-filtered transmission electron microscopy. *ACS Photonics* **5**, 759–764 (2017).
114. Zhao, L. *et al.* Terahertz streaking of few-femtosecond relativistic electron beams. *Physical Review X* **8**, 021061 (2018).
115. Snively, E. *et al.* Femtosecond compression dynamics and timing jitter suppression in a THz-driven electron bunch compressor. *Physical Review Letters* **124**, 054801 (2020).
116. Qi, F. *et al.* Breaking 50 femtosecond resolution barrier in MeV ultrafast electron diffraction with a double bend achromat compressor. *Physical Review Letters* **124**, 134803 (2020).
117. Ruan, C.-Y. *et al.* The Development and Applications of Ultrafast Electron Nanocrystallography. *Microscopy and Microanalysis* **15**, 323–337 (2009).
118. Bie, Y.-Q., Zong, A., Wang, X., Jarillo-Herrero, P. & Gedik, N. A versatile sample fabrication method for ultrafast electron diffraction. *Ultramicroscopy*, 113389 (2021).
119. Langford, R. & Rogers, M. In situ lift-out: steps to improve yield and a comparison with other FIB TEM sample preparation techniques. *Micron* **39**, 1325–1330 (2008).

120. Maxson, J. M., Bartnik, A. C. & Bazarov, I. V. Efficient and accurate laser shaping with liquid crystal spatial light modulators. *Applied Physics Letters* **105**, 171109 (2014).
121. Maxson, J., Lee, H., Bartnik, A. C., Kiefer, J. & Bazarov, I. Adaptive electron beam shaping using a photoemission gun and spatial light modulator. *Phys. Rev. ST Accel. Beams* **18** (2015).
122. Thompson, D. *et al.* Suppression of emittance growth using a shaped cold atom electron and ion source. *Physical Review Letters* **117**, 193202 (2016).
123. Franssen, J., de Raadt, T., van Nindhuijs, M. & Luiten, O. Compact ultracold electron source based on a grating magneto-optical trap. *Physical Review Accelerators and Beams* **22**, 023401 (2019).
124. Kasmi, L., Kreier, D., Bradler, M., Riedle, E. & Baum, P. Femtosecond single-electron pulses generated by two-photon photoemission close to the work function. *New Journal of Physics* **17**, 033008 (2015).
125. Karkare, S. *et al.* Ultracold electrons via near-threshold photoemission from single-crystal Cu (100). *Physical Review Letters* **125**, 054801 (2020).
126. Bazarov, I. V., Dunham, B. M. & Sinclair, C. K. Maximum Achievable Beam Brightness from Photoinjectors. *Physical Review Letters* **102** (2009).
127. Filippetto, D., Musumeci, P., Zolotarev, M. & Stupakov, G. Maximum current density and beam brightness achievable by laser-driven electron sources. *Phys. Rev. ST Accel. Beams* **17** (2014).
128. Qian, H., Murphy, J., Shen, Y., Tang, C. & Wang, X. Surface photoemission in a high-brightness electron beam radio frequency gun. *Applied Physics Letters* **97**, 253504 (2010).

129. Maxson, J., Musumeci, P., Cultrera, L., Karkare, S. & Padmore, H. Ultrafast laser pulse heating of metallic photocathodes and its contribution to intrinsic emittance. *Nuclear Instruments and Methods* **865**, 99–104 (2017).
130. Bae, J. K. *et al.* Brightness of femtosecond nonequilibrium photoemission in metallic photocathodes at wavelengths near the photoemission threshold. *Journal of Applied Physics* **124**, 244903 (Dec. 2018).
131. Houdellier, F., Caruso, G. M., Weber, S., Kociak, M. & Arbouet, A. Development of a high brightness ultrafast transmission electron microscope based on a laser-driven cold field emission source. *Ultramicroscopy* **186**, 128–138 (2018).
132. Pierce, C. M. *et al.* Low intrinsic emittance in modern photoinjector brightness. *Phys. Rev. Accel. Beams* **23** (2020).
133. Zerbe, B. S., Xiang, X., Ruan, C.-Y., Lund, S. & Duxbury, P. Dynamical bunching and density peaks in expanding Coulomb clouds. *Phys. Rev. Accel. Beams* **21** (2018).
134. Chase, T. *et al.* Ultrafast electron diffraction from non-equilibrium phonons in femtosecond laser heated Au films. *Applied Physics Letters* **108**, 041909 (2016).
135. Curtis, W. A. & Flannigan, D. J. Toward fs–meV resolution in electron microscopy: systematic simulation of the temporal spread of single-electron packets. *Physical Chemistry Chemical Physics* **23**, 23544–23553 (2021).
136. Bianco, E. *et al.* Stable Continuously Variable Temperature Cryo-STEM to Understand the Structurally Driven Phase Transition in the 2D Layered Magnet Nb₃Br₈. *Microscopy and Microanalysis* **26**, 1090–1092 (2020).

137. Cultrera, L., Lee, H. & Bazarov, I. Alkali antimonides photocathodes growth using pure metals evaporation from effusion cells. *Journal of Vacuum Science & Technology B* **34**, 011202 (2016).
138. Maxson, J., Cultrera, L., Gulliford, C. & Bazarov, I. Measurement of the tradeoff between intrinsic emittance and quantum efficiency from a NaKSb photocathode near threshold. *Applied Physics Letters* **106**, 234102 (2015).
139. Wells, R. P. *et al.* Mechanical design and fabrication of the VHF-gun, the Berkeley normal-conducting continuous-wave high-brightness electron source. *Review of Scientific Instruments* **87**, 023302 (2016).
140. Karkare, S. *et al.* Temperature-dependent quantum efficiency degradation of K-Cs-Sb bialkali antimonide photocathodes grown by a triple-element codeposition method. *Phys. Rev. Accel. Beams* **20**, 113401 (2017).
141. Lee, H. *et al.* A cryogenically cooled high voltage DC photoemission electron source. *Review of Scientific Instruments* **89**, 083303 (2018).
142. Bazarov, I. V. *et al.* Efficient temporal shaping of electron distributions for high-brightness photoemission electron guns. *Phys. Rev. ST Accel. Beams* **11**, 040702 (4 2008).
143. Li, R. K., Roberts, K. G., Scoby, C. M., To, H. & Musumeci, P. Nanometer emittance ultralow charge beams from rf photoinjectors. *Phys. Rev. ST Accel. Beams* **15**, 090702 (9 2012).
144. Van Oudheusden, T. *et al.* Electron source concept for single-shot sub-100 fs electron diffraction in the 100 keV range. *Journal of Applied Physics* **102**, 093501 (2007).

145. Otto, M. R., René de Cotret, L., Stern, M. J. & Siwick, B. J. Solving the jitter problem in microwave compressed ultrafast electron diffraction instruments: Robust sub-50 fs cavity-laser phase stabilization. *Structural Dynamics* **4**, 051101 (2017).
146. General Particle Tracer, <http://www.pulsar.nl/gpt/>.
147. Gulliford, C., Bartnik, A. & Bazarov, I. Multiobjective optimizations of a novel cryocooled dc gun based ultrafast electron diffraction beam line. *Phys. Rev. Accel. Beams* **19**, 093402 (2016).
148. Piazza, L. *et al.* Design and implementation of a fs-resolved transmission electron microscope based on thermionic gun technology. *Chemical Physics* **423**, 79–84 (2013).
149. Bach, N. *et al.* Coulomb interactions in high-coherence femtosecond electron pulses from tip emitters. *Structural Dynamics* **6**, 014301 (2019).
150. Feist, A. *et al.* Ultrafast transmission electron microscopy using a laser-driven field emitter: Femtosecond resolution with a high coherence electron beam. *Ultramicroscopy* **176**, 63–73 (2017).
151. Li, R. *et al.* Note: Single-Shot Continuously Time-Resolved MeV Ultrafast Electron Diffraction. *Review of Scientific Instruments* **81**, 036110. ISSN: 0034-6748 (Mar. 2010).
152. Musumeci, P. *et al.* Capturing Ultrafast Structural Evolutions with a Single Pulse of MeV Electrons: Radio Frequency Streak Camera Based Electron Diffraction. *Journal of Applied Physics* **108**, 114513 (2010).
153. Scoby, C. M., Li, R. K. & Musumeci, P. Effect of an ultrafast laser induced plasma on a relativistic electron beam to determine temporal overlap in pump–probe experiments. *Ultramicroscopy* **127**, 14–18 (2013).

154. Stern, M. J. *et al.* Mapping momentum-dependent electron-phonon coupling and nonequilibrium phonon dynamics with ultrafast electron diffuse scattering. *Physical Review B* **97**, 165416 (2018).
155. Allen, L. J., Findlay, S., *et al.* Modelling the inelastic scattering of fast electrons. *Ultramicroscopy* **151**, 11–22 (2015).
156. Tate, M. W. *et al.* High dynamic range pixel array detector for scanning transmission electron microscopy. *Microscopy and Microanalysis* **22**, 237–249 (2016).
157. Cao, Y. *et al.* Unconventional superconductivity in magic-angle graphene superlattices. *Nature* **556**, 43–50 (2018).
158. Yoo, H. *et al.* Atomic and electronic reconstruction at the van der Waals interface in twisted bilayer graphene. *Nature Materials* **18**, 448–453 (2019).
159. Liao, M. *et al.* Precise control of the interlayer twist angle in large scale MoS₂ homostructures. *Nature Communications* **11**, 1–8 (2020).
160. Liu, F. *et al.* Disassembling 2D van der Waals crystals into macroscopic monolayers and reassembling into artificial lattices. *Science* **367**, 903–906 (2020).
161. Kim, S. E. *et al.* Extremely anisotropic van der Waals thermal conductors. *Nature* **597**, 660–665 (2021).
162. Zhao, B. *et al.* High-order superlattices by rolling up van der Waals heterostructures. *Nature* **591**, 385–390 (2021).
163. Gadelha, A. C. *et al.* Localization of lattice dynamics in low-angle twisted bilayer graphene. *Nature* **590**, 405–409 (2021).

164. Allahgholi, A. *et al.* Megapixels@Megahertz—the AGIPD high-speed cameras for the European XFEL. *Nuclear Instruments and Methods* **942**, 162324 (2019).
165. Leonarski, F. *et al.* Fast and accurate data collection for macromolecular crystallography using the JUNGFRÄU detector. *Nature Methods* **15**, 799–804 (2018).
166. Ramilli, M. *et al.* Measurements with MÖNCH, a 25 μm pixel pitch hybrid pixel detector. *Journal of Instrumentation* **12**, C01071 (2017).
167. Bai, Y. *et al.* Excitons in strain-induced one-dimensional Moire potentials at transition metal dichalcogenide heterojunctions. *Nature Materials* **19**, 1068–1073 (2020).
168. Wang, J. *et al.* Diffusivity Reveals Three Distinct Phases of Interlayer Excitons in MoSe₂/WSe₂ Heterobilayers. *Physical Review Letters* **126**, 106804 (2021).
169. Chatelain, R. P., Morrison, V. R., Klarenaar, B. L. & Siwick, B. J. Coherent and incoherent electron-phonon coupling in graphite observed with radio-frequency compressed ultrafast electron diffraction. *Physical Review Letters* **113**, 235502 (2014).
170. Tran, K. *et al.* Evidence for Moire excitons in van der Waals heterostructures. *Nature* **567**, 71–75 (2019).
171. Seyler, K. L. *et al.* Signatures of Moire-trapped valley excitons in MoSe₂/WSe₂ heterobilayers. *Nature* **567**, 66–70 (2019).
172. Brem, S., Linderälv, C., Erhart, P. & Malic, E. Tunable phases of Moire excitons in van der Waals heterostructures. *Nano Letters* **20**, 8534–8540 (2020).

173. Philipp, H. T. *et al.* Very-High Dynamic Range, 10,000 Frames/Second Pixel Array Detector for Electron Microscopy. *Microscopy and Microanalysis* **28**, 425–440 (2022).
174. Schneider, G. F., Calado, V. E., Zandbergen, H., Vandersypen, L. M. & Dekker, C. Wedging transfer of nanostructures. *Nano Letters* **10**, 1912–1916 (2010).
175. Duncan, C. J., Muller, D. A. & Maxson, J. M. Lossless Monochromation for Electron Microscopy with Pulsed Photoemission Sources and Radio-Frequency Cavities. *Physical Review Applied* **14**, 014060 (2020).
176. Hawkes, P. Aberration correction past and present. *Philosophical Transactions of the Royal Society A: Mathematical, Physical and Engineering Sciences* **367**, 3637–3664 (2009).
177. Scherzer, O. The theoretical resolution limit of the electron microscope. *Journal of Applied Physics* **20**, 20–29 (1949).
178. Schönhense, G. & Spiecker, H. Correction of chromatic and spherical aberration in electron microscopy utilizing the time structure of pulsed excitation sources. *Journal of Vacuum Science & Technology B* **20**, 2526–2534 (2002).
179. Khursheed, A. Dynamic chromatic aberration correction in low energy electron microscopes. *Journal of Vacuum Science & Technology B* **23**, 2749–2753 (2005).
180. Reijnders, M. *et al.* Phase-space manipulation of ultracold ion bunches with time-dependent fields. *Physical Review Letters* **105**, 034802 (2010).
181. Oldfield, L. C. *Microwave cavities as electron lenses*. PhD thesis (University of Cambridge, 1974).

182. Chatelain, R. P., Morrison, V. R., Godbout, C. & Siwick, B. J. Ultrafast electron diffraction with radio-frequency compressed electron pulses. *Applied Physics Letters* **101**, 081901 (2012).
183. Gliserin, A., Walbran, M., Krausz, F. & Baum, P. Sub-phonon-period compression of electron pulses for atomic diffraction. *Nature Communications* **6**, 8723 (2015).
184. Van Oudheusden, T. *et al.* Compression of subrelativistic space-charge-dominated electron bunches for single-shot femtosecond electron diffraction. *Physical Review Letters* **105**, 264801 (2010).
185. Maxson, J. *et al.* Direct measurement of sub-10 fs relativistic electron beams with ultralow emittance. *Physical Review Letters* **118**, 154802 (2017).
186. Zeitler, B., Floettmann, K. & Grüner, F. Linearization of the longitudinal phase space without higher harmonic field. *Physical Review Special Topics-Accelerators and Beams* **18**, 120102 (2015).
187. Pasmans, P., van den Ham, G., Dal Conte, S., van der Geer, S. & Luiten, O. Microwave TM₀₁₀ cavities as versatile 4D electron optical elements. *Ultramicroscopy* **127**, 19–24 (2013).
188. Zhao, L. *et al.* Terahertz streaking of few-femtosecond relativistic electron beams. *Physical Review X* **8**, 021061 (2018).
189. Li, R. *et al.* Terahertz-based subfemtosecond metrology of relativistic electron beams. *Physical Review Accelerators and Beams* **22**, 012803 (2019).
190. Cesar, D. & Musumeci, P. Temporal magnification for streaked ultrafast electron diffraction and microscopy. *Ultramicroscopy* **199**, 1–6 (2019).
191. Kolner, B. H. & Nazarathy, M. Temporal imaging with a time lens. *Optics Letters* **15**, 655.

192. Hachmann, M. & Flöttmann, K. Measurement of ultra low transverse emittance at REGAE. *Nuclear Instruments and Methods* **A829**, 318–320 (2016).
193. Filippetto, D. & Qian, H. Design of a high-flux instrument for ultrafast electron diffraction and microscopy. *Journal of Physics B: Atomic, Molecular and Optical Physics* **49**, 104003 (2016).
194. Sannomiya, T., Arai, Y., Nagayama, K. & Nagatani, Y. Transmission Electron Microscope Using a Linear Accelerator. *Physical Review Letters* **123**, 150801 (2019).
195. Lassise, A., Mutsaers, P. & Luiten, O. Compact, low power radio frequency cavity for femtosecond electron microscopy. *Review of Scientific Instruments* **83**, 043705 (2012).
196. Oldfield, L. C. A rotationally symmetric electron beam chopper for picosecond pulses. *Journal of Physics E: Scientific Instruments* **9**, 455 (1976).
197. Verhoeven, W., van Rens, J. F. M., Kieft, E. R., Mutsaers, P. H. A. & Luiten, O. J. High quality ultrafast transmission electron microscopy using resonant microwave cavities. *Ultramicroscopy* **188**, 85–89 (2018).
198. Murooka, Y. *et al.* Transmission-electron diffraction by MeV electron pulses. *Applied Physics Letters* **98**, 251903 (2011).
199. Verhoeven, W. *et al.* Time-of-flight electron energy loss spectroscopy by longitudinal phase space manipulation with microwave cavities. *Structural Dynamics* **5**, 051101 (2018).
200. Ura, K. & Morimura, N. Generation of picosecond pulse electron beams. *Journal of Vacuum Science and Technology* **10**, 948–950 (1973).

201. Hosokawa, T., Fujioka, H. & Ura, K. Gigahertz stroboscopy with the scanning electron microscope. *Review of Scientific Instruments* **49**, 1293–1299 (1978).
202. Krivanek, O. L. *et al.* Vibrational spectroscopy in the electron microscope. *Nature* **514**, 209 (2014).
203. Venkatraman, K., Levin, B. D., March, K., Rez, P. & Crozier, P. A. Vibrational spectroscopy at atomic resolution with electron impact scattering. *Nature Physics* **15**, 1237–1241 (2019).
204. Joy, D. C. & Joy, C. S. Low voltage scanning electron microscopy. *Micron* **27**, 247–263 (1996).
205. Koppell, S. A. *et al.* Design for a 10 KeV Multi-Pass Transmission Electron Microscope. *arXiv preprint arXiv:1904.11064* (2019).
206. Krivanek, O. L. *et al.* High-energy-resolution monochromator for aberration-corrected scanning transmission electron microscopy/electron energy-loss spectroscopy. *Philosophical Transactions of the Royal Society* **367**, 3683–3697 (2009).
207. Mankos, M., Shadman, K. & Kolarik, V. Novel electron monochromator for high resolution imaging and spectroscopy. *Journal of Vacuum Science & Technology B* **34**, 06KP01 (2016).
208. Williams, J. *et al.* Active control of bright electron beams with RF optics for femtosecond microscopy. *Structural Dynamics* **4**, 044035 (2017).
209. Li, R. & Wang, X. Femtosecond MeV Electron Energy-Loss Spectroscopy. *Physical Review Applied* **8**, 054017 (2017).
210. Karkare, S. *et al.* Ultrabright and ultrafast III-V semiconductor photocathodes. *Physical Review Letters* **112**, 097601 (2014).

211. Rao, T. & Dowell, D. H. An Engineering Guide To Photoinjectors. *arXiv preprint arXiv:1403.7539* (2014).
212. Bartels, A., Dekorsy, T. & Kurz, H. Femtosecond Ti: sapphire ring laser with a 2-GHz repetition rate and its application in time-resolved spectroscopy. *Optics Letters* **24**, 996–998 (1999).
213. Krivanek, O. L., Lovejoy, T. C., Dellby, N. & Carpenter, R. Monochromated STEM with a 30 meV-wide, atom-sized electron probe. *Microscopy* **62**, 3–21 (2013).
214. Dowell, D. & Schmerge, J. Quantum efficiency and thermal emittance of metal photocathodes. *Physical Review Special Topics-Accelerators and Beams* **12**, 074201 (2009).
215. Feist, A. *et al.* Ultrafast transmission electron microscopy using a laser-driven field emitter: Femtosecond resolution with a high coherence electron beam. *Ultramicroscopy* **176**, 63–73 (2017).
216. Scheinfein, M., Qian, W. & Spence, J. Aberrations of emission cathodes: Nanometer diameter field-emission electron sources. *Journal of Applied Physics* **73**, 2057–2068 (1993).
217. Stern, M. J. *et al.* Mapping momentum-dependent electron-phonon coupling and nonequilibrium phonon dynamics with ultrafast electron diffuse scattering. *Physical Review B* **97**, 165416 (2018).
218. Cultrera, L. *et al.* Cold electron beams from cryocooled, alkali antimonide photocathodes. *Physical Review Special Topics-Accelerators and Beams* **18**, 113401 (2015).

219. Franssen, J. & Luiten, O. Improving temporal resolution of ultrafast electron diffraction by eliminating arrival time jitter induced by radiofrequency bunch compression cavities. *Structural Dynamics* **4**, 044026 (2017).
220. Van der Geer, B. & De Loos, M. *The general particle tracer code: design, implementation and application* (2001).
221. Baum, P. Quantum dynamics of attosecond electron pulse compression. *Journal of Applied Physics* **122**, 223105 (2017).
222. Cardin, V. *et al.* High power hollow-core fiber compression of Yb lasers as ideal drivers for HHG in CLEO: Science and Innovations (2018), SM4M-3.
223. Zuo, J. M. & Spence, J. C. *Advanced transmission electron microscopy* (Springer, 2017).
224. Stadler, L.-M. *et al.* Hard x ray holographic diffraction imaging. *Physical Review Letters* **100**, 245503 (2008).
225. Bonevich, J. *et al.* Electron holography observation of vortex lattices in a superconductor. *Physical review letters* **70**, 2952 (1993).
226. Houdellier, F. *et al.* Optimization of off-axis electron holography performed with femtosecond electron pulses. *Ultramicroscopy* **202**, 26–32 (2019).
227. Deng, J. *et al.* The velociprobe: An ultrafast hard x-ray nanoprobe for high-resolution ptychographic imaging. *Review of Scientific Instruments* **90**, 083701 (2019).
228. Jiang, Y. *et al.* Electron ptychography of 2D materials to deep sub-ngström resolution. *Nature* **559**, 343–349 (2018).
229. Rodenburg, J. M. *et al.* Hard-x-ray lensless imaging of extended objects. *Physical Review Letters* **98**, 034801 (2007).